PEOPLE'S DEMOCRATIC REPUBLIC OF ALGERIA
MINISTRY OF HIGHER EDUCATION AND SCIENTIFIC RESEARCH
UNIVERSITY OF MENTOURI BROTHERS – CONSTANTINE 1
EXACT SCIENCES FACULTY
PHYSICS DEPARTMENT

Order N°:

Series:

THE EFFECTS OF MWCNTs ON IRON–COPPER NANOCOMPOSITES THERMAL-STRUCTURAL PROPERTIES

A Dissertation
Submitted to The Department of Physics
University of Mentouri Brothers–Constantine 1
In Partial Fulfillment
of the Requirements for the Degree of
3rd cycle Doctorate in
Physics
Speciality: Nanomaterials & Advanced Materials
by
BOULEKLAB MOHAMED CHERIF
16/12/ 2021

Doctoral committee:

Chairman:	A. BOUBERTAKH	Prof.	Constantine 1 University
Advisor:	S. HAMAMDA	Prof.	Constantine 1 University
Examiners:	N. BELLAL	Prof.	Constantine 1 University
	K. LATROUS	Prof.	Constantine 3 University
	R. GUEMINI	Prof.	Larbi Ben M'hidi University
	K. CHETEHOUNA	Prof.	INSA Centre Val de Loire-France

This page intentionally left blank

Dedication

To whom I owe it all

To mother

May Allah have mercy

on her soul and reward

her with the good ending

Acknowledgements

First and foremost, I would like to express my gratitude to my thesis advisor, Professor S. Hamamda, whose expertise, understanding, and patience added considerably to my Ph.D. study at UMC 1. During my graduate years, he provided me with direction, technical support, and became more of a mentor and a friend than an advisor. I feel truly grateful and fortunate to be one of his students.

I would also like to thank the members of my defence and candidacy examining committees for their interest: Prof. A. Boubertakh, Prof. K. Latrous, Prof. N. Bellal, Prof. R. Guemini, Prof. K. Chetehouna.

I recognized that this research would not have been possible without the technical assistance from all members in our laboratory LTTSM, current and former: Prof. A. Karaali, Prof. A. Boudjada, Prof. N. Boukhiet, Dr. I. Zerrouk, Dr. M. Zehaf,

Dr. T. Dorbani, Dr. A Djari, A.M. Bazine, H. Filali.

Abstract

The subject studied in the presented thesis is the effect of incorporating different concentrations of multiwall carbon nanotubes into iron-copper — Fe–Cu with a ratio of 4:1; MWCNTs of 0.5, 1.0 and 2.0 vol.%—nanocomposites—made via mechanical milling of different times of 20, 60 and 120 minutes— on the thermal and structural properties.

The characterisations conducted were heat flow and thermogravimetry, the relative linear expansion ($\Delta L/L_0$), coefficient of linear thermal expansion (CTE) for the thermal behaviour, on the other hand for the structural changes, x-ray diffraction, Raman spectroscopy and infrared absorptions were applied. Several temperature ranges were distinguished for the Fe–Cu–MWCNTs nanocomposite by the $\Delta L/L_0$ (T) and CTE temperature dependences. Effect of CNTs on the $\Delta L/L_0$ and CTE temperature dependences are different for different temperature ranges, and the magnitude of the effect depends on the CNTs content.

The heat flow and thermogravimetry show thermal stability and higher calorific capacity for the samples with longer milling time and containing a higher concentration of CNTs.

As for the coefficient of thermal expansion, an improvement in CTE of the Fe–Cu-1% MWCNTs milled for 120 minutes.

The provided x-ray diffraction patterns show a grain refinement for the 120 minutes milling time, also a homogenous distribution of CNTs (the absence of CNTs clusters appearing as carbon graphite)

Raman spectroscopy reveals a higher defect density with a longer milling time, except for 60 minutes samples showing a lower defect density which indicates the healing and the recovery of CNTs.

Infrared spectroscopy aid in showing the presence of functional groups in the samples and the establishment of multiple bonding types.

ملخص

تَأْثِيرْ أَنَابِيبْ اَلْكَرْبُونْ اَلْنَانَوِيَةْ عَلَى اَلْخَصَائِصْ اَلْحَرَارِيَةْ-اَلْبُنْيَوِيَةْ لِلْمُرَكَبْ اَلْنَانُومِتْرِيْ حَدِيدْ-نُحَاس

الموضوع قيد الدراسة و المقدم في هاته لأطروحة هو تأثير إرفاق تراكيز مختلفة من أنابيب الكربون النانومترية متعددة الجدران داخل المزيج النانومتري لحبيبات الحديد–النحاس —بتواجد نسبي للحديد–نحاس 4 إلى 1 و المحضرعن طريق الطحن الميكانيكي على مر عدة أزمنة إبتداءا من 20 دقيقة, ف 60 دقيقة لتليها أخيرا 120 دقيقة, و نسبة حجمية إبتداءا من 0.5 , 1.0 و 2 بالمئة من أنابيب الكربون النانومترية متعددة الجدران— على الخصائص الحرارية و البنيوية.

الخصائص التي أجريت هي التدفق الحراري و القياس الحراري, التمدد الخطي النسبي $(\Delta L/L_0)$, معامل التمدد الحراري الخطي (CTE) , من ناحية التغييرات الهيكلية, حيود الأشعة السينية, مطيافية Raman

و تم أيضا تطبيق إمتصاص الأشعة تحت الحمراء. تم تمييز العديد من نطاقات درجة الحرارة للمركب النانوي حديد–نحاس-أنابيب الكربون النانومترية متعددة الجدران من خلال $(\Delta L/L_0)$ و (CTE) و إعتمادهما على درجة الحرارة. يختلف تأثير أنابيب الكربون النانوية على تبعيات درجة الحرارة $(\Delta L/L_0)$ و (CTE) بإختلاف نطاقات درجات الحرارة, و يعتمد حجم التأثير على كمية محتوى أنابيب الكربون النانوية.

يُظهر التدفق الحراري والقياس الحراري ثباتًا حراريًا وقدرة حرارية أعلى للعينات ذات وقت طحن أطول وتحتوي على تركيز أعلى من أنابيب الكربون النانوية.

بالنسبة لمعامل التمدد الحراري, هنالك تحسن ملحوظ بالنسبة لعينة حديد–نحاس-أنابيب كربون نانوية ذات تركيز حجمي واحد بالمئة المطحون لمدة ساعتين.

تُظهر أنماط حيود الأشعة السينية المقدمة تحسينًا للحبوب لمدة 120 دقيقة من وقت الطحن ، وكذلك توزيعًا متجانسًا لأنابيب الكربون النانوية الكربونية (غياب مجموعات الأنابيب النانوية الكربونية التي تظهر كغرافيت كربون)

من ناحية أخرى, قام تحليل Raman الطيفي بتقييم التماسك الظاهري للأنابيب الكربون النانوية و حالة التلف نتيجة زمن الطحن, و قد كشف عن كثافة أعلى للتشوهات كلما كان وقت الطحن أطول, مع إستثناء لعينات زمن الطحن الموافق ل 60 دقيقة أين أظهر كثافة عيوب أقل نسبيا مما يشير إلى شفاء و إسترجاع أنابيب الكربون النانوية.

يساعد التحليل الطيفي بالأشعة تحت الحمراء في إظهار وجود مجموعات وظيفية في العينات وإنشاء أنواع ترابط متعددة.

Résumé

Les effets des NTCM sur les propriétés thermo-structural des nanocomposites de Fe–Cu

Le thème étudié porte sur l'effet de l'incorporation de différentes concentrations de nanotubes de carbone multiparois dans du fer-cuivre — Fe–Cu avec un rapport de 4:1 ; NTCM de 0,5, 1,0 et 2,0 % en volume—nanocomposites—fabriqués par broyage mécanique de différentes durées de 20, 60 et 120 minutes—sur les propriétés thermiques et structurelles.

Les caractérisations conduites ont été le flux thermique et la thermogravimétrie, la dilatation linéaire relative ($\Delta L/L_0$), le coefficient de dilatation thermique linéaire (CDT) pour le comportement thermique, d'autre part pour les changements structurels, la diffraction des rayons X, la spectroscopie Raman et l'infrarouge. L’absorption a été appliquée. Plusieurs gammes de températures ont été distinguées pour le nanocomposite Fe–Cu–NTCM par les dépendances de température $\Delta L/L_0$ (T) et CDT. L'effet des NTC sur les dépendances de température $\Delta L/L_0$ et CDT est différent pour différentes plages de température, et l'ampleur de l'effet dépend de la teneur en NTC.

Le flux de chaleur et la thermogravimétrie montrent une stabilité thermique et une capacité calorifique plus élevée pour les échantillons avec un temps de broyage plus long et contenant une concentration plus élevée de NTC.

En ce qui concerne le coefficient de dilatation thermique, le CDT amélioré des Fe–Cu-1% NTCM broyés pendant 120 minutes.

Les diagrammes de diffraction des rayons X fournis montrent un raffinement du grain pour le temps de broyage de 120 minutes, ainsi qu'une répartition homogène des NTC (l'absence d'agrégats de NTC apparaissant sous forme de graphite de carbone)

La spectroscopie Raman, d'autre part, a évalué l'intégrité de la morphologie des NTC et l'état d'endommagement du temps de broyage, elle révèle une densité de défauts plus élevée avec un temps de broyage plus long, à l'exception des 60 minutes, elle montre une densité de défauts plus faible qui indique la guérison et la récupération des NTC.

La spectroscopie infrarouge aide à montrer la présence de groupes fonctionnels dans les échantillons et l'établissement de plusieurs types de liaison.

Contents

List of Tables

List of Figures

Figure Page

I

INTRODUCTION

“When we get to the very, very small world — say circuits of seven atoms — we have a lot of new things that would happen that represent completely new opportunities for design. Atoms on a small scale behave like nothing else on a large scale, for they satisfy the laws of quantum mechanics”.

Richard Feynman, *There’s plenty of room at the bottom*

Since the dawn of time, the human journey through life wasn't any easier, from the discovery of fire to building pyramids with unprecedented precisions that even held its end in recent times, to unveiling the mysteries lies in the cold perpetual darkness of deep oceans, to the era where human race witnesses the greatest conflicts known to men, from WWI to WWII, concluding it with a cold war between the two polls of power on earth, racing against one another to acquire advantageous technologies in both space and weaponry, even nowadays the race heating up with the join of other rising forces, which fuelled the innovations and researches even further, hence the need for new and advanced composite materials to fulfil the ever-increasing demand for more reliable and improved devices in a vast range of applications.

The urge for such advanced materials leads to the development of new technologies that dealt with miniaturizing materials toward atomic-scale which gives a rise to a new branch of technologies and science alike, hence the name, nanotechnologies — the design and production of structures, devices, and circuitry at the nanometre scale — and it represents the cutting edge of many scientific fields ranging from biology to computers. The emergence of nanotechnologies opens doors to the realm of nanoscale and its uncharted and strange properties and behaviour like nothing else.

The most known material that springs in popularity with its derivative nanostructure, it is the building block of all organic compounds, ***carbon*** which by itself has been known to mankind for millenniums in its allotropic forms, as a residue of burned organic materials (soot), to coal which was the pillar stone of the industrial revolution which was a key moment in history that shaped the world as we know it today, to graphite where it's been exploited to an extent from a very simple use as pencils to a more complex one in a nuclear reactor as a moderator which control (deaccelerate) the ejection of neutrons from the nuclear fuel rods during fission; to the hardest and most thermally conductive known *natural* material as well as the most extensively researched member of carbon family yet; diamond is found deep within the Earth's mantle formed under conditions of intense heat and pressure, diamond considered the most precious hence the use in jewellery, while the synthetic and most of the natural one used in grinding tools and excavators.

Other forms of carbon are either discovered or manmade, such as fullerene, multiwall carbon nanotubes, singlewall nanotubes, graphene, carbyne with the door open for new ones.

Among the most useful nanostructures created so far are carbon nanotubes (CNTs) which possess a broad range of unique physical, mechanical, and electronic properties, such properties have created an enormous amount of excitement in research laboratories across the world. This is evident from the exponential growth over the last decade in journal publications and conference presentations on all subjects related to CNTs.

Current applications of CNTs — ranging from lightweight space frames and computer chips to scaffolds for the regeneration of damaged nerves — only hint at their broader commercial and scientific potential once they can be manufactured in greater quantities and at significantly lower costs.

The discovery of carbon nanotubes has brought a promising future into the development of metal matrix nanocomposites materials which is of great importance in present-day materials technology.

The inclusion of carbon nanotubes (CNTs) into metallic systems has a chemical reaction with two aspects, (i) The partial chemical reaction at the CNT/metal interface and (ii) the complete chemical reaction of CNTs with a metallic matrix, the first is favourable for load baring application while the latter can bilaterally affect the physicomechanical properties of CNT-dispersed metal matrix nanocomposites. Hence sharing and transferring mechanical and thermal properties into the hosting metallic matrix nanocomposites, to obtain a high-strength and conductive improved nanocomposite

The need for materials with improved Physicochemical, electrical, thermal, and other properties is a springboard for qualitative scientific and technological advances not only in aerospace and shipbuilding but also in mechanical, power, electronic, electrical, radio engineering, automotive, construction, and other industries

Few studies have been dedicated to the Fe–Cu-X% MWCNTs nanocomposites mechanical and electromagnetic properties, while thermal investigations remain fewer

This thesis is concerned with the iron–copper metal matrix nanocomposites mixture prepared via high energy ball milling —for mechanochemical activation— of different milling times, with the incorporation of different volume concentrations of multiwall carbon nanotubes prepared via chemical vapour deposition, studied thoroughly in this thesis the thermal and structural behaviour and changes using multiple characterisation tools such as differential scanning calorimetry (DSC), thermogravimetry (TG), dilatometry, X-ray diffraction, both Raman and infrared spectroscopy. For temperature dependence measurements such as DSC, TG and dilatometry, temperature range from room temperature up to 800 °C.

The first chapter is an intro to the evolution of humans and the struggles that springboard the innovations for new and better performance materials. In chapter II we have a literature review in two parts, part one namely carbon is a classical walk through on most of the carbon allotropies from their discoveries to describing geometry ending with their properties and applications, while the second part is a brief on the metal matrix nanocomposites and the addition of multiwalled carbon nanotubes to enhance wanted properties and the challenges that come with. Chapter III describes the preparation procedures and the characterisations tools to firm a near complete analysis for the targeted properties. Whereas, chapter IV presents all experimental results accompanied by their interpretations.

Lastly, we finished with a conclusion tethering the obtained results and their interpretations.

II

LITTERATEUR REVIEW

II.A Carbon

> “Carbon, in fact, is a singular element . . .”
>
> Primo Levi, *The Periodic Table*

New Carbon allotropes are often mentioned as nanocarbon materials due to their nanoscale dimension which was impactful on carbon science and technology, and without any doubt, these materials have been the main core of nanoscience and nanotechnologies too. These carbon materials are found in a variety of forms such as graphite, diamond, carbon fibres, fullerenes, and carbon nanotubes. The key to carbon versatility in taking many structural forms, compared to other periodic table elements lies in its flexibility to bond with itself and other elements. This section introduces different carbon allotropies and describes their atomic nature.

II.A.1 Interatomic bonding in carbon

Carbon is the sixth element in the periodic table and it is a fascinating one in many ways. Its ability to bond with itself and other atoms in an endlessly varied combination of chains and rings forms the basis for the sprawling scientific discipline that is modern organic chemistry. One interesting aspect of carbon lies in the flexibility of configuring electronic states, thus bonding between neighbouring carbon atoms.

Carbon properties are a result of the electron arrangements surrounding the nucleus of the atom. The elemental carbon atom has six electrons shared evenly between the three energetic states corresponding to $1s^2$, $2s^2$, and $2p^2$ atomic orbitals. Each carbon atom has four valence electrons 2s, $2p_x$, $2p_y$, and $2p_z$ atomic orbitals, which are important in constituting covalent bonds in carbon materials. Compared with the binding energy of the valence bonds, the difference in energy between the 2p and 2s energy levels in the carbon atom is very small. So, the wave functions for these four valence electrons can easily mix, causing the redistribution of these four electrons in the 2s and three 2p atomic orbitals to raise the carbon's binding energy atom with its nearest neighbours. The mixture of 2s and 2p atomic orbitals is called the hybridization of orbitals. The mixture of a single 2s electron with one, two, or three 2p electrons is called sp^n hybridization with n = 1, 2, 3 [1, 2]. The hybridization between 2s and 2p atomic orbitals form three possible hybridizations: *sp*, sp^2, and sp^3. These bonding states induce specific structural arrangements so that *sp* bonding gives a linear chain structure (1-D) separated by an angle of 180°, *sp*^{2} bonding to planar structure (2-D) separated by an angle of 120°. In comparison, *sp*^{3} gives a regular tetrahedral structure (3-D) with an angle of 109.5°.

Carbon bonds can bind into two different types, a sigma (σ) bond and a pi (π) bond, each carbon atom has (n + 1) σ bonds in *sp*^{n} hybridization. These bonds form a particular n-dimensional structural arrangement. For example, two σ bonds form a one-dimensional (1D) chain structure in *sp* hybridization. In *sp*^{2} hybridization, three s bonds form a planar structure in graphite. Because graphite has strong in-plane trigonal bonding, it is the stable ground state of carbon under ambient conditions. The *sp*^{3} hybridization gives a regular three-dimensional (3D) tetrahedron called diamond structure. [3,4]

Table 2.1: Accepted bond lengths and energies for the *sp*, *sp*^{2} and *sp*^{3} C–C bonds

Bond	Length (pm)	Energy (kJ. mol^{-1})
sp C–C	121	837
sp^2 C–C	134	611
sp^3 C–C	154	347

Source: Kotz, J.C. and Purcell, K.F., *Chemistry & Chemical Reactivity*, Saunders College Publishing, 1987.

Note: These are example values, the actual lengths and energies do vary slightly between different materials.

II.A.2 Different carbon allotropes forms

Carbon in nature, in its solid phase, exists in three allotropic forms, graphite, diamond, and buckminsterfullerene. Carbon is a unique element that stands on top of the IV column in the periodic table, due to both type and numbers of bonds formed with itself and other various elements, which give it almost an endless possible combination.

Table 2.2: Isomers made of carbon

Dimension	0-D	1-D	2-D	3-D
isomer	fullerene C_{60}	nanotube	graphite	diamond
		carbyne	fibre	amorphous
hybridization	sp^3	sp^2 (sp)	sp^2	sp^3
density (g/ cm^3)	1.72	1.2-2.0	2.26	3.515
		2.68-3.13	~2	2–3
Bond Length (Å)	1.40 $(C = C)$	1.44 $(C = C)$	1.42 $(C = C)$	1.54 $(C - C)$
	1.46 $(C - C)$		1.44 $(C = C)$	
electronic properties	semiconductor E_g = 1.9 eV	metal or semiconductor	semimetal	insulating E_g = 5.47 eV

II.A.2.1 Graphite

Graphite is one of the longest known forms of pure carbon, naturally occurring on the surface of the earth as a mineral and it’s been used by humankind for centuries, it exists as a black solid containing an infinite diagonal of a hexagonal lattice of carbon sheet known as "graphene planes" following an AB Bernal stacking sequence in the most common form of graphite, the graphene sheet features covalent bonding in which three of the four valence electrons form strong directional interatomic covalent bonds (σ-bonds) to neighbouring atoms in the basal plane. The electrons in the σ-bonds are strongly bound into the bonds so they cannot move. The fourth valence electron, on the other hand, is responsible for weak van der Waals (π-bonds) between neighbouring atoms in other graphene layers. (Figure below); the distance between two consecutive planes is 3.35 Å.

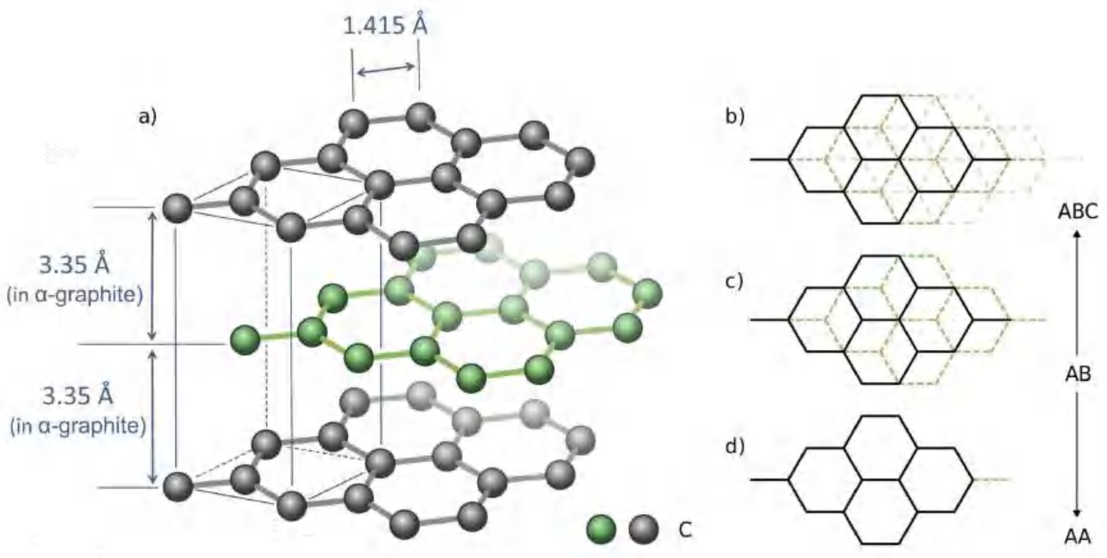

Figure. 2.1: Graphite structures. (a) Structure of α-graphite showing the offset of adjacent graphene layers that alternate in an AB pattern along with (b-d) additional stacking arrangements of the graphene layers. The AB stacking arrangement corresponds to α-graphite and the ABC arrangement to β-graphite

There is another existing graphite in symmetry rhombohedral [5], which has an ABC stacking sequence and it is consisting of three layers and a lattice constant of 10.05 Å, but this form of graphite is unstable compared to the earlier one. Graphite is available naturally or synthesized and it is considered the most thermodynamically stable form of carbon under ambient conditions (as is shown in figure 2.2).

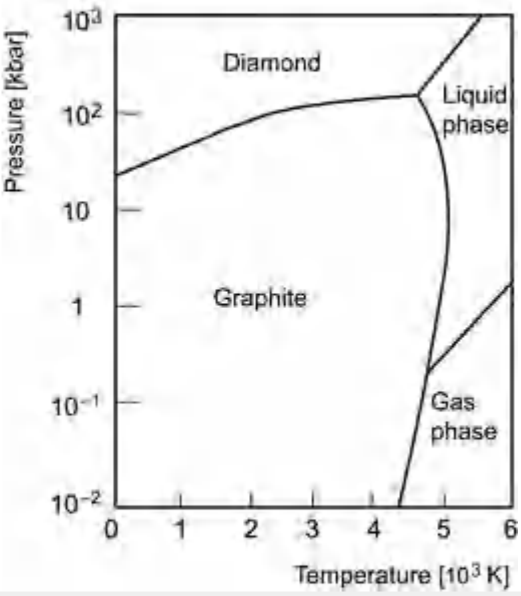

Figure. 2.2: Phase diagram of carbon.

Synthetic graphite is manufactured from organic precursors. The precursor is first subjected to a process of carbonization, consisting of progressive heating under an inert atmosphere up to reach temperatures of close to 1300 °C. At this stage, there remains amorphous carbon and polycrystalline graphite. Thermal treatment at 2500 °C then allows a graphitizing of this carbon to give the graphite.

In the graphite phase, the structure is highly anisotropic, exhibiting semi-metallic behaviour of very high conductivity in the plane of the individual graphene layers, whilst a poor conductivity in the direction normal to the graphene planes. In terms of mechanical properties, graphite is the stiffest material in nature (has the highest in-plane elastic modulus) and has the highest melting point (4200 K), with a superior thermal conductivity (3000 W/mK) and high room-temperature electron mobility (30,000 cm^2/Vs) [6,7].

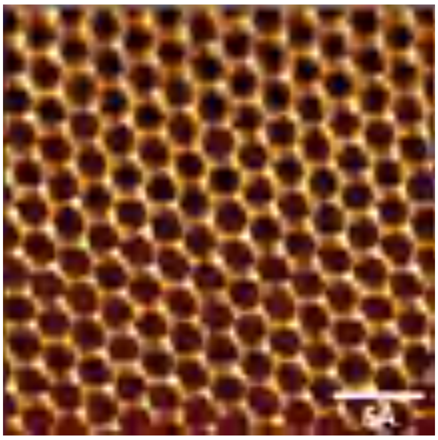

Figure. 2.3: STM image of graphite. Notice the different brightness for the A and B atoms, M.M. Lucchese et al [8].

II.A.2.2 Diamond

The diamond structure is probably the most thoroughly investigated of all crystallographic structures of carbon. Silicon and germanium, the most commonly used elemental semiconductors, also exhibit the same "diamond" structure and other important group 111-V or II-VI compound semiconductors (such as GaAs or CdTe) crystallize in the closely related zincblende structure, the fundamental difference between the zincblende and diamond structures being that the two constituent atomic species of the zincblende structure occupy each of the distinct sites in the diamond structure [9].

The ideal diamond structure is shown in figure. 2.4 has the characteristic of four other carbon atoms surrounding every carbon atom at the corners of a regular tetrahedron with a cube edge length of a_o= 3.567 Å, and this carbon atom is bonded to these neighbours by strong covalent sp^3 bonds.

The diamond structure is cubic and can be viewed as two interpenetrating fcc structures displaced by (1/4, 1/4, 1/4) a_0 along the body diagonal. The nearest-neighbour carbon-carbon distance is 1.544 Å, nearly 10% larger than in graphite. Yet, the atomic density of diamond (1.77x 10^{23} cm^{-3}) is 56% higher than in graphite, due to the high anisotropy of the graphite structure (see Table 2.1). The diamond crystal is highly symmetric with a cubic space group O_h^7 *(Fd3m)*. Although cubic and nearly isotropic, diamond cleaves along {111 planes, while highly anisotropic graphite cleaves along {002} planes [2]. There also exists a hexagonal form of diamond with a space group D_{6h}^4*(P6₃/mmc)*, the same as for graphite, but with different site locations. The packing in the hexagonal diamond is similar to the cubic diamond, except for a shift of one of the two carbon layers laterally along the {111} planes [10]. The c-axis unit vector for a hexagonal diamond is $(a_o/\sqrt{3})$ =2.06 Å, considerably smaller than the interplanar separation of 3.35 Å for graphite.

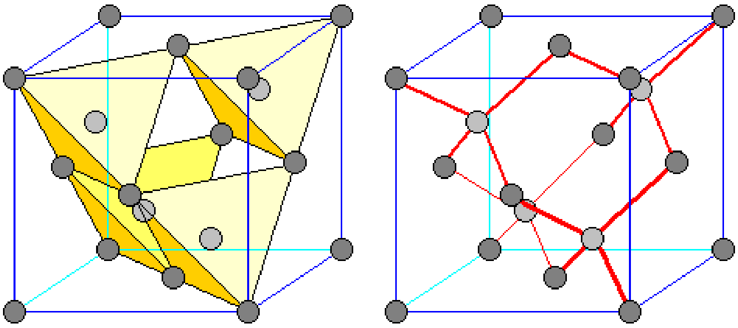

Figure. 2.4: The crystallographic unit cell (unit cube) of the diamond structure

Impurities in a diamond are critical because of the changes they induce in the electrical and thermal properties of the diamond; these modified properties find applications mainly in industrial processes. The best natural diamonds contain impurities with concentrations in the range ~ 1 part in 10^5. Only a few chemical species (e.g., B, N) can enter the diamond lattice substitutionally such substitutional impurities are very low (less than 1 part in 10^4). In contrast to the semi-metallic anisotropic graphite phase, diamond is an anisotropic, cubic, wide-gap (5.5 eV) insulator.

Table 2.3: Properties of graphite and diamond.

Property	Graphite[a]		Diamond
Lattice Parameter	Hexagonal		Cubic
Space Group	P6$_3$/mmc (D^4_{6h})		
Lattice constant[b] (Å)	2.462	6.708	3.567
Atomic density (C atoms/cm^3)	1.14x10^{23}		1.77x10^{23}
Specific gravity (g/cm3)	2.26		3.515
Specific heat (cal/g.K)	0.17		0.12
Thermal conductivity (W/cm. K)[c]	30	0.06	~25
Binding energy (eV/C atom)	77.4		
Debye temperature (K)	2500	950	1860
Bulk modulus (GPa)	286		42.2
Elastic modulus (GPa)	1060[d]	36.5[d]	107.6[e]
Compressibility (cm^2/dyn)	2.98x 10^{-12}		2.26x 10^{-13}
Mohs hardness[f]	0.5	9	10
Band gap (eV)	-0.04[g]		5.47
Carrier density (10^{18}/cm^3 at 4 K)	5		0
Electron mobility[b] (cm^2/V sec)	20.000	100	1800
Hole mobility[b] (cm^2/V sec)	15.000	90	1500
Resistivity (Ωcm)	50x10^{-6}	1	~10^{20}
Dielectric constant[b] (low ω)	3.0	5.0	5.58
Breakdown field (V/cm)	0	0	10^7 (highest)
Magnetic susceptibility (10^{-6} cm^3/g)	-0.5	-21	---
Refractive index (visible)	---	---	2.4
Melting point (K)	4450		4500
Thermal expansion (/K)	-1x10^{-6}	+29x10^{-6}	~1x10^{-6}
Velocity of sound (cm/sec)	~2.63x10^5	~1x10^5	~1.96x10^5
Highest Raman mode (cm^{-1})	1582	---	1332

[a] For anisotropic properties, the in-plane (*ab* plane or *a*-axis) value is given on the left and the *c*-axis value on the right.

[b] Measurements at room temperature (300 K).

[c] Highest reported thermal conductivity values are listed.

[d] in-plane elastic constant is Cu and c-axis value is C_{33}. Other elastic constants

[b] Measurements at room temperature (300 K).

for graphite are $C_{12} = 180$, $C_{13} = 15$, $C_{44} = 4.5$ GPa.

[e] For diamond, there are three elastic constants, Cu = 1040, $C_{12} = 170$, $C_{44} = 550$ GPa.

[f] A scale based on values from 0 to 10, where 10 is the hardest material (diamond) and 1 is talc [11].

[g] A negative band gap implies a band overlap, i.e., semi-metallic behaviour.

II.A.2.3 Fullerene

Harry Kroto, of the University of Sussex, and Richard Smalley, of Rice University, Houston, had different reasons for being interested in the synthesis of carbon clusters. Kroto had been fascinated since the early 1960s by the processes occurring on the surface of the stars.

A coalescence of research activities in two seemingly independent areas, astrophysicists were working in collaboration with spectroscopists [12] to identify some unusual infrared (IR) emission from large carbon clusters which were streaming out of red giant stars [13]. Smalley, on the other hand, has been working with his team for several years on the development of a laser vaporization cluster technique, concentrating chiefly on semiconductors such as silicon and gallium arsenide. But he was also keen on what might happen when one vaporises carbon and suggested the possibility of creating unusual carbon-based molecules or clusters that would yield the same IR spectrum on earth as is seen in carbon from red giant stars. This motivation led to the collaboration of the two scientists in August 1985 at Rice and with a group of colleagues and students, began the famous series of experiments on the vaporisation of graphite using a supersonic cluster beam apparatus. They were immediately struck by a surprising result. In the distribution of gas-phase carbon clusters, detected by mass spectrometry, the new carbon element was by far the dominant species [14].

The new element C_{60} with full icosahedral symmetry can be regarded as the first isolated carbon nanosystem, named *"buckminsterfullerene"* after the American architect Buckminster Fuller, whose geodesic dome resembles what was observed by the group of scientists including Smalley, Robert Curl, and Kroto. For their novel discovery; they shared a Nobel Prize in 1996. Other fullerenes were discovered shortly afterwards with more and fewer carbon atoms; they ranged from 18 atoms to up to hundreds of atoms. Buckyball containing 60 carbon atoms is the most popular. C_{60} remains the easiest to produce and the cheapest, with prices rising rapidly for other larger fullerenes.

Much subsequent research was devoted to the study of this new class of hollow-structured carbon clusters, [15–17] and in 1990, Krätschmer and his colleagues developed a contact arc discharge method for macroscopic production, known as the Krätschmer-Huffman method. They discovered that carbon rods heated resistively in a helium atmosphere cloud generate gram quantities of fullerenes embedded in carbon soot, which was also produced in the process. This method consists of graphite electrodes contact arcs passing an alternating or direct current through them in an atmosphere of helium in approximately 200 torrs. The evaporated graphite takes the form of soot, which is dissolved in a nonpolar solvent. The solvent is dried away and the C_{60} and C_{70} fullerenes can be separated from the residue. Optimal current, helium pressure and flow rate lead to yields of up to 70% of C_{60} and 15% of C_{70} with this method. Laser vaporization is also used for fullerene production. In a typical apparatus a pulsed Nd:YAG laser operating at 532 nm and 250 mJ of power is used as the laser source and the graphite target is kept in a furnace at 1200 °C. Finally, it should be mentioned that fullerenes have also been produced in sooting flames involving, for example, the combustion of benzene and acetylene, although the yields are low [18].

II.A.2.3.1 Structural overview

The structure of the C_{60} Buckyball is a combination of 12 pentagons and 20 hexagonal rings, forming a spheroid shape with 60 vertices for 60 carbon atoms. As the molecule structure depicted in the figure 2.5, which reveals how the pentagonal rings sit at the vertices of an icosahedron such that no two pentagonal rings are next to each other. The average C–C bond distance measured using nuclear magnetic resonance (NMR) is 1.44 Å. A diameter of 7.09 Å is calculated for the C_{60} based on the fact that the C–C distance is equal to 1.40 Å for the hexagon bonds and 1.46 Å for the pentagonal bond length [19].

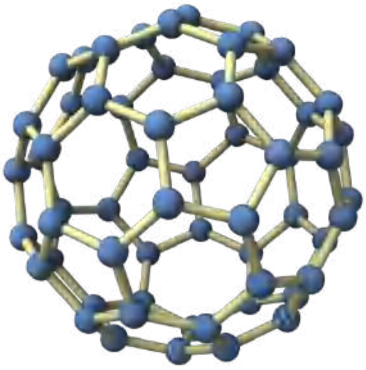

Figure. 2.5: C_{60} Molecular structure.

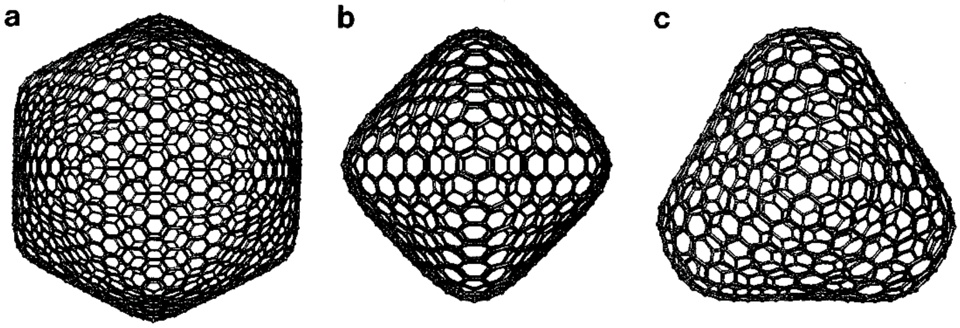

Figure. 2.6: Giant fullerene structures with various symmetries [20]. (a) C_{1500} (I_h symmetry), (b) C_{600} (D_{2h} symmetry), (c) C_{660} (tetrahedral symmetry).

II.A.2.3.2 Properties

The C_{60} displayed extraordinary physical properties such as resistance to great pressure and the ability to retain formal forms (shape memory) after being subjected to over 3,000 atmospheres. Theoretical calculations suggest that a single C_{60} molecule has an effective bulk modulus of 668 GPa when compressed to 75% of its size [21]. Such property makes fullerene even hardened than steel and diamond, whose bulk moduli are 160 GPa and 442 GPa, respectively.

II.A.2.3.3 Applications

Fullerene shows promising properties and versatility in a wide range of domains from:

- Organic Solar Cells due to the high electron affinity and superior ability to transport charge, low cost compared to silicon solar production and flexibility in production process makes Fullerenes the best acceptor component currently available and shipped within a great expectation for the use of organic cells in the advertising and packaging businesses involve autonomous luminous banners, large liquid crystalline displays and packaging for food.
- Hydrogen gas Storage has a unique molecular structure, fullerene seems to be the only form of carbon that potentially be chemically hydrogenated and de-hydrogenated reversible. When fullerenes are hydrogenated, the C=C double bonds become C-C single bonds and C-H bonds, the bond strength for the single bonds respectively are, 83 kcal/mol, 68 kcal/mol [22]. H-C bond is appreciably weaker than C-C bonds which under heat it will break first and the fullerene structure should be preserved. The considerably lower heat of formation for $C_{60}H_{36}$ as a molecule is more thermodynamically stable than C_{60}.
- Strengthening/Hardening of Metals offers unique opportunities to harden metals and alloys without seriously compromising their ambient temperature ductility. This is caused by their small size and high reactivity, which enable the dispersion strengthening of metallic matrices with carbide particles that result from in-situ interactions between fullerenes and metals [23].
- As Precursor to Diamond
- Based Sensors
- In Medicine, as a container

II.A.2.4 Carbon Nanotubes

Carbon in the sp^2 hybridization can form a variety of amazing and unique structures with exceptional mechanical, electrical, optical and thermal properties. Among the midst of carbon allotropes, carbon nanotubes have gained a great deal of interest. Despite the ongoing controversy about carbon nanotubes (i.e., filaments or whiskers) first occurring and by whom it was synthesized, this uncertainty still echoes here and there in the scientific community after the wide recognition of Iijima as the godfather of carbon nanotubes.

Indeed, Carbon nanotubes (CNTs) alike structures have long been synthesized as products of the action of a catalyst on the gaseous species originating from the thermal decomposition of hydrocarbons. Thus, in 1886, Hugues and Chambers patented a process for increasing the filaments of carbon " hair alike " from methane by vapour deposition. In France, two reports from the Academy of Sciences also mention the production of fibrils or filaments [24]. However, for all these works, the characterization techniques used do not make it possible to prove the filaments' tubular nature. It was not until 1939 and the appearance of the scanning electron microscope to see the first images of carbon fibrils. The first evidence that the nanofilaments produced in this way were nanotubes – that they exhibited an inner cavity – can be found in the transmission electron microscope micrographs published by Radushkevich and Lukyanovich in 1952, while working with Dubinin on the adsorption of carbonaceous (e.g., materials produced by combustion of coal) on transition metals. They noticed that in some cases the structures formed were quite unusual, leading to the detailed study published in the same year. The work was done at the Institute of Physical Chemistry, USSR Academy of Science; its significance was not recognized (the concept of “nanotechnology” did not exist in the 1950s) and indeed the work was not widely read in the west simply due to the fact it was published in Russian [25]. In addition, in the 1970s it has been identified in the core structure of vapour-grown carbon fibres as very small carbon filaments [26–28]. Since then, the interest in carbon nanofilaments/nanotubes was recurrent, though within a scientific area almost limited to the carbon material scientist community. These discoveries will not find the audience or the repercussions that Iijma was able to find in 1991.

Apart from the well-known graphite, carbon also can build closed and open cages with honeycomb atomic arrangement. The first such structure to be discovered was the C_{60} molecule by Kroto et al. [29]. Although various carbon cages were studied, it was in 1991 when Iijima [30] using the same arc process to synthesis fullerene, reported a by-product of carbon fibrils described as a hollow monolithic tubular structure of the same analogues as the buckyball and it contained multiple tubes or shells like a Matryoshka doll, one within another which he interpreted as carbon nanotubes (figure 2.7). The new material called multi-walled carbon nanotubes (MWNTs) consisted of up to several tens of graphitic shells (graphene to be discovered later on) with adjacent shell separation of ~0.34 nm, diameters of ~1 nm and a large length/diameter ratio. But the real breakthrough occurred two years later when attempts to fill the nanotubes in situ with various metals led to the discovery – again unexpected – of single-wall carbon nanotubes (SWNTs) simultaneously by Iijima and Ichihashi [31] and IBM team headed by Bethune [32]. Single-walled carbon nanotubes (SWNTs) consisted of a single rolled layer of graphene and they were new nano-objects with properties and behaviours that are often quite specific, not to mention that both SWNTs and MWNTs are formed with open or closed ends.

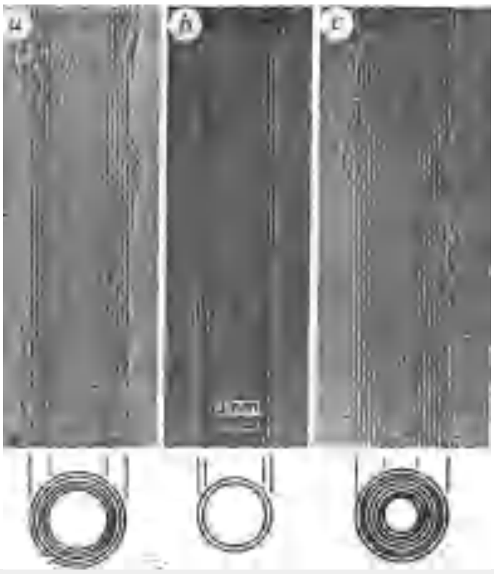

Figure. 2.7: The first electron micrographs to be identified as carbon nanotubes. The images are of MWCNTs. In (a) the MWCNT has 5 shells and a diameter of 6.7 nm. In (b) the MWNT has 2 shells and a diameter of 5.5 nm. In (c) the MWNT has 7 shells and a diameter of 6.5 nm. (Courtesy goes to S. Iijima and Nature from [30], © 1991 Macmillan Magazines, Inc.)

II.A.2.4.1 Structural overview

This section provides a brief introduction to the unusual structural properties of single-wall carbon nanotubes, that emphasize their unique (1D) attribute and sets them apart from other nanomaterials systems. A perfect single-wall carbon nanotube (SWNT) can be described as a single graphene sheet rolled into a seamless cylindrical shape so that the structure is quasi-one-dimensional with axial symmetry which generally exhibits a spiral conformation, it consisted of one atom thick, usually with a small number (perhaps 10–40) of carbon atoms along the circumference and a long length (microns) along the longitudinal axis [33]. The chirality, as defined here, is given by a single vector called the chiral vector C_h. To specify the structure of carbon nanotubes, we define several important vectors, which are derived from the chiral vector.

$$\boldsymbol{OA} = \boldsymbol{C_h} = na_1 + ma_2 \equiv (n, m), \quad (n, m \text{ are integers, } 0 \leq |m| \leq n).$$

with

$$a_1 = \frac{a\sqrt{3}}{2}x + \frac{a}{2}y \ \text{ and } a_2 = \frac{a\sqrt{3}}{2}x + \frac{a}{2} - y,$$

where $a = 2.46$ Å, and

$$\cos\theta = \frac{C_h a_1}{|C_h||a_1|} = \frac{2n+m}{2\sqrt{n^2+m^2+nm}}$$

where is often described by the pair of indices (n, m) that denote the number of unit vectors na_1 and na_2 in the hexagonal honeycomb lattice contained in the vector $\overrightarrow{\boldsymbol{OA}}$.

The vector of helicity C_h (= $\boldsymbol{OA}$) is perpendicular to the tube axis, while the angle of helicity θ is taken with respect to the so-called zigzag or a_1 direction axis [34], the vector of helicity that results in nanotubes of the zigzag type (see Figure 2.8).

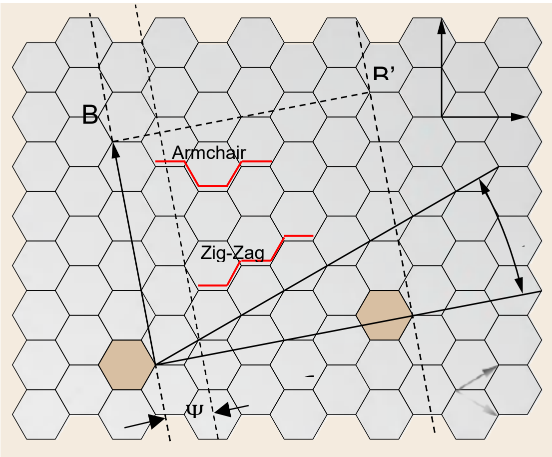

Figure. 2.8: The unrolled honeycomb lattice of a nanotube. When we connect sites O and A and sites B and B′, a portion of a graphene sheet can be rolled seamlessly to form an SWNT. The vectors $\overrightarrow{\mathrm{OA}}$ and $\overrightarrow{\mathrm{OB}}$ define the chiral vector C*h* and the translational vector *T* of the nanotube, respectively. The rectangle OAB′B defines the unit cell for the nanotube. The Figure is constructed for an (*n*, *m*) = (4, 2) nanotube [36].

The diameter *D* of the corresponding nanotube is related to C_h by the relation

$$D = \frac{|C_h|}{\pi} = \frac{a_{cc}\sqrt{3(m^2 + mn + n^2)}}{\pi}$$

where a_{cc} is the nearest-neighbour C–C distance

$$\underset{\text{(Graphite)}}{1.41\ \text{Å}} \le a_{C=C} \le \underset{(\text{C}_{60})}{1.44\ \text{Å}}$$

The C–C bond length is elongated by the curvature imposed by the structure; the average bond length in the C_{60} fullerene molecule is a reasonable upper limit, while the bond length in flat graphene in genuine graphite is the lower limit (corresponding to an infinite radius of curvature). Since C_h, θ, and *D* are all expressed as a function of the integers *n* and *m*, they are sufficient to define any particular SWNT by denoting them (*n*, *m*). The values of *n* and *m* for a given SWNT can be simply obtained by counting the number of hexagons that separate the extremities of the C_h vector following the unit vector a_1 first and then a_2 [35]. In the example of Figure. 2.9, the SWNT that is obtained by rolling the graphene so that the two shaded aromatic cycles can be superimposed exactly is a (4,2) chiral nanotube. Similarly, SWNTs from Figure. 2.10 a–c is (9,0), (5,5), and (10,5) nanotubes respectively, thereby providing examples of zigzag-type SWNT (with an angle of helicity = 0°), armchair type SWNT (with an angle of helicity of 30°), and a chiral SWNT, respectively.

The diameter of the carbon nanotube, d_t is given by L/π, in which L is the circumferential length of the carbon nanotube:

$$d_t = L/\pi \, , L = C_h = \sqrt{C_h . C_h} = a\sqrt{n^2 + m^2 + nm}$$

It is noted here that a_1 and a_2 are not orthogonal to each other and that the inner products between a_1 and a_2 yield:

$$a_1 . a_1 = a_2 . a_2 = a^2, \qquad a_1 . a_2 = \frac{a^2}{2}$$

Figure. 2.9: Sketches of three different SWNT structures that are examples of **(a)** a zigzag-type nanotube (5,5), **(b)** an armchair-type nanotube (9,0), **(c)** a helical nanotube (10,5).

Figure. 2.9 shows the terminations of each of the three nanotubes. The terminations are often called caps or end caps and consist of a "hemisphere" of a fullerene. Each cap contains six pentagons and an appropriate number and placement of hexagons that are selected to fit perfectly to the long cylindrical section.

II.A.2.4.2 Properties

- Adsorption properties due to the accessible specific surface area of CNTs (*reactivity*), [37,38] have highlighted the porous nature of both SWCNTs and MWCNTs. The theoretical surface area ranges from 50–1315 $m^2.g^{-1}$ depending on the number of walls, the diameter, the density of tubes [39]. Experimentally, the surface area of an SWNT is often larger than that of an MWNT, of 400–900 $m^2.g^{-1}$ compared to 200–400 $m^2.g^{-1}$. Although SWCNTs belong to the graphene-based materials family, unlike graphite, they have no (chemically active) dangling bonds. Yet it is believed that the chemical reactivity of SWCNTs (and MWCNTs) are derived mainly from caps at the end of each tube which represent in itself a hemisphere fullerene containing sites that are created at the concave surface and physisorption sites are created on the convex surface, both with an adsorption efficiency that increases with the diameter decreases.
- Carbon nanotubes (CNTs) have excellent thermal conductivity, stable electrical resistance in the presence of high currents densities (max. 10^9 A/cm^2) about three orders of magnitude higher than Cu, as well as superior mechanical properties [33,40]. Thermal conductivity depends on the axial directions, in the CNT case both longitudinal and radial thermal conductivity were assumed to be 3000 $W\ m^{-1}\ K^{-1}$ [41] and 5.5 $W\ m^{-1}\ K^{-1}$ [42], respectively.
- Mechanically, Carbon nanotubes are the strongest and stiffest materials yet to be discovered in terms of tensile strength and elastic modulus respectively. This strength is a result of the covalent bond sp^2 bonds of the curved graphene sheet, which is stronger than in diamond (sp^3 hybridization; 0.142 nm versus 0.154 nm for the C–C bond length in graphene and diamond respectively), these values can be affected by the presence of defects and disorder in the sidewalls. The Young modulus of an SWCNT is estimated to have a value as high as 1 to 1.8 TPa.

Table 2.4: Summary of experimental measurements of mechanical properties of CNTs.

Methods	Remarks	Ref
Amplitude of thermal vibrations of CNTs at different temperatures in a TEM	E = 0.4–4.15 TPa Avg. = 1.8 TPa	[43]
Same as 1 for SWCNTs	E = 1.3–0.4/+0.6 TPa	[44]
Force-displacement curve of pinned CNT using AFM	E = 1.28 ± 0.59 TPa	[45]
Shifts in *D** peaks of the Raman spectra of CNT in epoxy composites	E = 2.8–3.6 TPa for SWNT and 1.7–2.4 TPa for CNT	[46]
Frequency of electromechanical resonances	E = 0.1–1 TPa for CNT	[47]
Bend test of simply supported CNT	E = 870 GPa for arc CNT and 27 GPa for CVD CNT	[48]
Same as 6 for SWCNT ropes	E = 1 TPa	[49]
Tensile test of CNT in SEM	E = 270–950 GPa Strength = 11–63 GPa	[50]
Same as 8 for SWNT ropes	E = 320–1470 GPa Strength = 13–52 GPa	[51]

II.A.2.4.3 Applications

In MWCNTs that consist of stacked graphene's, the bond strength varies significantly depending on whether the in-plane direction (characterized by very strong covalent and therefore very short – 0.142nm – bonds) or the direction perpendicular to it (characterized by very weak van der Waals and therefore very loose – ≈ 0.34 nm – bonds) is considered. Such heterogeneity is not found in single SWCNTs. However, the heterogeneity returns, along with the related consequences, when SWCNTs associate into bundles. Therefore, the properties – and applicability – of SWCNTs may also change dramatically depending on whether single SWCNTs or SWCNT ropes are involved.

Perfect CNTs exhibit a high aspect ratio, high tensile strength, low mass density, high heat conductivity, large surface area, poor chemical reactivity, and versatile electronic behaviour, including high electron conductivity. While these are the characteristics of individual CNTs, many of the secondary structures such as ropes, fibres, papers, and thin films with aligned tubes, all with the specific properties that make them a potential candidate for a nearly infinite variety of applications, regardless of their cost [52].

- Due to the high mechanical strength and aspect ratio, CNTs almost ideal candidates for use as force sensors in scanning probe microscopy (SPM) [53,54].
- Proven to be efficient electron field emitters with higher stability, higher mechanical resistance, longer lifetimes, and 1/3 – 1/10 lower energy consumption [55].
- Flexible and touch-screen displays [56].
- Non-volatile random-access memory (NRAM) [57]. The devices reach a switching speed of 100–200 GHz, operate at orders of magnitude than flash memories, and present lower power consumption to dynamic random-access memories (RAMs).
- Light absorbents, Surrey NanoSystems create and sell a coating called Vantablack that absorb 99.6% of light (it is not a painting, but it is claimed to be the darkest black colour available), which is useful in optical devices for instance.
- The automotive and aeronautic industry used to enable electrostatic-assisted painting of polymer parts such as mirror housings and bumpers [58], CNT-polymer composites used as an anticorrosion coating for metals. CNTs enhance the mechanical and tribological properties of coatings while providing an electric pathway for cathodic protection [59].
- High-Tech goods and clothes such as baseball bats, tennis and badminton racquets, racing bicycles, skis, and archery arrows. Far from sports issues yet a serious matter nowadays, CNT sheets are applied in light armours and projectile protection wearables reducing the weight of the finished products.
- Anodes for Li-Ion batteries, CNTs are excellent conductive additives for Li-ion batteries [60]. The measured reversible Li-ion capacities for CNT-based anodes can exceed 1000 $mAhg^{-1}$, which is a 3-fold improvement over conventional graphite anodes [61], also improving cyclic efficiency of graphite anode was maintained at almost 100% for up to 50 cycles by adding 10 wt% MWCNTs [62].
- Chemical sensors.
- Catalyst support.

II.A.2.5 Graphene

The 2010 Nobel Prize in Physics was awarded to two scientists Andre Geim and Konstantin Novoselov [63] for their ground-breaking work on graphene, which is gaining weight in the scientific community worldwide till nowadays, due to its exceptional mechanical, thermal, optical, and electrical properties [64–69].

Graphene in a nutshell is a polyaromatic monoatomic layer consisting of sp^2-hybridized carbon that is tightly packed into a 2-D honeycomb lattice with a thickness of ~ 0.335 nm (see figure 2.10). The past decade witnessed great interest and research-oriented toward graphene. For example, graphene was reported to outperform carbon nanotubes (CNTs) in room-temperature heat conduction [65], and it has extremely high electron mobility at ambient temperature with a resistivity of 10^{-6} Ω cm, which is comparable to, or even lower than that of, silver (1.62×10^{-6} Ω cm), a material widely known for its lowest resistivity. Moreover, electron transport in graphene remains ballistic up to 0.3 µm at 300 K [69]. The extraordinary and outstanding properties of graphene make it a promising candidate for a wide range of applications, including field-effect transistors (FETs), composite materials, field emitters, chemical sensors, biosensors, hydrogen storage media, and transparent conductive electrodes [70–79].

The extraordinary properties the graphene possessed makes it a focus of intense scientific research. It had been reported an exceptional value such as ballistic electron mobility with theoretical limit: $\sim 2 \times 10^5$ cm^2 V^{-1} s^{-1} [71]; experimentally measured to be 2.53×10^5 cm^2 V^{-1} s^{-1} [80], high thermal conductivity (5000 W/m^{-1} K^{-1}), Young’s modulus (~1100 GPa), fracture strength (125 GPa) [69], a high specific area (~2630 m^2/g) [81], and optical absorption of exactly $\pi\alpha \approx 2.3\%$ (in the infrared limit, where α is the fine structure constant) [74].

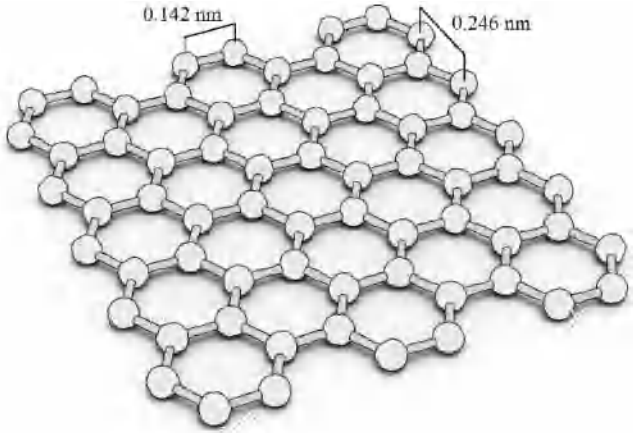

Figure. 2.10: Illustration of a graphene sheet.

II.A.2.6 Carbynes

Little is known about the *sp* hybridization of the linear acetylenic carbon [82], known as *carbyne*, which is a polymeric form of carbon consisting of chains $(-\mathrm{C} \equiv \mathrm{C}-)_n$ for n > 10. A longstanding study postulated the impossibility of preparing this truly one-dimensional (1D) material. Due to its extreme instability in ambient conditions, the same had been foreseen for graphene on account of its thermodynamic instability. The theoretical existence of carbyne has been known for quite some time. Carbyne was first proposed in 1885 by Adolf von Baeyer who described the existence of linear acetylenic carbon. However, carbyne is an extremely unstable form of carbon, so its existence could not be confirmed until it was isolated recently.

Carbyne has attracted much interest and a significant controversy [83–86] since the 1960s, but its identification remained questionable for years in the scientific community, but we will revisit dedicated literature for this.

This carbon structure is stable at high temperature and pressure as indicated in the phase diagram of carbon suggested by Bundy [87]. Figure. 2.11 as shock-quenched phases.

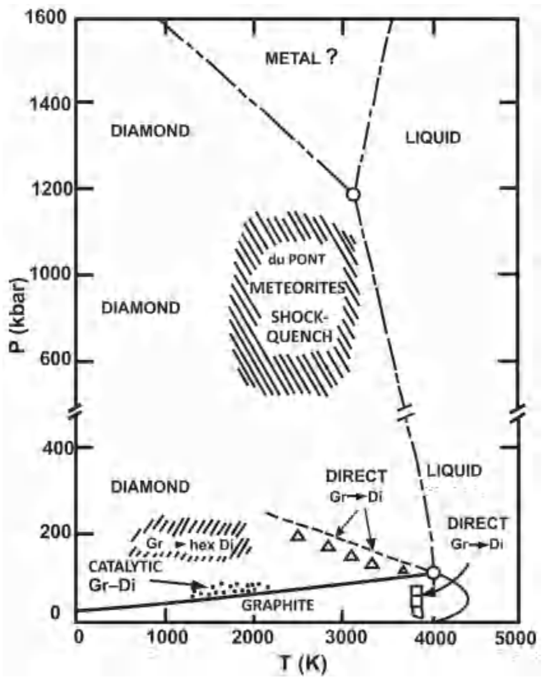

Figure. 2.11: One version of the phase diagram of carbon was suggested by Bundy [87]. The diamond (Di) and graphite (Gr) phases are emphasized in this figure. Other phases shown in the diagram include hexagonal diamond and a high temperature-high pressure phase, denoted in the diagram by du Pont, meteorites and shock-quench, which has not been studied in much detail and may, in part, be related to carbynes. Liquid carbon, which has been studied at low pressures and high temperatures, and an unexplored high-pressure phase, which may be metallic, are also indicated in the figure.

Carbynes are silver-white and are found in meteoritic carbon deposits, where the carbynes are mixed with graphite particles. Synthetic carbynes have also been prepared by sublimation of pyrolytic graphite [88,89]. It has been reported that carbynes are formed during very rapid solidification of liquid carbon, near the surface of the solidified droplets formed upon solidification [90]. Some researchers [91-93], have reported evidence that these linearly bonded carbon phases are stable at temperatures ranges 2700 <T< 4500 K.

Carbynes were allegedly first identified in samples found in the Ries crater in Bavaria [94] and were later synthesized by the dehydrogenation of acetylene [89]. The carbynes have been characterized by x-ray diffraction, scanning electron microscopy (TEM), ion micro-mass analysis, and spectroscopic measurements which show some characteristic features that identify carbynes in general and specific carbyne polymorphs in particular.

The crystal structure of carbynes has been studied by x-ray diffraction through identification of the Bragg peaks with those of synthetic carbynes produced from the sublimation of pyrolytic graphite [91]. In fact, two polymorphs of carbynes (labelled α and β) have been identified, both being hexagonal and with lattice constants a_{α} = 8.94 Å, c_{α}= 15.36 Å; a_{β}= 8.24 Å, c_{β} = 7.68 Å [89]. application of pressure converts α phase into the β phase. The numbers of atoms per unit cell and the densities are, respectively, 144 and 2.68 g/cm^3 for the α phase and 72 and 3.13 g/cm^3 for the β phase [95]. These densities determined from x-ray data [89] are in rough agreement with prior estimates [96]. It is expected that other less prevalent carbyne polymorphs should also exist. In the solid form, these carbynes have a hardness intermediate between diamond and graphite. Because of the difficulty in isolating carbynes in general, and specific carbyne polymorphs in particular, little is known about their detailed physical properties.

The recent reports [97] of feasible synthesis routes have inspired revisiting carbyne from both theoretical and experimental points of view. Carbyne's theoretically anticipated strength, elastic modulus and stiffness are greater than any known material, including diamond, carbon nanotubes and graphene, this structure of carbon gives an impressive Young’s modulus of 32.7 TPa, which is forty times that of diamond, and thirty times that of carbon nanotubes, such breakthrough allows one to envisage new composite materials [98].

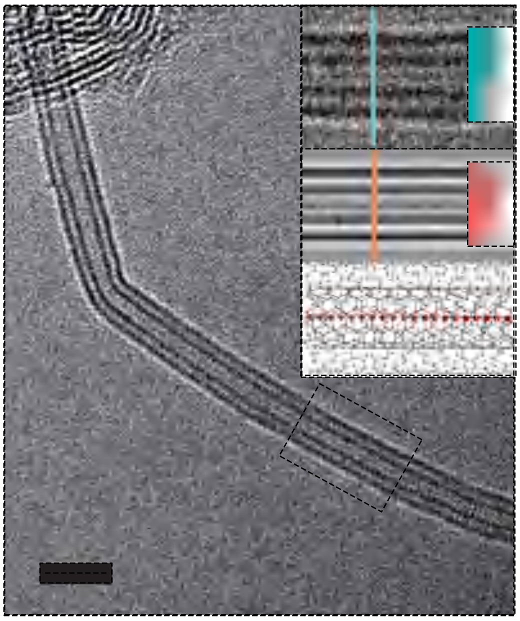

Figure. 2.12: HRTEM image of an LLCC (long linear carbon chains) and DWCNT with bending. The LLCC inside a DWCNT is longer than 26 nm, which means that it consists of more than 200 contiguous carbon atoms [97]. © Nature Materials

II.A.2.7 Graphyne

Graphyne with its own family is a new joiner to carbon allotropes having a 2D form with both *sp* and sp^2 hybridization. In recent years graphyne with different structures have risen interest from experimental and theoretical communities, since the first successful synthesis of graphdiyne, which is a typical member of the graphyne family. In 1987, Baughman et al. theoretically proposed graphyne and the graphyne-family members (GFMs) [99], which are new forms of carbon with one-atom-thickness. These structures can be constructed by either partially or completely replacing the C–C bonds in graphene with acetylenic groups $-C \equiv C -$.

The structure of graphyne can be viewed as a 2D network of hexagonal carbon rings (sp^2 hybridized) connected by acetylenic linkages (*sp* hybridized), as presented in Figure. 1(a). To distinguish from other graphyne family members, this structure is often referred to as -graphyne in many works of literature. But in the original paper of Baughman, he mentioned it as graphyne. It has a hexagonal symmetry similar to that of graphene.

The length of the acetylenic linkages can be different, leading to the graphyne-*n* structures, in which n indicates the number of $-C \equiv C -$ bonds in the linkage (Figure. 1(a)). Graphdiyne (graphyne-2) is the first experimentally accessible member in the graphyne family [100]. Compared with graphene, the graphyne-*n* structures show weaker stability, because inserting the acetylenic linkages into the carbon network reduces the cohesive energy. Among the graphyne-n structures, graphyne is predicted to be the most stable, and the cohesive energy decreases as the length of acetylenic linkage increases [99].

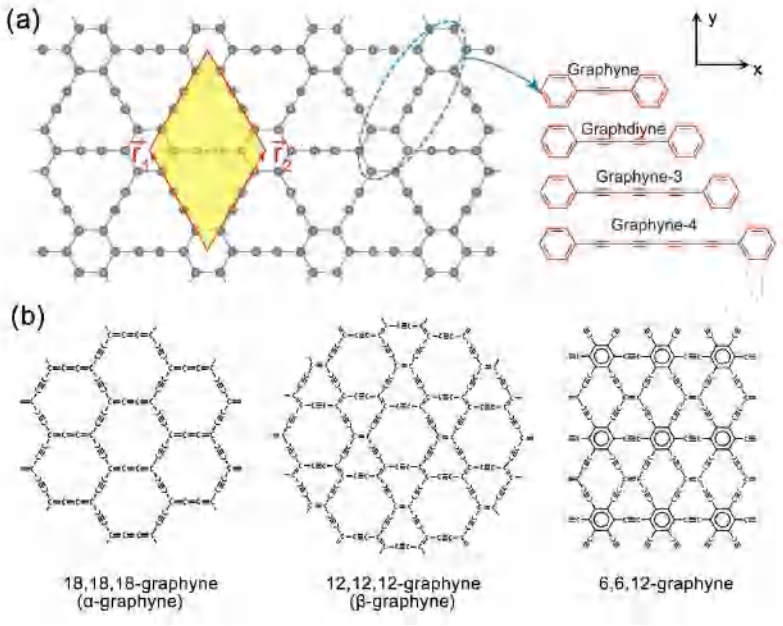

Figure. 2.13: (a) Illustration of the graphyne-*n* structures. [101] © 2013 American Chemical Society. (b) Structures of *α*-graphyne, *β*-graphyne, and 6,6,12-graphyne. [99] © AIP Publishing

The coexistence of *sp* and *sp*2 hybridization in graphyne-n results in different C–C bonding types. In graphyne, there are three types of C–C bonds: The C(sp^2)–C(sp^2) bond with a length of 1.43 Å, the C(sp^2)–C(*sp*) bond with a length of 1.40 Å, and the C(*sp*)≡C(*sp*) bond with a length of 1.23 Å. In graphyne-*n* with *n* larger than 1, besides the above three types of bonds, there are another C(*sp*)–C(*sp*) bond that connects two C(*sp*)≡C(*sp*) bonds, and its length is 1.33 Å [102].

Besides the graphyne-n structures, Baughman et al. also proposed that *sp* and sp^2 carbon atoms can form 2D networks with different arrangements, thus the graphyne family members can have many other structures. These structures are indicated as α, β, γ-graphyne [99]. Here α and β are the numbers of C atoms in the smallest and next to smallest rings which are connected by acetylenic linkage, whereas γ is the number of C atoms in a third ring connected to the β through acetylenic linkage. With different α, β and γ, the structure can have a different ratio of *sp* and sp^2 carbons, as well as different symmetry. In Figure. 1(b) the structures of three α, β, γ-graphynes are given, namely 18,18,18-graphyne, 12,12,12-graphyne, and 6,6,12-graphyne. The symmetries of the former two structures are hexagonal, whereas 6,6,12-graphyne possesses rectangular symmetry. The 18,18,18-

graphyne and 12,12,12-graphyne are often referred to as α -graphyne and β -graphyne [103].

While their mechanical properties exhibit significantly reduced ultimate strength compared with graphene, on the other hand, for electronic properties, GFMs possessed a nonzero bandgap, which is absent in graphene and the calculated bandgap of the graphyne-n structures is around 0.5 eV [102,104], and only show weak dependence on n [101,102].

II.A.3 Carbon nanotubes synthesis techniques

Nowadays, MWCNTs and SWCNTs are produced mainly by three techniques: arc-discharge, laser-ablation, and catalytic growth. Yet we discussed other techniques and methods for versatility.

One route to produce CNTs is to vaporize a solid carbon source (usually graphite), which requires processes able to generate high temperatures (T > 5000 K). Various techniques have been employed for this (e.g., laser ablation, DC electric arc, solar furnace). We will focus here on the DC electric-arc technique, as the other methods have been almost abandoned for being less robust and versatile. Some information on the other techniques will be provided.

The DC electric-arc process is based on carbon vaporization in an inert gas atmosphere at reduced pressure. The morphologies of the carbon nanostructures and the SWNT yields can differ notably concerning the experimental conditions. It was (and still is) the first method of producing fullerenes in relatively large quantities [105-107].

II.A.3.1 Electric arc discharge

The electric arc discharge method was the first recognized method for producing both SWCNTs and MWCNTs. This method is similar to the Kratschmer–Huffman method of generating fullerenes and the procedure to make carbon whiskers developed by Roger Bacon over 30 years ago (Figure 2.14) [108]. Arc discharge synthesis uses a low-voltage (~12 to 25 V), high-current (50 to 120 amps) power supply (an arc welder can be used). An arc is produced across a 1-mm gap between two graphite electrodes 5 to 20 mm in diameter. An inert gas such as He or Ar is used as an atmosphere for the reaction, at a pressure of 100 to 1000 torr. Iijima produced the first MWCNTs by this method [30]. He found that nanotubes formed on the cathode, along with soot and fullerenes. MWCNTs produced by arc discharge are very straight due to their high crystallinity. For the growth of SWCNTs, transition metal catalysts are needed in the arc discharge [109]. demonstrated large-scale production of SWCNTs using arc discharge method with a good optimization been able to achieve gram quantities. The yield of SWCNTs (70-90%) was improved by using a carbon anode containing 1 at. % Yttrium and 4.2 at. % Nickel as a catalyst. However, the crude CNTs synthesized by this technique require extensive purification to remove the soot and catalytic metal particles.

Open-air synthesis of CNTs with welding arc torch and synthesis of MWCNTs in liquid nitrogen have been reported, in which low pressure or/and expensive inert gas can be avoided. These methods are promising routes for the economic production of CNTs [110,111].

Several factors are important in producing a good yield of high-quality nanotubes. Perhaps the most important is the pressure of the helium in the evaporation chamber, as demonstrated by Ebbesen and Ajayan in their 1992 paper [112].

Another important factor in the arc-evaporation method is the current, as demonstrated in several studies [113,114]. Too high a current will result in a hard, sintered material with few free nanotubes. Therefore, the current should be kept as low as possible, consistent with maintaining a stable plasma. Efficient cooling of the electrodes and the chamber has also been shown to be essential in producing good quality nanotube samples and avoiding excessive sintering, as discussed in the next section.

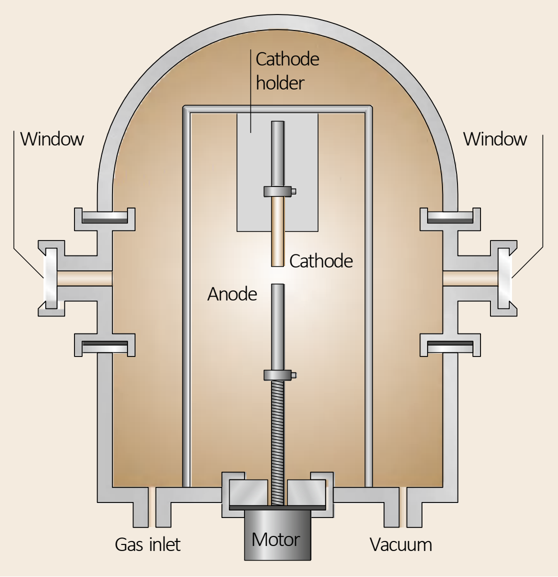

Figure. 2.14: Schematic illustration of arc-evaporation apparatus for the production of fullerenes and nanotubes.

II.A.3.2 Chemical vapour deposition (CVD)

CVD was first reported to produce defective MWCNTs in 1993 by Endo et al [115]. In 1996 Dai in Smalley's group successfully adapted CO-based CVD to produce SWCNT at Rice University [116]. While the arc method is capable of producing large quantities of unpurified nanotubes, significant effort is being directed toward production processes that offer more controllable routes to nanotube synthesis, CVD seems to offer the best chance of obtaining a desired controllable process for the selective production of nanotubes with defined properties such as higher atomic quality and higher per cent yield compared with other methods currently available [117–119]. For instance, it has been reported that decompose C_2H_2 over SiO_2-supported Fe catalysts to produce very long CNTs (~2 mm) [120]. These nanotubes were reported to be produced at very high purity, in well aligned arrays, and uniformed lengths, although it should be noted that such results have not been repeated elsewhere. It produces individual aligned SWCNTs on SiO_2 substrates for use in electronics and also vertical aligned MWCNTs for use as high-performance field emitters [121]. An illustration of a typical CVD process for the generation MWNTs is shown in Figure. 2.15.

CVD is a catalytically driven process, wherein a thermal decomposition of a hydrocarbons vapour over a dispersed Fe catalyst that is deposited in situ on quartz substrates. The synthesis apparatus consists of a quartz tube reactor inside a combined preheater and furnace set up. A syringe pump allows the continuous injection of a xylene-ferrocene liquid into a preheat section that is operated at ~200 °C. The xylene-ferrocene vapours are carried from the preheater into the reaction zone of the furnace by an Ar/ 10% H_2 carrier gas that also controls the partial pressure inside the quartz tube reactor. The reaction temperatures are typically in the range of 550 to 1200 °C. The MWNTs grow perpendicular to the quartz surfaces and form thick mats that are readily harvested. This process produces highly pure aligned MWNTs at a carbon yield approaching 60% of all carbon feed converting to nanotube products. Similarly, CVD processes sometimes utilize a feed of $Fe(CO)_5$ for in situ catalysts production [117].

The most common metals used in the growth of both SWCNTs and MWCNTs are Fe, Co, and Ni. While Fe and Ni, respectively are most used as a single catalyst for MWCNTs growth by CVD [119,122,123–127]. However, bimetallic catalysts consisting of Fe, Ni, or Co and some rare-earth metals have also been studied [128]. Although bimetallic catalysts are predominately used for the generation of SWNTs, they have been successful in catalysing the CVD growth of MWNTs as well. In one study, Pd, Cr, and Pt are investigated as modifiers to Co-Ni catalysts [129]. The Nanotubes produced at 550 °C from C_2H_2 with Pd modified catalyst are primarily straight with bamboo structure, while Cr yields curled nanofiber, and graphite whiskers are produced with Pt addition.

A variety of gaseous and liquid hydrocarbon feedstocks are used to produce nanotubes via thermal catalytic decomposition. These range from light gases such as C_2H_4 and C_2H_2 to heavier aromatic liquids like xylene [119] or benzene [130]. Similarly, MWNTs are formed using Fe-Co catalysts supported on SiO_2 by the decomposition of C_2H_2, C_2H_4, C_3H_6, acetone, C_5H_{12}, CH_3OH, toluene, and CH_4. Acetylenes, olefins, and molecules that decompose to generate olefins are all suitable feedstocks for nanotube formation. Liquid feeds such as benzene or xylene are used as a means of simultaneously introducing the metal catalysts, either by spray pyrolysis, [124] continuous liquid injection, [119] or aerosol delivery [125].

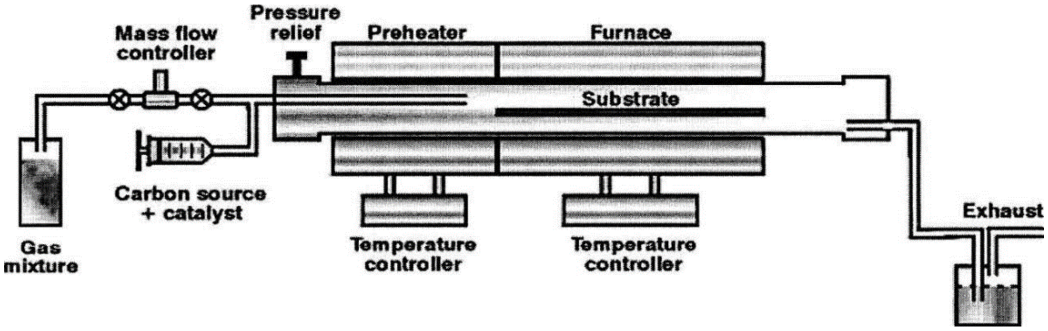

Figure. 2.15: Schematic of a CVD reactor. This reactor uses a 2-zone furnace and a liquid hydrocarbon feed. MWNT growth occurs on the quartz tube wall and the substrate [119].

II.A.3.3 Laser ablation

The first large-scale (gram quantities) production of SWCNTs was achieved in 1996 by Smalley and co-workers at Rice University (Figure 2.16) [131]. The laser ablation technique uses a 1.2 at. % of cobalt/nickel with 98.8 at. % of graphite composite target that is placed in a 1200 °C quartz tube furnace with an inert atmosphere of ~500 Torr of Ar or He and vaporized with a laser pulse. A pulsed- or a continuous-wave laser can be also used. Nanometre-size metal catalyst particles are formed in the plume of vaporized graphite. The metal particles catalyse the growth of SWCNTs in the plasma plume, at the same time by-product are formed. The nanotubes and by-products are collected via condensation on a cold finger downstream from the target. The SWCNTs self-organized into "ropes", which consist of between 100 to 500 tubes in a two-dimensional triangular lattice, due to van der Walls forces. The by-products of this synthesis are graphitic and amorphous carbon, "bucky onions" (concentric fulleroid spheres) surrounding metal catalyst particles and small fullerenes (C_{60}, C_{70}, etc.) [132]. Reported a high production rate of SWCNTs at ~1.5 g/hr using ultrafast laser pulses at 20% power of a free-electron laser. The production rate of SWCNTs is increased to ~45 g/hr if the power of the ultrafast laser pulses is running at maximum. A 2 KW continuous wave CO_2 laser ablation was used to produce SWCNT soot at a rate of 5 g/hr [133].

Both arc-discharge and laser-ablation techniques have the advantage of high (>70%) yields of SWNTs along with drawbacks such as (1) relying on evaporation of carbon atoms from solid targets at temperatures >3000 °C, and (2) the nanotubes are tangled which makes difficult the purification and application of the samples.

The laser-ablation prepared samples usually contain >70% nearly endless, highly tangled ropes of SWNTs along with nanoscale impurities. The potential use of the nanotubes in nano electronics devices requires nanotubes with lengths in the range of 10–300 nm. A procedure of purification of the as-grown sample before cutting the nanotube was proposed by Liu et al [134]. The purification method consists in refluxing in 2.6 M nitric acid and re-suspending the nanotubes in pH 10 water with surfactant followed by filtration with a cross-flow filtration system. Passing the resultant purified SWNT suspension through a polytetrafluoroethylene filter produced a freestanding mat of tangled SWNT ropes-a ''bucky paper''.

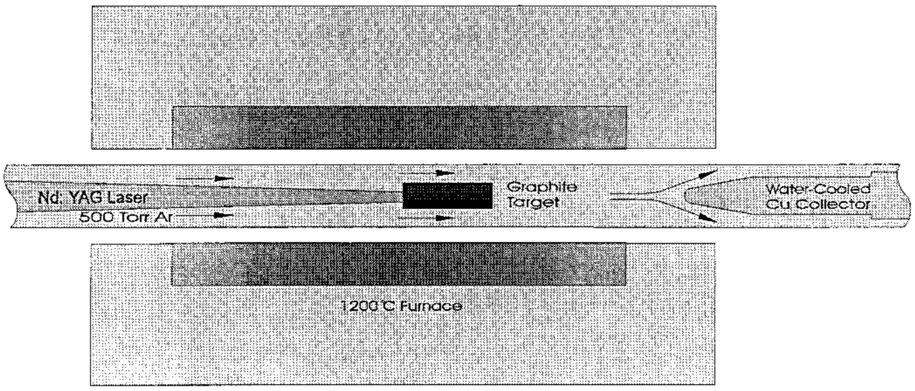

Figure. 2.16: Schematic illustration of the Smalley group's oven laser vaporization apparatus for the synthesis of multiwalled nanotubes and nanoparticles [135].

II.A.3.4 High-pressure carbon monoxide synthesis (HiPco)

Gas-phase high pressure carbon monoxide (HiPco) is an innovative process developed by Rice University in 2001[136,137] for the production of SWCNTs in large quantities up to a kilogram. In recent years, it has become a source of high-quality, narrow-diameter distribution SWCNTs claimed to be up to 97% atomic purity. A report of a large-scale yielding rate of ~10.8 g/day or ~450 mg/h [137]. Figure 2.17 shows the schematic setup of the HiPco process, whereby SWCNTs are synthesized in high pressure (30–50 atm), high temperature (900–1100 °C) flowing CO on clusters of iron catalysts formed in situ from iron pentacarbonyl, $Fe(CO)_5$. fraction of the CO flow is passed through a liquid-filled $Fe(CO)_5$ bubbler and carried the $CO/Fe(CO)_5$ mixture into the hot reaction zone. These iron clusters act as nucleating and growing sites of SWCNTs. The production of SWCNTs in the gas phase is carried out by CO disproportionation (Boudouard reaction):

$$CO + CO \rightarrow C(SWCNTs) + CO_2$$

The as-synthesized HiPco products consist of SWCNT ropes interspersed with carbon-over coated metal particles (2–5 nm), and the sidewalls of SWCNTs are free of amorphous carbon coating. The size and diameter distribution of SWCNTs are controllable by the CO pressure. EDX spectroscopy shows that the HiPco product typically consists of 97 mol % of carbon and 3 mol % of iron. Because organometallics are used to nucleate the SWNTs produced, there will always be some nonzero density of metal particles in raw HiPco SWNT material, although increased efficiency in SWNT nucleation and/or growth can, in principle, make this concentration arbitrarily small, a yield of ~70% can be achievable.

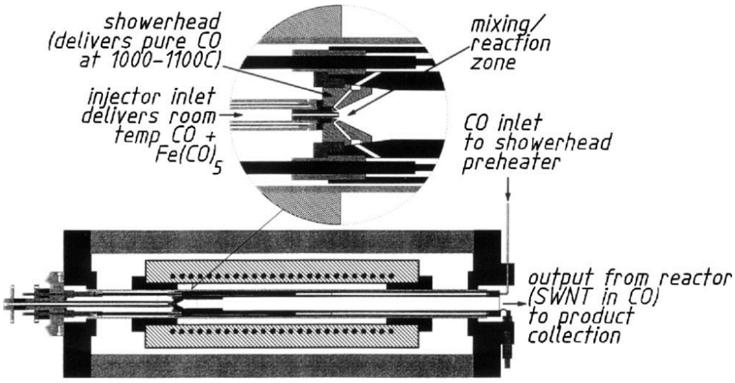

Figure. 2.17: Schematic of a HiPco furnace reactor, with the mixing/reaction zone shown enlarged. The CO gas + catalyst precursor is injected cold into the hot zone of the furnace, while excess CO gas is “showerhead” on it from all sides. Empirically this leads to the highest yield and longest individual nanotubes formed by this process [137].

II.A.3.5 CoMoCats process

Resasco et al [138]. developed a scalable process (CoMoCAT) for the production of SWCNTs by catalytic disproportionation of CO on Co/Mo/SiO_2 solid catalysts. In the CoMoCAT process, high-quality SWCNTs with a narrow distribution of tubular diameters are synthesized by CO disproportionation at 750–950 °C in the flow of pure CO at a pressure of 1–10 atm using fluidized-bed reactors. The production rate is ~0.25 g SWCNT/g catalyst in a couple of hours, with better than 80% selectivity towards SWCNT synthesis. The CoMoCAT process uses a low Co:Mo loading on silica supports (SiO_2 support with 6 nm average pore size and BET surface area of 480 m^2/g) as efficient catalysts for SWCNT production. The total loading of bimetallic Co-Mo in the catalyst is 2 wt.% with a Co:Mo molar ratio of 1:3. The synergistic effect between Co and Mo enhances the performance of catalysts [139]. The Co interacts with Mo to form a superficial Co molybdate-like species and Mo is in the form of Mo (6+) oxidation state.

During high-temperature reduction in hydrogen, the Co molybdate-like species remains as well dispersed Co^{2+} ion and resists sintering. The prevention of Co sintering is crucial to the selective synthesis of narrow diameter distribution of SWCNTs. As shown in Figure 2.18, SWCNTs synthesized by the CoMoCAT process has significantly narrower radial breathing modes (RBMs) than SWCNTs synthesized by the HiPco process. However, as the synthesis temperatures are higher than 750 °C the diameter distribution of the as-synthesized SWCNTs becomes wider, which is due to the metal sintering and formation of large catalyst clusters. Figure 2.18 compares the near-infrared emission spectra of semiconducting SWCNTs synthesized by CoMoCAT and HiPco methods. Individually suspended SWCNTs show characteristic near-infrared emission that uniquely labelled the diameter and chirality of the nanotube using (n, m) notations. The CoMoCAT SWCNT samples are dominated by two structures, namely, (6,5) and (7,5), which account for 57% of the semiconducting nanotubes. In other words, the (6,5) and (7,5) semiconducting SWCNTs constitute ~38% of the total SWCNTs in the CoMoCAT. On the other hand, the near-infrared emission of HiPco SWCNT samples exhibits several types of semiconducting SWCNTs. The CoMoCAT process has great potential in obtaining SWCNT samples with better uniformity of electronic properties. Thus, the CoMoCAT process has the potential to selectively grow SWCNT samples enriched with semiconducting (6, 5) and (7, 5) nanotubes.

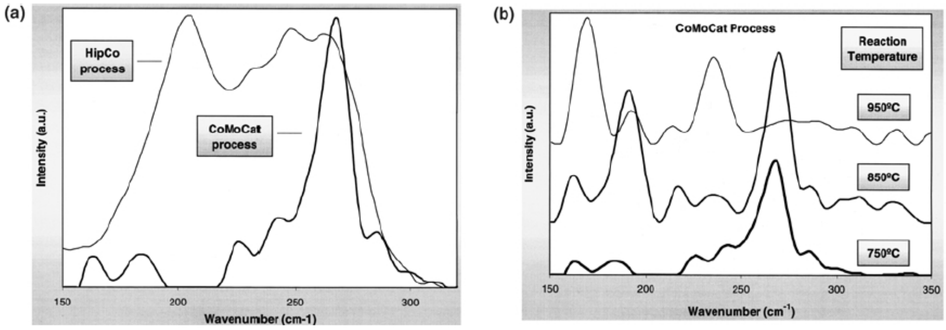

Figure. 2.18: Comparison of Raman spectra obtained with an excitation laser of 532 nm. (a) SWNT is produced by the CoMoCAT process at 750 °C (heavier line) and SWNT is produced by the HiPco process (lighter line). (b) Comparison of spectra of SWNT produced by the CoMoCAT process at various reaction temperatures. Upper 950 °C, Middle 850 °C, Lower 750 °C [138].

II.A.4 The catalysts involved in the process

A wide variety of catalytic species can be used to produce SWCNTs in CVD growth. It is important at this point to note that the word *catalyst* is used somewhat indiscriminately in nanotube science, whether or not the “catalyst” actually remains in its original form after making a nanotube. Several catalytic species, such as Fe and Co, in many cases, form metal carbides when they produce nanotubes and remain carbides after growth. Regardless of feedstock, it has been found that Fe, Co, and Ni nanoparticles are all able to form SWCNTs. The use of bimetallic or tri-metallic mixtures of Fe, Co, and Ni with elements such as Y, Mo, Ru, and Pt has led to massive increases in yield under certain conditions [139,140]. These results are empirical, and there is little generally accepted theory for why this is, though there are hundreds of experimental and theoretical papers that analyse the effects on the yield of differing concentrations of elements using a particular growth condition. Specific catalyst mixtures, such as Fe/Mo and Co/Mo [141–144] have been analysed in-depth, though usually with only one feedstock gas.

Interestingly, work by Mizuno et al. shows that while a typical Co/Mo-based catalyst is highly active in ethanol growth while having relatively low SWCNT yield in CH_4 growth, a common Fe/Mo catalyst has a high yield in CH_4 growth and low yield in ethanol [145]. This observation is one of many that make it clear that the catalyst-growth dynamics-feedstock picture is not yet complete, and there is much more to learn. Regardless of the catalyst metals chosen for growth, catalyst material can take any of three basic forms, depending on the type of samples desired: unsupported, supported, and vapour phase.

II.A.5 Carbon feedstock

The first SWCNT synthesis performed with CVD utilized carbon monoxide (CO) as a feedstock [146]. Since then, methane [147,148], ethylene [149], acetylene [150], ethanol, methanol [151], and benzene [152], as well as others, have been used successfully to make SWCNT at various temperatures and using several catalysts (usually transition metals such as Ni, Fe, Co, etc.) in a temperature range between 300–1200 °C. Since much of the growth dynamics is not well understood, no feedstock provides a clear advantage over others, though there are many particular applications in which one or feedstock excel. One of the obvious variations in feedstock choice is reactivity. For instance, CH_4 is much less reactive than ethylene (C_2H_4) or acetylene (C_2H_2). As a result, SWCNTs have been grown from C_2H_4 at temperatures as low as 550 °C [153], whereas CH_4 synthesis is not reported below 680 °C [154]. Additionally, the oxygen content of the feedstock may affect growth quality and yield. Many growth methods, such as HiPco [139] and CoMoCAT [145], utilize CO as a feedstock to much success, yielding high-quality SWCNTs that are smaller in diameter (0.7 to 1.5 nm) than those from most other conventional hydrocarbon methods (1 to 5 nm). As mentioned earlier, the presence of a controlled amount of oxygen, OH, or H_2O may have a cleansing effect by preventing the formation of amorphous carbon (which is more reactive than its graphitic cousin, and thus more sensitive to small amounts of oxidizers). To this end, ethanol (C_2H_5OH) has proven to be a highly useful feedstock, yielding the longest single tubes ever observed [155], as well as many high-yield growths, revealing yields of close to one SWCNT per catalyst particle (previously, in most synthesis, not all catalyst nanoparticles successfully produced tubes, often lower than 10%). Virtually all growth methods dilute the active carbon species in argon, hydrogen, nitrogen, helium, or some mixture of these four, which provides yet another degree of freedom. Recently, the use of C_2H_4 mixed with a small and measured amount of H_2O has been successfully utilized for highly efficient and clean growths [156]. The use of etching gases, such as H_2O, OH, or O_2, to improve growth properties is still in its infancy and is doubtless to be the next major step toward cheap and reliable production of SWCNTs.

II.A.6 Purification of Carbon nanotubes

Due to the nature of synthesising techniques and the carbonaceous source with the catalyses used, the presence of impurities as a by-product is absolute. To produce high purity CNTs, it is a necessity to go through the aspect of purification and the complexity that comes with it.

As synthesised CNTs prepared by the previously-mentioned methods inevitably contain carbonaceous impurities and metal catalyst particles, and the amount of impurities commonly increases with the decrease of CNT diameter. Carbonaceous impurities typically include amorphous carbon, fullerenes, and carbon nanoparticles (CNPs) (as shown in Figure. 2.19). Because the carbon source in arc discharge and laser ablation comes from the vaporization of graphite rods, some un-vaporized graphitic particles that have fallen from the graphite rods often exist as an impurity in the final product. In addition, graphitic polyhedrons with enclosed metal particles also coexist with CNTs synthesized by arc discharge and laser ablation as well as high temperature (>1000 °C) CVD. Fullerenes can be easily removed owing to their solubility in certain organic solvents.

Amorphous carbon is also relatively easy to eliminate because of its high density of defects, which allow it to be oxidized under gentle conditions. The knottiest problem is how to remove polyhedral carbons and graphitic particles that have a similar oxidation rate to CNTs, especially SWCNTs. Metal impurities are usually residues from the transition metal catalysts. These metal particles are sometimes encapsulated by carbon layers (varying from disordered carbon layers to graphitic shells, as shown in Figure. 2.19 b and c) making them impervious and unable to dissolve in acids. Another problem that needs to be overcome is that carbonaceous and metal impurities have very wide particle size distributions and different amounts of defects or curvature depending on synthesis conditions, which makes it rather difficult to develop a unified purification method to obtain reproducibly high-purity CNT materials. To fulfil the vast potential applications and to investigate the fundamental physical and chemical properties of CNTs, highly efficient purification of the as-prepared CNTs is, therefore, very important.

Thus, great attention has been paid to the issue of purification. The developed purification schemes usually take advantage of differences in the aspect ratio and oxidation rate between CNTs and carbonaceous impurities. In most cases, CNT purifications involve one or more of the following steps: gas phase oxidation, wet chemical oxidation/ treatment, centrifugation, filtration, and chromatography, etc. However, a reproducible and reliable purification protocol with high selectivity, especially for SWCNTs, is still a great challenge, because the purity of CNTs depends on not only purification itself, but also many other factors, including CNT type (SWCNTs or MWCNTs), morphology and structure (defects, whether or not they exist in bundles, diameter), impurity type and their morphology (particle size, defect, curvature, the number and crystallinity of carbon layers wrapping metal particles), purity assessment technique, and so on.

Since SWCNT is easily oxidised compared with MWCNT [157], the purification process such as the burning method cannot be applied to that purpose. Tohji et al., however, have succeeded in this by employing the water-heating treatment [158], furthermore, the centrifuge [159] and micro-filtration [159,160] methods can also be employed. It has recently been reported that SWCNT could be purified by the size-exclusion chromatography method, which made separation according to its length possible. This method looks effective to obtain SWCNT of a high degree of purity. The development of the differentiation method of SWCNT with its diameter is still an open problem.

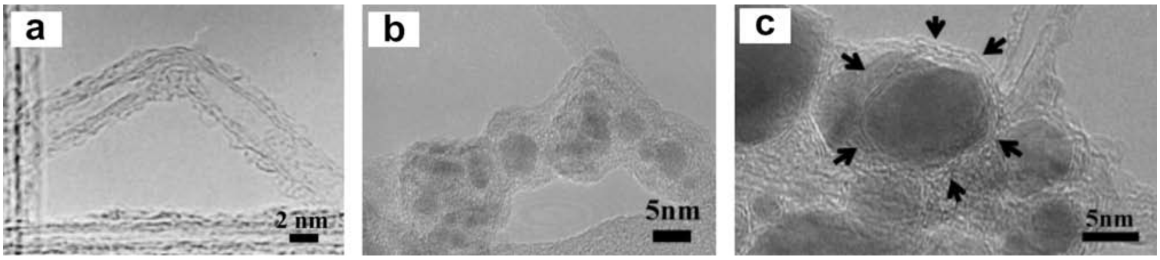

Figure. 2.19: TEM images of (a) amorphous carbon and fullerene molecules on the surface of CNTs [161]; (b) metal nanoparticles covered by amorphous carbon layer, (c) metal nanoparticles covered by graphitic carbon multi-layer ([162], ©2004 American Chemical Society).

II.A.7 Purification methods

Purification methods of CNTs can be classified into three categories, namely chemical, physical, and a combination of both. The chemical method of purifying CNTs is based on the idea of selective oxidation, wherein carbonaceous impurities are oxidized at a faster rate than CNTs, and the dissolution of metallic impurities by acids. This method can effectively remove amorphous carbon and metal particles except for those encaged in polyhedral graphitic particles. However, the chemical method always influences the structure of CNTs due to the oxidation involved. The physical method separates CNTs from impurities based on the differences in their physical size, aspect ratio, gravity, and magnetic properties, etc. In general, the physical method is used to remove graphitic sheets, carbon nanospheres (CNSs), aggregates or separate CNTs with different diameter/length ratios. In principle, this method does not require oxidation and therefore prevents CNTs from severe damage. However, the physical method is always complicated, time-consuming and less effective. The third method of purification combines the merits of physical and chemical purification, it can lead to high yield and high-quality CNT products. Owing to the diversity of the as-prepared CNT samples, such as CNT type, CNT morphology and structure, as well as impurity type and morphology, it needs a skilful combination of different purification techniques to obtain CNTs with desired purity.

II.A.7.1 Chemical oxidation

Carbonaceous impurities as a residue of synthesising CNTs are amorphous carbon and carbon nanoparticles (CNPs). These impurities compared to CNTs usually have higher oxidation activity, as for amorphous carbon is due to the presence of more unsaturated bonds and structural defects which tend to be easily oxidized; meanwhile, the high reactivity of the CNPs can be attributed to their large curvature and pentagonal carbon rings [163,164]. Therefore, chemical oxidation purification is based on the idea of selective oxidation etching, wherein carbonaceous impurities are oxidized at a faster rate than CNTs. The disadvantages of this method are that it often opens the end of CNTs, cuts CNTs, damages the surface structure and introduce oxygenated functional groups (–OH, –C=O, and –COOH) on CNTs. As a result, the purified CNTs in turn can serve as chemical reactors or a starting point for subsequent nanotube surface chemistry [165,166].

A.7.1.1 Gas phase oxidation

In this oxidative purification process, the carbonaceous impurities oxidized at a temperature ranging from 225 °C to 760 °C within an oxidizing atmosphere. Commonly used ones, includes air [167,168], a mixture of Cl_2, H_2O, and HCl [169], a mixture of Ar, O_2, and H_2O [170], a mixture of O_2, SF_6 and $C_2H_2F_4$ [171], H_2S and O_2 [172], and steam [173]. Selective, applying similar procedure of MWCNTs onto SWCNTs has its inconvenient, specific targeted impurities, a low yield but less damage to tube walls overall.

Gas phase oxidation is a simple method for removing carbonaceous impurities and opening the caps of CNTs without vigorously introducing sidewall defects, although it cannot directly get rid of metal catalysts and large graphite particles.

A.7.1.2 Liquid phase oxidation

Oxidative ions and acid ions dissolved in the solution can evenly attack the network of raw samples, and therefore a selection of oxidant type and precise control of treatment conditions can produce high-purity CNTs in a high yield. The commonly used oxidants for liquid-phase oxidation include HNO_3 [174], H_2O_2 or a mixture of H_2O_2 and HCl [175–177], a mixture of H_2SO_4, HNO_3, $KMnO_4$ and NaOH [178–182].

Nitric acid is the most commonly used reagent for SWCNT purification for its mild oxidation ability, which can selectively remove amorphous carbon. In addition, it is inexpensive and non-toxic, capable of removing metal catalysts and no secondary impurities are introduced.

Liquid phase oxidation is a continuous process that can eliminate impurities on a large scale, but it often causes reaction products on the CNTs sidewalls, adding functional groups, which increases the chemical activity and the solubility of CNTs in most organic and aqueous solvents. This surface modification effect shows great potential for improving their physical and chemical properties for specific applications (see) [183–186]. and destroys CNT structures (including cutting and opening CNTs). The main problem of this liquid oxidation strategy is the damage to CNTs, the inability to remove large graphite particles, and the loss of a large number of SWCNTs with a small diameter. It is very difficult to obtain purified SWCNTs with high purity and high yield without damage.

A.7.1.3 Electrochemical oxidation

Superior to the gas phase oxidation and wet oxidation, the optimum time and degree of electrochemical oxidation for CNT purification can be easily determined. This method can get rid of impurities to some extent, particularly for selectively opening and purifying vertically aligned CNT arrays. The desired vertical orientation can be maintained and facilitates the use of CNT arrays as fuel cell electrodes, sensor platforms, nanoreactors, field emitter components, and other applications. However, little polyhedral carbon, graphite particles, and metal particles enwrapped by carbon layers with fewer defects can be removed by CV oxidation. Moreover, the purity of the obtained sample greatly depends on the starting materials, and the amount of sample purified for each batch is too small to make the method practical [187].

II.A.7.2 Physical-based purification

The morphology and physical properties of CNTs, such as aspect ratio, physical size, solubility, gravity, and magnetism are different from impurities. These differences enable the separation of CNTs from impurities by applying specified physical techniques. Therefore, physical-based methods including filtration, chromatography, centrifugation, electrophoresis, and high temperature annealing (1400–2800 °C), have been extensively investigated. The most striking feature of these methods is a non-destructive and non-oxidizing treatment. Another feature is that the purifications are mostly performed in solution, which requires the as-prepared samples to have good dispersibility in the solutions. To meet this requirement, surfactants and/or sonication are often used.

II.A.7.2.1 Filtration

Separation by filtration is based on the differences in physical size, aspect ratio, and solubility of SWCNTs, CNSs, metal particles and polyaromatic carbons or fullerenes. Small size particles or soluble objects in the solution and can be filtered out, while SWCNTs with a large aspect ratio will remain. Polyaromatic carbons or fullerenes are soluble in some organic solvents, such as CS_2, toluene, etc. The impurities can be easily removed by immersing the as-prepared sample in these organic solutions followed by filtering. The impurity particles smaller than that of the filter holes flow out with the solution during filtration, while large impurity particles and small ones adhering to the CNT walls remain. One problem with this technique is that CNTs or large particles deposited on the filter often block the filter, making the filtering prohibitively slow and inefficient. Therefore, a stable suspension of CNTs and a technique preventing them from deposition and aggregation are very important during filtration. Thus, surfactants are widely used to make a stable CNT suspension, and ultrasonication is usually adopted to prevent the filter from being blocked.

A major advantage of filtration is that it is driven by pure physicochemical interactions of carbon products with amphiphilic molecules and the filter membrane, leaving the nanotubes undamaged. However, this procedure relies on the quality of raw samples and is time-consuming. In addition, amorphous and spherical carbon particles stuck on the tube walls cannot be effectively removed.

II.A.7.2.2 Centrifugation

Based on the effect of gravity on particles (including macromolecules) in suspension because two particles of different masses settle in a tube at different rates under the effect of gravity. On the other hand, centrifugation can also separate amorphous carbon and CNPs based on the different stabilities in dispersions consisting of amorphous carbon, SWCNTs, and CNPs in aqueous media. The different stabilities resulted from the different (negative) surface charges introduced by acid treatment [187–189], such as nitric acid which introduces functional groups on their surface.

II.A.7.2.3 Solubilisation of CNTs with functional groups

The principle of this purification step is to solubilize CNTs by introducing functional groups onto their surface. These soluble nanotubes allow for the application of other techniques such as filtration or chromatography as a means of tube purification. To regain reasonable quantities of un-functionalized but purified nanotubes, the functional groups should be removed by thermal treatment or other techniques. The advantage of this process is that it can always preserve the surface electronic structure of CNTs. This property is of fundamental importance for the use of nanotubes as biosensors [190]. On the other hand, the capability of dispersing CNTs in solution is a very important step for using CNTs as vectors to deliver therapeutics (drug, nucleic acid) [190]. However, the effectiveness of this technique is not high for CNT samples containing a large number of impurities or bundled SWCNTs.

II.A.7.2.4 High temperature annealing

For some applications of CNTs, such as their use as biomaterials, complete removal of metal particles is of particular importance. However, it is very difficult to achieve this by acid washing because most of the metal particles are enwrapped by carbon layers. The physical properties of carbon and metals are different at high temperatures (>1400 °C) under an inert atmosphere or high vacuum. It is well known that graphite is stable even at 3000 °C, while metal evaporates at temperatures higher than their evaporation point. Therefore, it is expected that high temperature annealing can effectively remove metal particles.

High temperature annealing of CNTs is one of the most efficient methods for the removal of metal particles at the tips or in the hollow core of CNTs [191–194] and also for structural evolvement from disordered to straight, crystalline layers [195]. High temperature annealing not only increases the mechanical strength and thermal stability of CNTs but also affects their electronic transport property. The drawback of this method is the carbonaceous impurities remained and become more difficult to remove after graphitisation, Therefore, this method can be used to remove residual metal particles of purified CNTs obtained by other techniques for achieving metal free CNTs. For more on the subject of carbon nanotubes purification see [196].

II.B.1 Introduction to metal matrix nanocomposites

Nanocrystalline materials are single-phase or multi-phase materials, the crystal size of which is of the order of a few (typically 1–100) nanometres in at least one dimension. Because of the extremely small size of the grains, a large fraction of the atoms in these materials are located in the grain boundaries (Figure. 2.20) and thus, the material exhibits enhanced combinations of physical, mechanical, and magnetic properties (compared to material with more conventional grain size, i.e., >1 µm). Nanocrystalline materials show increased strength, high hardness, extremely high diffusion rates, and consequently reduced sintering times for powder compaction. Several excellent reviews are available giving details of the processing, properties, and applications of these materials [197–200].

Grain sizes with nanometre dimensions have been observed in almost all mechanically alloyed pure metals, intermetallic, and alloys (if they continue to be crystalline). Thus, it appears to be a ubiquitous phenomenon. Despite this, there have not been many investigations to explain why and how nanometre-sized grains are obtained in these materials. Hellstern et al. [201] have described the mechanism of the formation of nanostructures by MA/MM. From high-resolution TEM observations, these authors reported that at the early stages of MA, shear bands were observed due to the high deformation rates experienced during MA. These shear bands, which contain a high dislocation density, have a typical width of approximately 0.5–1.0 µm. With continued milling, the average atomic level strain increases due to the increasing dislocation density, and at a certain dislocation density within these heavily strained regions, the crystal disintegrates into subgrains that are separated by low-angle grain boundaries. This results in a decrease in the lattice strain. On further processing, deformation occurs in shear bands located in previously unstrained parts of the material. The grain size decreases steadily and the shear bands coalesce. The small angle boundaries are replaced by higher angle grain boundaries, implying grain rotation, as reflected by the absence of texture in the electron diffraction patterns and random orientation of the grains observed from the lattice fringes in the high-resolution electron micrographs. Consequently, dislocation-free nanocrystalline grains are formed.

The minimum grain size achievable by milling is determined by the competition between the plastic deformation via dislocation motion and the recovery and recrystallization behaviour of the material [202,203].

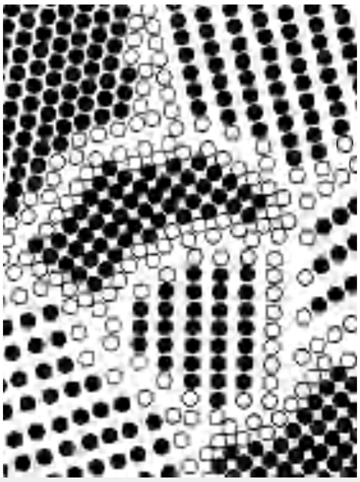

Figure. 2.20: Schematic arrangement of atoms in an equiaxed nanocrystalline metal.

Materials with high specific strength and stiffness have seen a surge in demand for various applications that thrive on high strength, lightweight, wear resistance, high electrical conductivity, and better properties at elevated temperatures compared to monolithic metals and alloys.

The incorporation of a different element(s) to a hosting matrix of a single (or multiple) constituents, to reach a desire mechanical and thermal properties has been pushed to the front of research and development. Humans have been through history experimenting with metals, ceramics, and no polymers

Metal matrix nanocomposites (MMCs) have many advantages over conventional metals, including a higher specific modulus, higher specific strength, better properties at elevated temperatures, lower coefficients of thermal expansion and better wear resistance. The following properties were enhanced due to the use of nano-scale reinforcement:

- Tensile and compressive behaviour
- Ductility or elongation to failure, a must then breaks design philosophy.
- High-temperature mechanical properties
- Creep
- Dynamic mechanical properties
- Wear resistance, including scratch resistance
- Coefficient of thermal expansion
- Damping
- Machining
- Ignition resistance
- Dry/ wet corrosion resistance

II.B.2 Metal-carbon nanotubes nanocomposite system

One of the technical hurdles associated with CNTs is post-synthesis, i.e., dispersion of CNTs in the matrix. Dispersion of the tubes is particularly important. Failure to disperse produces a phase separation due to the strong surface interactions between the tubes. It is likely that chemical functionalization would not only serve to facilitate dispersion but could also stabilize the CNTs and prevent agglomeration.

Although CNTs have exceptional chemical and physical properties, incorporating them into other materials has been inhibited by the chemical nature of their sidewalls. In many applications, it is necessary to tailor the chemical nature of the nanotubes to take advantage of their unique properties. In the area of material chemistry, for example, problems such as phase separation, aggregation, poor dispersion within a matrix, and poor adhesion to the host must be solved (Figure 2.21). These problems can be addressed by developing a new multifunctional surface treatment technology that optimizes the interaction between CNTs and the host matrix.

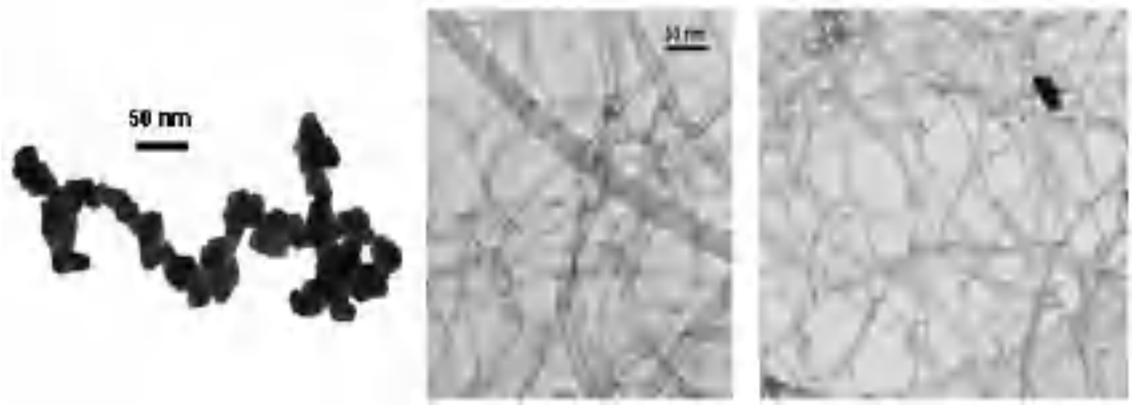

Figure 2.21: Agglomeration of carbon nanomaterials is a problem: carbon black, MWCNTs, and SWCNTs (© Zyvex 2006).

Due to strong attractive interactions, and van der Waal interactions, almost all the carbon nanomaterials form aggregate, and without any exception, SWCNTs tend to aggregate to form ropes or bundles and further agglomerate when dispersed in a polymer matrix, thus preventing the efficient transfer of their superior properties to the matrix. The high surface area of the nanotubes also results in high viscosity of the nanotubes/polymer mixture that making it extremely difficult to form uniform dispersion.

The practical results show that the dispersion process of CNTs inside the metallic matrices can be completely different and more difficult than water media. This is because an intrinsically different phase (i.e., metal) is added to the system which makes the process more complex. Among these complexities, the CNT/metal interfaces and the poor wettability of CNTs by metal matrices are of prime significance. significance. As generally accepted, an increment in CNT content can result in further agglomeration due to the increased possibility of contacts between CNTs and decreased wettability.

Therefore, dispersing individual CNTs in metallic systems with reasonable spacing is a critical challenge for engineers. Here when the mechanical alloying comes to solve this problem through powder metallurgy which proves to be a reliable technique to mix metals such iron and copper and bypass the solubility issue, as well as a homogeneous dispersion of additives such as carbon nanotubes into the hosting medium.

A great deal of attention has been dedicated to the incorporation of CNTs into metal matrix-based nanocomposites, such Al, Ni, Cu, Ti, Mg; yet. on the other hand, there aren’t many studies oriented toward the Fe-Cu based nanocomposite with the addition of CNTs.

II.B.3 Challenges facing metal matrix nanocomposites reinforced CNTs

Non-uniform dispersion of CNTs in the metallic matrix, poor interfacial adhesion at the CNT/metal interface, the unfavourable chemical reaction of CNTs with the matrix, and low compatibility are the most significant challenges

(i) Favourable dispersion of CNTs throughout the matrix. A composite with improved properties will be obtained when the reinforcements are uniformly distributed through the matrix. Otherwise, the micro-pores, as well as agglomerated particles, may for all over the microstructure [204,205]. To overcome this challenge, a broad spectrum of dispersion methods is developed. Among these techniques, the mechanical methods [206], surface treatments [207], and chemical methods [208] are the most conventional. Each of these techniques has its advantages and disadvantages.

(ii) The unfavourable chemical reaction of CNTs with matrix at high pressures, elevated temperature, and induced strains. It is usually accompanied by the formation of defects. In the other words, to thermally decompose CNTs in exposure to the metallic matrix, the presence or formation of defects is required. It is shown that the thermal decomposition of CNTs can bilaterally affect the final properties of the nanocomposites. In other words, the final properties strongly depend on the chemical composition of the formed intermetallic [209,210].

(iii) The poor interfacial adhesion between CNTs and the matrix is due to the hydrophobic nature of the CNTs. This shortcoming deteriorates the load bearing between the matrix and CNTs. Moreover, intensive phonon scattering arising from insufficient adhesion can significantly enhance the electrical resistivity [211]. It is noteworthy that the interfacial adhesion can be improved whenever a controlled superficial chemical reaction between CNTs and metallic matrix occurs. In other words, the poor interfacial adhesion can be considered as a sub-challenge under the title of "chemical reaction of CNTs with metallic matrix".

(iv) Low compactability of metallic powders. The incorporation of CNTs into metallic powders can decline the relative density of final CNT-metal compacts if the agglomeration of CNTs is heavy and their volume fraction is exceedingly high.

II.B.4 Mechanical alloying (MA)

Two different terms are commonly used in the literature to denote the processing of powder particles in high-energy ball mills. Mechanical Alloying (MA) describes the process when mixtures of powders (of different metals or alloys/compounds and non-miscible materials) are milled together. The material transfer is involved in this process to obtain a homogeneous alloy. On the other hand, milling of uniforms (often stoichiometric) composition powders, such as pure metals, intermetallic, or pre-alloyed powders, where a material transfer is not required for homogenization, has been termed Mechanical Milling (MM) and in some cases as Mechanical Grinding. The use of this process to mix pure elements can achieve the formation of amorphous phases also intermetallic systems.

Mechanical alloying basically, is a powder metallurgy technique consisting of repeated cold welding, fracturing and re-welding of powder particles in a high-energy ball mill. This technique is of fundamental importance since it allows achieving a better dispersion of nano-powder into the composite by breaking up matrix clusters

II. B.5 Types of mills

Different types of high-energy milling equipment are used to produce mechanically alloyed powders. They differ in their capacity, the efficiency of milling and additional arrangements for cooling, heating, etc. A detailed description of the different mills available for MA can be found in [212].

II.B.5.1 SPEX shaker mills

Shaker mills such as SPEX mills (Figure. 2.22a), which mill about 10–20 g of the powder at a time, are most commonly used for laboratory investigations and alloy screening purposes.

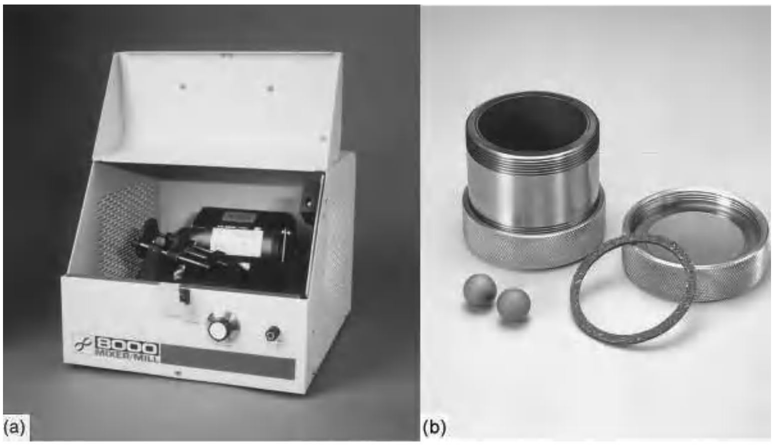

Figure. 2.22: (a) SPEX 8000 mixer/mill in the assembled condition. (b) Tungsten carbide vial set consisting of the vial, lid, gasket, and balls. Courtesy of SPEX CertiPrep, Metuchen, NJ.

II.B.5.2 Planetary ball mills

Another popular mill for conducting MA experiments is the planetary ball mill in which a few hundred grams of the powder can be milled at a time (Figure. 2.23a)

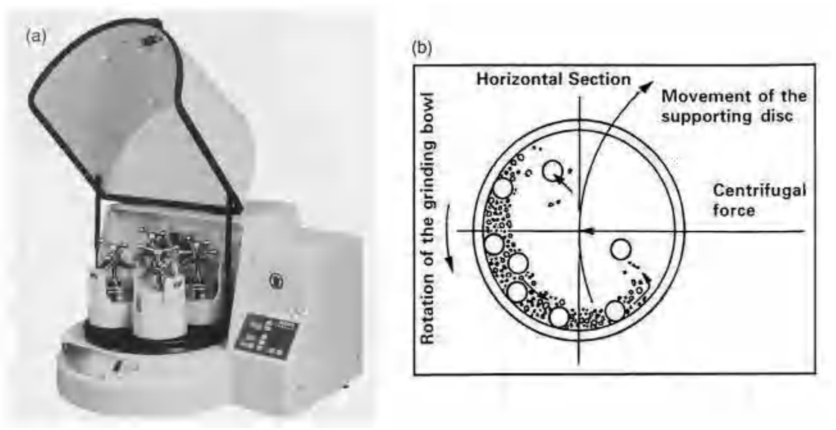

Figure. 2.23: (a) Fritsch Pulverisette P-5 four station ball mill. (b) Schematic depicting the ball motion inside the ball mill. Courtesy of Gilson Company, Inc., Worthington, OH.

II.B.5.3 Attritor mills

An attritor (a ball mill capable of generating higher energies) consists of a vertical drum with a series of impellers inside it. Set progressively at right angles to each other, the impellers energize the ball charge, causing powder size reduction because of impact between balls, between balls and container wall, and between balls, agitator shaft, and impellers.

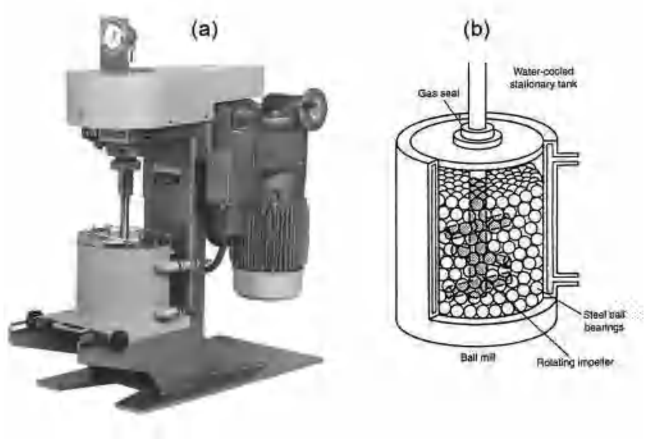

Figure. 2. 24: (a) Model 1-S attritor. (b) Arrangement of rotating arms on a shaft in the attrition ball mill. Courtesy of Union Process, Akron, OH

II.B.5.4 Commercial mills

Commercial mills for MA are much larger than the mills described above and can process up to 1250 kg capacity at a time. (Figure. 2.25).

The milling time decreases with an increase in the energy of the mill. It may be noted that the times are an order of magnitude shorter in the attritor [213].

Figure. 2.25: Commercial production-size ball mills used for mechanical alloying. Courtesy of Inco Alloys International.

II.B.5.5 New designs

Include the rod mills, vibrating frame mills, the ability to control the temperature of milling from very low temperatures by spraying liquid nitrogen up to a high temperature of 300 °C by electrical heating; also, the potential to control the nature and magnitude of the impact of the balls using a field strength with the help of adjustable magnets.

II.B.6 Process variables

Mechanical alloying is a complex process and hence involves the optimization of several variables to achieve the desired product phase and/or microstructure.

- type of mill,
- milling container,

- milling speed,
- milling time,
- type, size, and size distribution of the grinding medium,
- ball-to-powder weight ratio,
- the extent of filling the vial,
- milling atmosphere,
- process control agent, and
- milling temperature.

Our case of study is concerned with the two most important parameters:

- milling time of 20-, 60-, and 120-minutes time,
- and the carbon nanotubes concentration of 0, 0.5, 1, and 2 vol.% added to the iron-copper matrix.

II.B.7 Mechanism of alloying

During high-energy milling, the powder particles are repeatedly fattened, cold welded, fractured and rewelded. Whenever two steel balls collide, some amount of powder is trapped in between them. The force of the impact plastically deforms the powder particles leading to work hardening and fracture. The new surfaces are created to enable the particles to weld together and this leads to an increase in particle size. Since in the early stages of milling, the particles are soft (if we are using either ductile-ductile or ductile-brittle material combination), their tendency to weld together and form large particles is high.

The composite particles at this stage have a characteristic layered structure consisting of various combinations of the starting constituents. With continued deformation, the particles get work hardened and fracture by a fatigue failure mechanism and/or by the fragmentation of fragile flakes. Fragments generated by this mechanism may continue to reduce in size in the absence of strong agglomerating forces. At this stage, the tendency to fracture predominates over cold welding.

However, it should be remembered that the efficiency of particle size reduction is very low, about 0.1% in a conventional ball mill. The efficiency may be somewhat higher in high-energy ball milling processes but is still less than 1%.

The remaining energy is lost mostly in the form of heat, but a small amount is also utilized in the elastic and plastic deformation of the powder particles.

After milling for a certain length of time, steady-state equilibrium is attained when a balance is achieved between the rate of welding, which tends to increase the average particle size, and the rate of fracturing, which tends to decrease the average composite particle size. Smaller particles can withstand deformation without fracturing and tend to be welded into larger pieces, with an overall tendency to drive both very fine and very large particles towards an intermediate size [214].

The minimum grain size achievable by milling is determined by the competition between the plastic deformation via dislocation motion and the recovery and recrystallization behaviour of the material [202,215]

II.B.8 Powder contamination

A major concern in the processing of metal powders by MA is the nature and the number of impurities that get into the powder and contaminate it. The small size of the powder particles, availability of large surface area, and formation of new fresh surfaces during milling all contribute to the contamination of the powder. Thus, it appears as though powder contamination is an inherent drawback of the technique unless very special precautions are taken to avoid or at least minimize it.

During the process of MA, the metal powder coats the surface of the grinding medium and the inner walls of the container. The magnitude of contamination appears to depend on the time of milling, the intensity of milling, the atmosphere in which the powder is milled, and the difference in the strength and hardness of the powder and the milling medium.

During MA the powder particles get trapped between the grinding medium undergo severe plastic deformation; Newly created surfaces due to the fracture of the powder particles. Additionally, collisions occur between the grinding medium and the vial, and also amongst the grinding balls. All these effects cause wear and tear of the grinding medium and the vial resulting in the incorporation of these impurities into the powder. The extent of contamination increases with increasing milling energy and also the use of higher BPR, higher speed of milling, etc.

Many attempts in recent years have been made to minimize powder contamination during MA. One way of minimizing the contamination from the grinding medium and the container is to use the same material for the container and grinding medium as the powder being milled. Thus, one could use copper balls and copper containers for milling copper and copper alloy powders. In this case, also there will be wear and tear of the grinding medium and this gets incorporated into the powder. Thus, even though there is no contamination, the chemistry of the final powder will be different from the starting powder; the metallic content in the final powder (from the container and balls) would be higher than in the initial powder. This can be compensated for if one knows the extent of the increase of the metallic content in the final powder [216].

III

MATERIALS AND METHODS

In this chapter, a brief on the preparation method of the samples, thereafter, a synopsis on the characterisation techniques been used, which they were essential for evaluating the properties of carbon nanotubes-reinforced iron-copper matrix nanocomposites. One of the main focuses is to have an understanding of the microstructural features such as carbon nanotubes distribution in the matrix, the interfacial reaction between CNTs and the matrix, CNTs retention and damage, and grain size changes in the matrix due to CNTs additions and milling time respectively. Thereafter, is to evaluate the thermal properties of the nanocomposite such as heat capacity and coefficient of thermal expansion. While Fourier transforms infrared spectroscopic study of the nanocomposites was done to understand the bonding characteristics. Raman spectroscopy was employed to assess the structural integrity of CNTs after high energy ball milling (HEBM).

These characterisation techniques are essential to provide insight and understanding on the correlation between thermodynamic behaviour and microstructural changes of the nanocomposites.

III.1 Samples preparation

A high-energy planetary ball mill (HEBM) is used for mechanochemical activation. Hardened stainless steel balls (15 units of 15 mm diameter) and vial (70 mm height, 50 mm diameter) with a ball-to-powder weight ratio of 20:1 was used. The vial temperature was held below 375 K during the experiments by air cooling. The milling process was cyclic with 5 min of treatment and 25 min of cooling time. The rotation speed was equal to 1480 rpm, the acceleration was around 50 g, and the pressure for a substance particle reached 5 GPa.

Multiwalled carbon nanotubes (TU U 24.1-03291669-009:2009) were synthesized through a chemical vapour deposition procedure in a rotating reactor [217]. Their resulting characteristics were: average diameter between 10 and 20 nm; specific surface area (determined through Ar-adsorption) - between 200 and 400 m^2/g; bulk density - between 20 and 40 g/dm^3 [218,219].

The charge was made of IP-1 (GOST 9849–86) iron and PMS-1 (GOST 4960–2009) copper powders in a 4:1 weight ratio. These powders were mixed with multiwalled carbon nanotubes at the concentrations of 0.5, 1.0, and 2.0 % in volume, for different milling times of 20, 60, and 120 minutes.

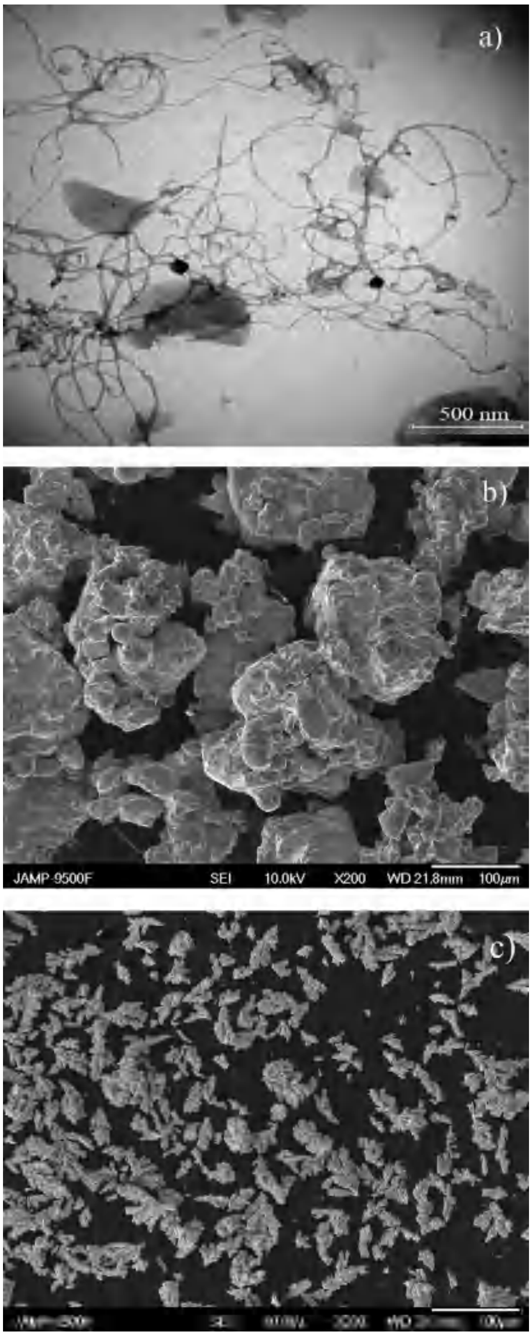

Figure. 3.1: Microstructural characterisation of source materials: (a) TEM image of CNTs. SEM image of (b) Fe, (c) Cu powders. [267]

After processing in the ball mill, the nanocomposites were subjected to a 40% compression followed by annealing at 950 °C for 30 min in Argon flow. Then, the powder samples were subjected to cold rolling followed by annealing at 900 °C in Argon flow. The described cycle was repeated three times; thus, the samples were undergone to 80% thinning. Finally, the thickness of the obtained ribbons was near 0.3 mm.

The temperature behaviour of some physical characteristics of the made nanocomposites, which were named here and before as Fe–Cu, Fe–Cu-CNT (0.5), Fe–Cu-CNT (1.0), and Fe–Cu-CNT (2.0), was studied using dilatometry and calorimetry technique. Structural characteristics and composition of the samples were monitored by X-ray diffraction, Raman scattering, and Infrared spectroscopy (IR).

The NETZSCH 402C dilatometer (NETZSCH, Selb, Germany) with 3% of accuracy were used. The heating rate was near 10 °C/min. The thermal expansion coefficient was measured in the temperature range from ambient temperature up to 800 °C.

Differential scanning calorimetry (DSC) test was performed using the Jupiter STA 449 F3 NETZSCH calorimeter (NETZSCH, Selb, Germany). The same heating rate was applied as under dilatometric measurements.

The X-ray diffraction patterns of the nanocomposite under study were obtained using the automated Philips X Pert Pro diffractometer with the filtered cobalt radiation $K_{\alpha 1}$= 1.7909 Å under the following scanning parameters: monitoring range [20–80°], with step scan 0.026°.

The Raman spectroscopy was carried out using a Raman Bruker Senterra spectrometer instrument, with a green laser (wavelength λ= 532 nm) from an argon ion.

The Infrared spectroscopy (also known as FTIR which stands for Fourier Transformation infrared), done using Jasco FT/IR-6300 spectrometer.

III.2 Characterisation Methods

The main objective is to evaluate the thermal properties and behaviour such as heat flow and weight loss or gain, as well as coefficient of thermal expansion (CTE) of the Fe–Cu-MWCNTs nanocomposite.

III.2.1 Differential scanning calorimetry (DSC)

Differential scanning calorimetry (DSC) is an analytical technique for studying thermal behaviour by measuring the rate of change in heat flow to or from a sample specimen as it is subjected to a controlled temperature program in a controlled atmosphere. A variation in the physical properties of a sample with temperature and time is measured [220]. With this technique, the amount of energy absorbed or released by a sample is measured as it is heated or cooled at a controlled rate. During a temperature change, DSC measures the heat radiated or absorbed by the sample based on the temperature difference between the sample and the reference material [221]. In simple terms, it detects and follows the changing of heat capacity C_p by temperature.

There are two types of DSC systems commonly in use:

III.2.1.1 Heat flux DSC (used)

In a heat flux DSC, a pan containing the sample and an empty reference pan is placed on a thermoelectric disk enclosed by a furnace. As the furnace is heated at a linear heating rate, the heat is transmitted to the sample and reference pan through the thermoelectric disk. The difference in temperature of the sample and reference pan due to the heat capacity (Cp) of the sample is measured by area thermocouples, and the resultant heat flow is calculated by the thermal equivalent of Ohm's law:

$$q = \frac{\Delta T}{R} \tag{3.1}$$

where q is the sample heat flow, ΔT is the temperature difference between sample and reference, and R is the resistance of the thermoelectric disk. [222]

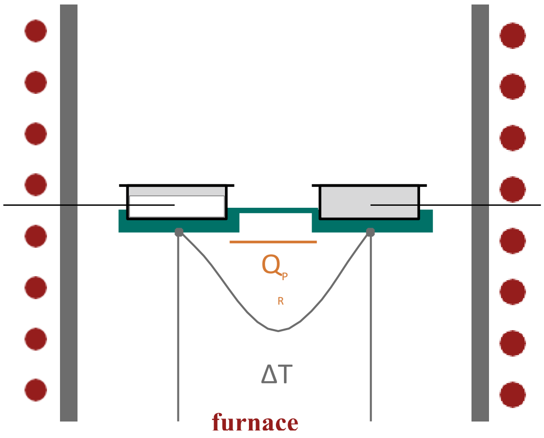

Figure 3.2: Schematic of a heat-flux DSC cell.

III.2.1.2 Power-Compensated DSC

In a PC-DSC, the sample and reference pans are placed in separate furnaces heated by separate heaters so the temperatures of the sample and reference are kept equal to each other; both temperatures are increased or decreased linearly. Two independent heating systems are used in PC-DSC; these heating units are quite small, which allows a rapid rate of heating, cooling, and equilibration. Both heating systems are placed in a large temperature-controlled heat sink. The power needed to maintain the sample temperature equal to the reference temperature as a function of the programmed temperatures is measured. The response time of PC-DSC is very rapid, so it is well suited for the kinetics studies in which fast equilibrations to new temperature settings are needed [223].

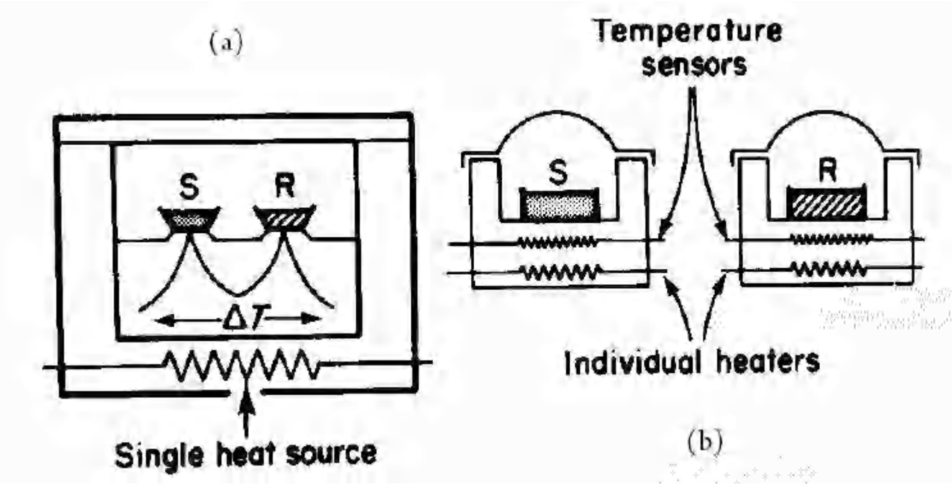

Figure. 3.3: (a) Heat flux DSC; (b) power-compensation DSC.

DSC Heat Flow

$$\frac{dH}{dt} = C_p \frac{dT}{dt} + f(T,t)$$

$\frac{dH}{dt}$	Total heat flow signal measured by the calorimeter
C_p	Sample Heat Capacity = Sample Specific Heat x Sample Weight
$\frac{dT}{dt}$	Underlying Heating Rate
$f(T,t)$	Heat flow is a function of time at an absolute temperature (kinetic response of sample)

III.2.1.3 Information obtained from DSC

- Glass Transition temperature (Tg)
- Melting points and boiling points
- Crystallization time and temperature
- Per cent crystallinity
- The heat of fusion and reaction
- Specific heat capacity
- Oxidative stability
- Rate of cure
- Degree of cure
- Reaction kinetics
- Purity
- Thermal stability

III.2.1.4 Limitations

- Very sensitive to any change in the sample or crucible.
- Requires very good thermal contact with the bottom of sample crucible
- Very sensitive to the heating rate

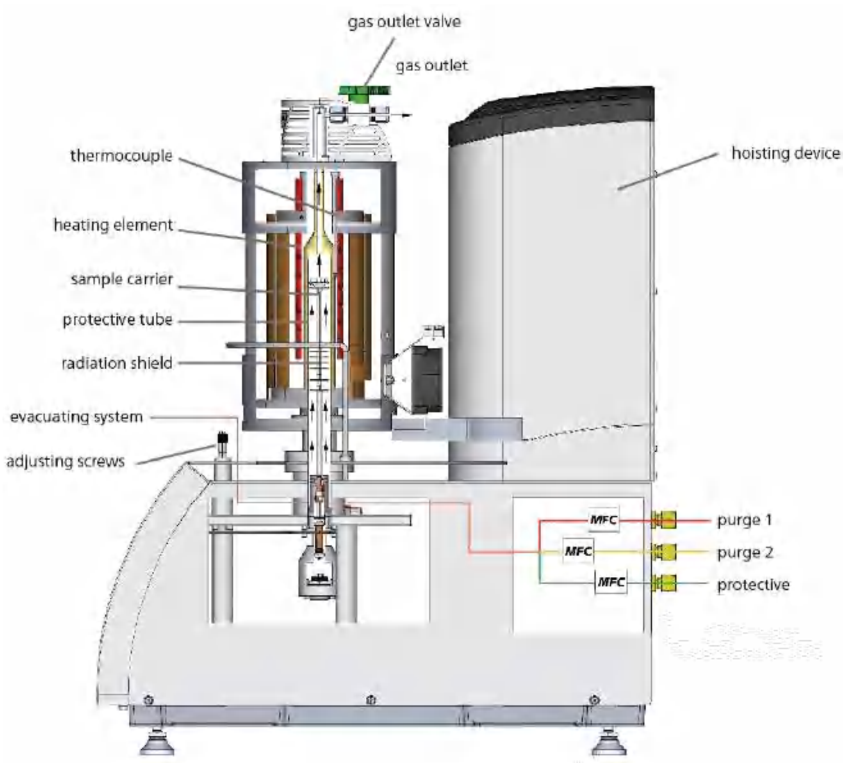

Figure 3.4: NETZSCH STA 449 F3 Jupiter Simultaneous Thermal Analyzer (STA) Incorporates TGA and DSC to measure mass change and heat flow rate simultaneously. *(Heat Flux)*

III.2.1.5 DSC Terminologies

- **Heat capacity *C*:** Heat brought to the system to increase its temperature divided by that temperature increase. At constant volume $C_V = \left(\frac{\partial U}{\partial T}\right)_V$ at constant pressure $C_P = \left(\frac{\partial U}{\partial T}\right)_P$, where U is the energy and H is the enthalpy of the system [224].
- **Amorphous Phase:** The portion of material whose molecules are randomly oriented in space. Liquids and glassy or rubbery solids. Thermosets and some thermoplastics.
- **Crystalline Phase:** The portion of material whose molecules are regularly arranged into well-defined structures consisting of repeat units. Very few polymers are 100% crystalline.
- **Semi-crystalline polymers:** Polymers whose solid phases are partially amorphous and partially crystalline. The most common thermoplastics are semi-crystalline.

- **Endothermic:** A reaction for which the overall standard enthalpy change ΔH° is positive, in another way, it is a transition that absorbs energy [225].
- **Exothermic:** A reaction for which the overall standard enthalpy change ΔH° is negative, in another way, it is a transition that releases energy [225].
- **Melting:** The endothermic transition upon heating from a crystalline solid to a liquid state. This process is also called fusion. The melt is another term for the polymer liquid phase.
- **Crystallization:** The exothermic transition upon cooling from liquid to crystalline solid. Crystallization is a function of time and temperature.
- **Cold Crystallization:** The exothermic transition upon heating from the amorphous rubbery state to the crystalline form. This only occurs in semi-crystalline polymers quenched (very rapidly cooled from the melt) into a highly amorphous state.
- **Enthalpy of Melting/Crystallization:** The heat energy required for melting or released upon crystallization. This is calculated by integrating the area of the DSC peak on a time basis.

Table 3.1: Physical origin of peaks in DSC

	Endothermic	*Exothermic*
Crystalline Transition	X	X
Fusion	X	
Crystallization		X
Vaporization	X	
Sublimation	X	
Adsorption		X
Desorption	X	
Glass Transition	Baseline change	No Peaks
Liquid Crystal Transition	X	
Physical Aging	X	

Chemisorption		X
Dehydration	X	
Decomposition	X	X
Oxidative Degradation		X
Oxidation in Gaseous Atmosphere	X	X
Solid State reaction		X
Combustion		X
Polymerization		X
Curing		X

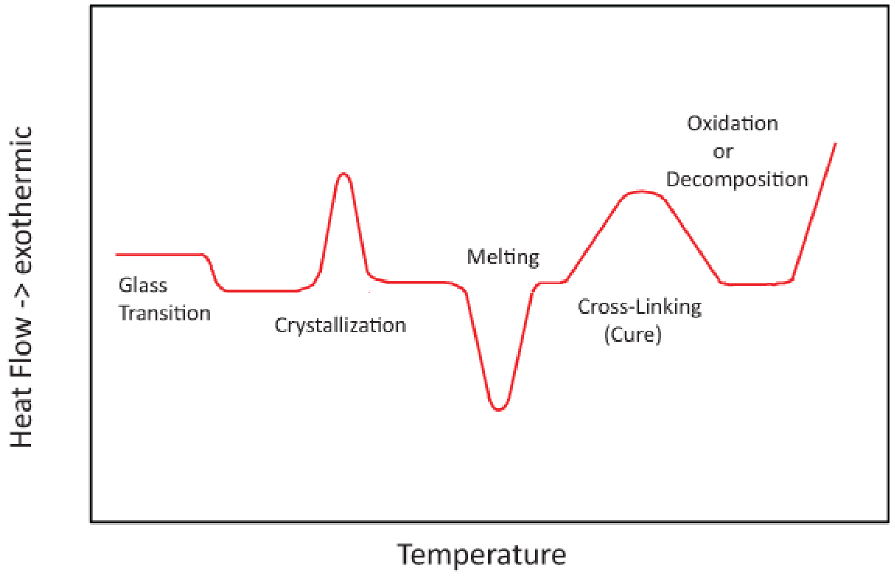

Figure 3.5: Typical DSC Output: Transitions of Interest in a DSC.

III.2.1.6 Information's regarding samples in DSC and TGA

- the crucible is made of alumina.
- the heating rate was 10 K/min.
    - Gas type and Flow rate: Argon 244.3 ml/min

III.2.2 Thermogravimetric analysis (TGA)

The thermogravimetric analysis measures the amount and rate of change in the weight of a material as a function of temperature or time in an atmosphere of nitrogen, helium, air, other gas, or in a vacuum. Measurements are used primarily to determine the composition of materials and to predict their thermal stability at temperatures up to 1200 °C. The technique can characterize materials that exhibit weight loss or gain due to decomposition, oxidation, or dehydration. Inorganic materials, metals, polymers and plastics, ceramics, glasses, and composite materials can be analysed via this technique.

Applications of TGA include predictions of:

- Thermal stability of materials
- Oxidative stability of materials
- Composition of multicomponent systems
- The estimated lifetime of the product
- Decomposition kinetics of materials
- The effect of reactive or corrosive atmospheres on materials
- Moisture and volatiles content of materials

In nanotechnology, much research has been performed in the area of thermal stability prediction of nanomaterials using TGA [226]. TGA also gives evidence for the surface modification of nanoparticles by other functional groups and the amount of surface-modifying agents attached to the surface of nanoparticles. Ramanujan et al. demonstrated the use of TGA to determine the amount of polyvinyl alcohol (PVA) bound to the iron oxide nanoparticles [227]. TGA can give information on nanoparticle coatings and the purity of some nanoparticles. Mansfield et al. investigated the purity of silica nanoparticles using microscale TGA [228].

III.2.2.1 Limitations

- Only provides meaningful data when a change in mass occurs.
- Some liquids can be measured, but this is generally very difficult to do.
- Very small samples are used, so non-homogeneous materials generally cannot be tested

III.2.3 Dilatometry

III.2.3.1 Introduction to thermal expansion

Most materials change their dimensions when the temperature changes. Usually, the dimension increases with increasing temperature, and this is referred to as a positive thermal expansion. The thermally induced change in the dimension of material in a confined environment can lead to significant stress. If the stress exceeds the strength of the material, the material will shatter, quite possibly with disastrous consequences.

On the other hand, some materials shrink with increasing temperature, giving rise to negative thermal expansion. Some materials exhibit 'thermomiotic' (from the Greek, 'thermo' for 'heat' and 'mio' for 'contract') behaviour only in certain directions, making the overall thermal expansion positive or negative.

Different methods applied on measuring the expansion are called dilatometry (from Latin: dilatare = to expand). This measuring technique uses small specimens for the determination of coefficients of thermal expansion and phase transformations in the solid state of metals, glass, ceramics, polymers, concrete, etc. The advantage of dilatometry is its simplicity in experimental realization and interpretation. In principle, any time-temperature cycle can be applied by appropriate heating and cooling. A restriction is that most dilatometers measure the solid state only and fail in the case of melting. For measurement in the liquid state special dilatometers exist. Within this thermal cycle the length change of a specimen, which is directly correlated with coefficients of thermal expansion, phase transitions, and lattice defects, is monitored.

Above absolute zero, atoms or molecules within a crystalline or amorphous solid state are vibrating. The higher the temperature the more vigorous the vibrations become forcing the effective distance of atoms to increase within the boundaries of the solid-state body. Therefore, the solid expands, which can be measured with the dilatometer. Consequently, the CTE is positive: an increase in temperature leads to an additional elongation. Crystals with low crystal symmetry (crystal anisotropy, e.g., aluminium oxide) and many composites (structure anisotropy, e.g., carbon-fibre-reinforced polymer) have an anisotropic CTE. The CTE is related to the direction of the crystal axis or structure axis, respectively [229].

Some materials have a negative coefficient of thermal expansion (NTE) [230]. These materials contract in the case of an increase in temperature. There are some physical reasons for an NTE. In some cases, this is an intrinsic property associated with the composition and the particular structure, e.g., structural subunits in nitrides or oxides like ZrW_2O_8 [231]. These substructures can rotate relative to each other and for higher temperatures, a configuration with lower dilatation is preferred.

III.2.3.2 Coefficient of thermal expansion (CTE)

The coefficient of thermal expansion, generally abbreviated as α and also called CTE, can be defined in a particular direction, ℓ, as [232]:

$$\alpha_l = \frac{1}{l}\left(\frac{\delta l}{\delta T}\right)_P$$

where, for example, ℓ could be one of the principal crystallographic directions (a, b, or c, giving α_a, α_b, and α_c, respectively), and T is temperature. The volumetric CTE, α_V, is

$$\alpha_V = \frac{1}{V}\left(\frac{\delta V}{\delta T}\right)_P$$

where V is the volume. Note that both ℓ and α_V are intrinsic to a given material at a given temperature, and independent of the material's size. Both α_V and the directional values of α have units of K^{-1}, but it is important to distinguish the type of CTE. If the material is cubic, $\alpha_V = 3\alpha_l$ but for less symmetric structures, the relationship is not so simple. Indeed, the α values in different directions could have different signs making α_V close to zero. One needs to read the thermal expansion literature carefully to ascertain which type of thermal expansion coefficient is being described.

III.2.3.3 Method

Pushrod dilatometry is a thermoanalytical technique for characterizing dimensional changes (expansion or shrinkage) of a material (solids, powders, pastes and liquids) under negligible load when subjected to a controlled temperature/time program. The measurements may be performed across a temperature range (e.g., from 800 °C to 1600 °C), or a specific controlled temperature program to mimic industrial processes, firing regimes, or a material's operating environment. The coefficient of thermal expansion is defined as the degree of expansion divided by the change in temperature. A precise understanding of thermal expansion behaviour provides crucial insight into firing processes, the influence of additives, reaction kinetics and other important aspects of how materials respond to environmental changes. Typical applications include the determination of the coefficient of thermal expansion, annealing studies, determination of glass transition point, softening point, densification, kinetics and sintering studies.

III.2.3.4 Device characteristics of (Netzsch 402C dilatometer)

- Temperature range (°C)
- Heating rate (K/min)
- Temperature precision (K)
- Cooling system (air, water, nitrogen…)
- Atmosphere (inert, vacuum, oxidizing, reducing…)
- Measuring range (µm)
- Load at the sample (cN)
- Δl resolution (nm/digit)
- Sample, diameter and length (mm)

Figure 3.6: DIL 402C – 1600 °C.

Figure 3.7: Technical showcase (longitudinal cross section of DIL 402 C – 1600 °C).

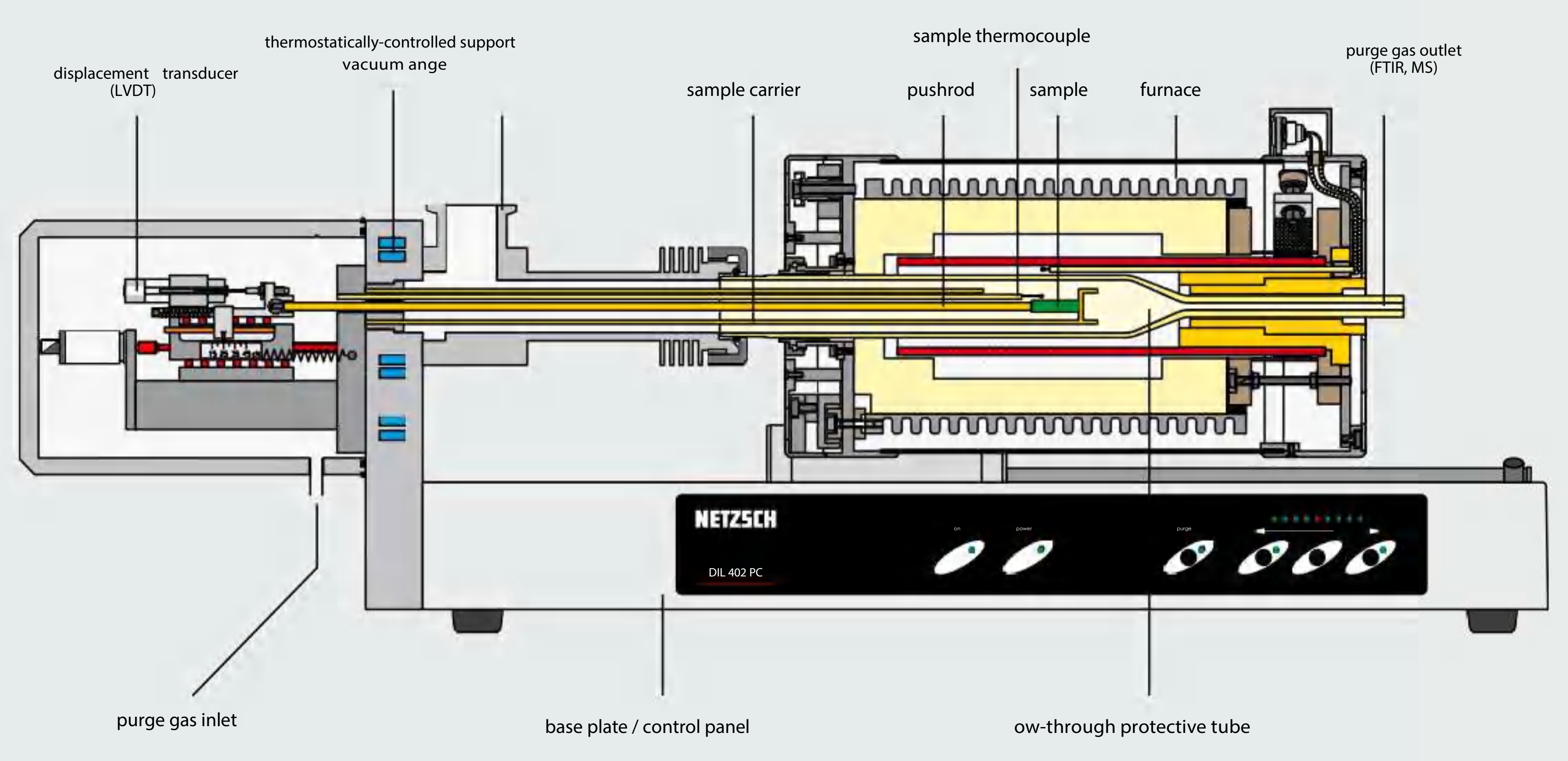

III.2.4 X-Ray diffraction

X-ray diffraction (XRD) is an essential tool in material science. It is a versatile technique for the identification of phases present in a sample. Much information on metal matrix nanocomposites-MWCNTs can be gathered using this technique.

The X-ray diffraction peaks obtained from the samples are characterized by diffraction angles θ_{hkl} and I_{hkl} intensities depending on the lattice cell and the wavelength radiation λ, used. The *hkl* Miller indexes correspond to the diffracting crystallographic planes (d_{hkl} is the inter-planes distance). These three parameters are connected through the Bragg relation [233]:

$$2d_{hkl}\sin\theta_{hkl} = n\lambda \qquad (1)$$

The position of the diffraction peaks gives access to the distance d_{hkl} between crystallographic planes, the structure and lattice parameters. If a monochromator is used, *l* is perfectly defined. In order not to lose intensity, two close wavelengths are used simultaneously; it is the case with a copper anti-cathode whose emission spectra contain the two close wavelengths $\lambda_{k_{\alpha 1}} = 1.540562$ Å and $\lambda_{k_{\alpha 2}} = 1.54390$ Å.

A fit of each diffraction peak by mixed of Gaussian and Lorentz functions, corresponding to $\lambda_{k_{\alpha 1}}$ and $\lambda_{k_{\alpha 2}}$ the wavelength can be carried out by using ORIGIN software for example. These functions have the following form:

$$y = y_0 + \frac{2A}{\pi}\frac{\beta}{4(x-x_0)^2+\beta^2} \qquad (2)$$

In which:

y_0 – is the value of the continuous background taken at the origin

A – is the total area under the curve after subtraction of the background;

x_0 – is the x-coordinate to the maximum of the y-coordinate;

β – is called the Full Width of the peak at Half Maximum y value (FWHM).

These functions fit the profiles of diffraction peaks and especially allow a very good evaluation of FWHM. The diffraction peak width has to be corrected by an "instrumental width" β_{st}. The shape and the intrinsic width β_{in} of the diffraction peaks are dependent on the dimensions of the coherence diffraction domains called the "grain size" and on their mechanical state (strains). In classical materials without stresses and well crystallized over a micron-scale the peak width β and the instrumental width β_{st} are equal (β_{in} is null or very small), but in nanomaterials, they differ significantly.

XRD has been used to study the reaction between metals and carbon species and qualitatively. It provides much information on MMN-CNT composites as well as determining phase composition after processing. It gives immediate information on the effect of the processing technique on the changes in the phase present in the matrix. For example, in bulk-metallic-glass-CNT composites, it shows whether the matrix is still crystalline [234]. Qualitative information on the alignment of the CNTs can be made from the relative intensities of the different peaks [235]. In nanocomposites, the mass fraction of CNTs is generally low, and only the (002) peak is discernible.

XRD has been used to study the reaction between metals and carbon species and qualitatively compare the reactivity of different carbon species. Another use of XRD is in determining the crystallite/grain size from the broadening of the peaks using the simplified Scherrer formula

$$\beta = \sqrt{\beta_s^2 - \beta_i^2} = \frac{0.9\lambda}{d\,cos(\theta)}$$

Where β is the corrected full width at half maximum (FWHM) of the peak at 2θ (in radians), β_s is the FWHM for the sample (in radians), β_i is the FHWM due to instrumental broadening (in radians), λ is the wavelength, θ is the corresponding Bragg's angle, and *d* is the average grain size of the material.

The crystallite size and lattice strain in the powder particles can be determined using the X-ray peak broadening techniques. X-ray diffraction peaks are broadened due to (a) instrumental effects, (b) small particle size, and (c) lattice strain in the material.

The individual contributions of these effects to the total broadening can be separated using standard techniques and these may be found in some of the textbooks [236] and/or research papers [237–239].

III.2.5 Raman spectroscopy

Raman spectroscopy is commonly used for characterizing carbonaceous materials such as graphite (graphene), MWCNTs and SWCNTs bundles because it is one of the most sensitive characterization tools for these nanostructures [240,241]. The Raman experiment is simple and can be done at both room temperature and pressure with no specific environment, it's popularity stems from the fact that is fast, non-destructive and non-invasive, and the instrumentation is generally available to a wide user community, providing a wealth of information about the purity, defects and tube alignment and assists in the distinguished presence of MWCNTs relative to other carbon allotropes [241].

Several reports have indicated that Raman spectroscopy can have qualitative and even quantitative characterization power. Because much less theoretical work has been devoted to understanding the Raman spectrum of MWCNTs, the interpretation of the experimental spectra is usually based on well-established results obtained for SWCNTs. This approach has proven valuable but has also shown important limitations since some effects, absent in SWCNTs, are often found in the spectra of MWCNTs [242]. For Raman scattering, MWCNTs can be said to be an ensemble of carbon nanotubes with diameters ranging from small to very large [243].

Raman spectrum originates due to the interaction of radiation (light) with the vibrational modes of a molecule. When coherent light radiation is an incident on a sample of the incident beam may be used up to excite a characteristic vibration or a vibration may die out giving its energy to the incident photon. If the frequency of a vibrational mode of a molecule and the incident beam is υ_m and υ_0, respectively, the resulting new photon will have a frequency of $\upsilon_0 – \upsilon_m$ (Stokes Raman Scattering) or $\upsilon_0 + \upsilon_m$ (Anti-Stokes Raman Scattering), respectively. This is known as the Raman Effect. It is a very weak phenomenon with an intensity of scattered radiation approximately 10^{-5} to 10^{-7} times that of the incident beam. Hence, lasers are employed as the incident light source owing to their high intensities and coherent nature. Some of the common radiations that have been used are the red light (wavelength $\lambda = 633$ nm) from a He-Ne laser, red light ($\lambda = 785$ nm) from a Ti-sapphire laser and green light ($\lambda = 514.5$ nm) from an argon-ion laser. The reflected beams with lower energy have a lower wavenumber (reciprocal of λ) and the difference, known as Raman shift (expressed in cm^{-1}), corresponds to the characteristic vibration frequency of the molecule. The dipole moment induced in a molecule must be affected by the molecular vibration for the Raman Effect to occur and hence only those species for which the polarizability changes with vibration are Raman active. An excellent introduction to Raman spectroscopy can be found in the textbook by Ferraro et al [244].

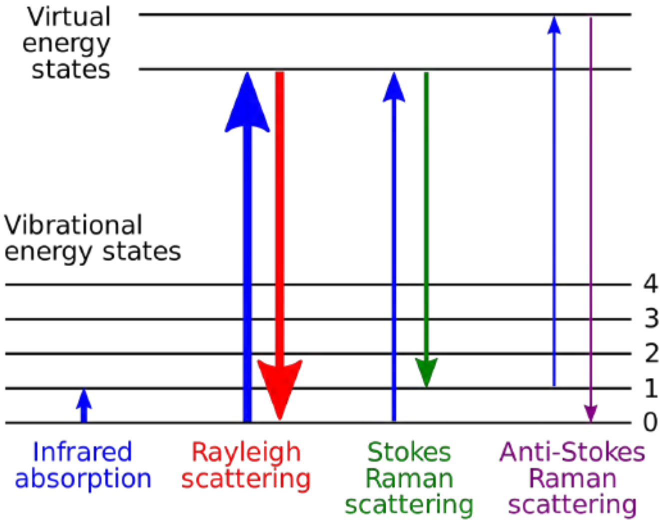

Figure. 3.8: Energy level diagram showing the origin of infrared absorption, Rayleigh scatter, Stokes Raman scatter, and anti-Stokes Raman scatter

Raman spectroscopy is o commonly used to charaterise the carbon nanotube reinforcing nanocomposites because it delivers a conclusive signature of CNTs presence.

Raman spectrum of a natural graphite single crystal shows a single peak at 1575 cm^{-1} corresponding to the E_{2g} vibration mode [245]. The Raman spectrum of different types of carbon nanotubes and species has been well documented in the literature [246–248]. CNTs show a peak at 1575 cm^{-1}, which is called the G-peak. Disorder in the CNTs and presence of sp^3 defects leads to an A_{1g} radial breathing mode peak at 1348 cm^{-1}, which is known as the D-peak (band as well). A second-order peak of the D-peak is observed at 2691 cm^{-1} and is called the G'-peak. SWCNTs show an additional unique peak at ~180 cm^{-1} for vibrations corresponding to the radial expansion and compression. This peak is known as radial breathing mode (RBM). Figure 3.8 shows the Raman spectra of SWCNTs.

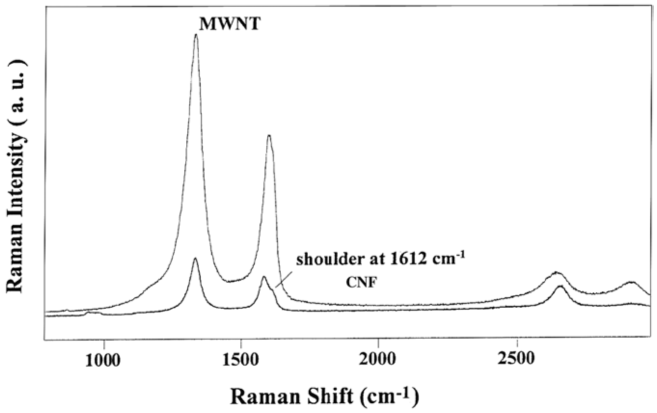

Figure. 3.9: Raman spectroscopic features of an MWCNT and CNF. All multiwalled structures exhibit a tangential graphitic G-band centred at 1589 cm^{-1} and a D-band centred at 1330 cm^{-1}. The CNF, in addition, shows a shoulder peak at 1612 cm^{-1} distinguishing it from an ideal MWCNT [249].

The Raman shift of the RBM peak changes with the diameter of the small nanotubes with diameter <2 nm and is given by the relation:

$$\tilde{\upsilon}(cm^{-1}) = \frac{248}{d(nm)}$$

where *d* is the diameter of the carbon nanotube in nanometres. The G'-peak, which is the overtone of the D peak, has been observed to shift significantly when the nanotube composites are stressed [250] and can be used to predict the stress state of the CNTs in the composite. The position of the G' band has been used to calculate the strain in the nanotubes and by calculating the corresponding thermal stresses, the approximate elastic modulus of CNTs also been estimated [251]. Important information about the structure of the CNTs can be obtained from the ratio of the intensities of the D- and G-peak (I_D/I_G). An increase in the I_D/I_G ratio after MM-CNT composite synthesis means an increase in the defect density and hence implies some sort of damage incurred to CNTs while processing. Similarly, a decrease in the I_D/I_G ratio may indicate graphitization by the annealing effect produced during processing. By studying the changes in the I_D/I_G ratio, one can make qualitative conclusions on the changes in the CNT structure during various stages of processing. Mechanical milling of Al-CNT powder mixture followed by hot rolling led to an increase in I_D/I_G ratio and a shift in the G-peak from 1572.7 cm^{-1} to 1596.3 cm^{-1}. This has been attributed to the increase in the inter-atomic distance of carbon atoms during the milling procedure, which may cause a decrease in the bonding potentials and result in the decline of the Raman vibration frequency [252].

Table 3.2: Summary of spectral features derived from Raman spectroscopy.

Mode	Designation	Attribute
Sub 500 cm^{-1}		Presence of Fe catalyst
Sub 500 cm^{-1}		Radial breathing modes. Evidence of MWCNTs with high-purity, low-defect material, thin innermost layers
650 cm^{-1}		Appears following intense laser irradiance
1350 cm^{-1}	D	Attributable to the presence of disordered amorphous carbon; double resonance effects in sp^2 carbon [253]. The frequency of the D-band peak increases with increasing laser energy. Note that this peak results from amorphous carbon, not defects, in the tube walls [254,255]
1590 cm^{-1}	G	This band corresponds to the tangential vibrations of the graphitic carbon atoms. In graphite, a single peak is present at 1582 cm^{-1}
1617-1625 cm^{-1}	D’	Associated with intercalated graphite compounds (but not graphite), increasing disorder by functionalization and strain in the C–C bond vibrations [256]
1850 cm^{-1}		Endo et al. [257] and Fantini et al. [259] proposed a coalescence-inducing mode associated with short carbon chains with an odd number of atoms, interconnecting nanotube surfaces
1855 cm^{-1}	G’	Jinno proposes the existence of chainlike carbon materials inside nanotubes [259]
2700 cm^{-1}		The G’ band is caused by two-phonon scattering around the K point of the Brillouin zone. This mode is known to be sensitive to increasing defect density, but not as significant as the first-order mode. The mode has significant contributions from regions near the K and M points, yielding peaks at approximately 2700 cm^{-1} and approximately 2730 cm^{-1}, respectively [256]. The intensity of this peak depends strongly on the metallicity of the nanotube [260]
3240 cm^{-1}		Second-order mode of D’: increases in intensity with increase in defects in a manner similar to the D’ peak at 1617 cm^{-1}; it can be seen as part of the density of states. Defect-induced [256]

III.2.6 Infrared spectroscopy

The absorption of infrared (IR) radiation causes excitation of vibrations of the atoms of a molecule or the crystal lattice and causes bands in the spectra which are generally presented in the unit wave number $\tilde{\nu}$ in cm^{-1}.

There are there main processes by which a molecule can absorb radiation. Each of these routes related to an increase of energy that is proportional to the light absorbed. Firstly, when absorption of radiation causes a higher rotational energy level in rotational transition. Secondly, vibrational transition which occurs on absorption of quantized energy that leads to an increase in vibrational energy level. Third one involves electrons of molecules being raised to a higher electron energy, which is the electronic transition.

The energy levels can be rated in the following order: electronic > vibrational > rotational. Each of these transitions differs by an order of magnitude. Rotational transitions occur at lower energies (longer wavelengths) and this energy is insufficient and cannot cause vibrational and electronic transitions but vibrational (near infra-red) and electronic transitions (ultraviolet region of the electromagnetic spectrum) require higher energies.

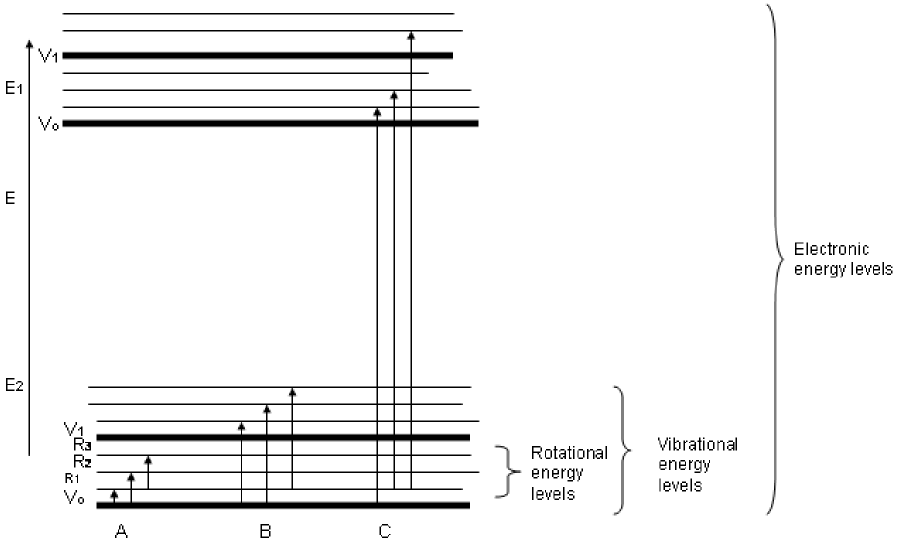

Figure. 3.10: Energy levels for a molecule. Possible transitions that occur: (A): Pure rotational Transitions, (B) rotational-Vibrational Transitions, (C) Rotational-Vibrational-Electronic Transitions.

Infrared spectrum ranges			
Region	Wavelength	Wavenumber $(\tilde{\nu})$, cm^{-1}	Frequencies (ν), Hz
Near	0.78–2.5	12800–4000	$3.8\times10^{14} - 1.2\times10^{14}$
Middle	2.5–50	4000–200	$3.8\times10^{14} - 1.2\times10^{14}$
Far	50–100	200–10	$3.8\times10^{14} - 1.2\times10^{14}$
Most Used	2.5–15	4000–670	$3.8\times10^{14} - 1.2\times10^{14}$

The infrared range of the electromagnetic spectrum is divided into three regions, named after their relation to the visible spectrum:

– ***Near-infrared (NIR) (***$\tilde{\nu}$ ranges from 14,000 to 4,000 cm^{-1} and wavelength range from 0.8 to 2.5 μm) lying adjacent to the visible region excites so-called overtone or higher harmonic vibrations (higher harmonics).

– ***Mid-infrared*** ($\tilde{\nu}$ range from approximately 4,000 to 200 cm^{-1} and wavelength ranges from 2.5 to 25 μm) excites mainly fundamental vibrations. This part of the infrared range may be used to study the structure of molecules that we shall be concerned about within this book. In general, the name "IR-spectroscopy" conventionally refers to the mid-IR region.

– ***Far-infrared*** ($\tilde{\nu}$ range from approximately 200 to 10 cm^{-1} and wavelength range from 25 to 1,000 μm) is the lowest-energy region which excites mainly lattice vibrations or can be used for rotational spectroscopy.

Infrared spectroscopy is a powerful and versatile technique for identifying the presence of functionalities groups, it provides information specific to the group itself — in our case of study, it reveals information about functional groups of the interaction between matrix–tube surface—, and also on the interaction of the group with other parts of the molecule and the spatial properties of the group.

Since it's based on the vibrations of the atoms of a molecule. The infrared spectrum is commonly obtained by passing infrared electromagnetic radiation through a sample that possesses a permanent or induced dipole moment and determining what fraction of the incident radiation is absorbed in particular energy [261].

The energy of each peak in an absorption spectrum corresponds to the frequency of the vibration of a molecule part, thus allowing qualitative identification of certain bond types in the sample. An IR spectrometer usually records the energy of the electromagnetic radiation that is transmitted through a sample as a function of the wavenumber or frequency.

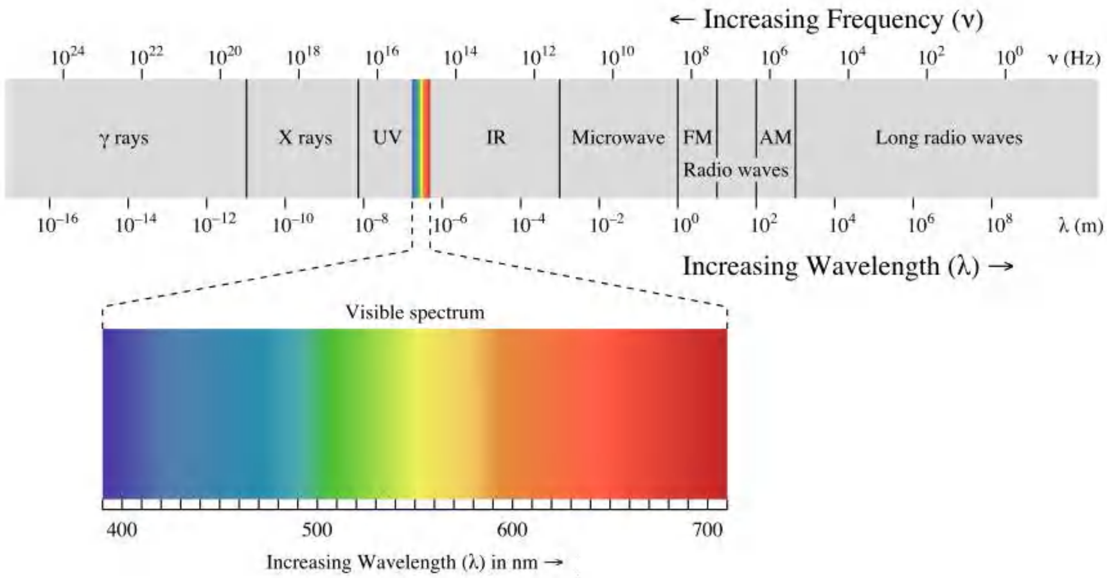

Figure. 3.11: The electromagnetic spectrum.

Table 3.3: Comparison of Infrared absorption and Raman

	Near-IR	*Mid-IR*	*Raman*
Spectral range (cm^{-1})	14000-4000	4000-400	4000-50
Analysis of:			
Gases	No	Yes	Yes
Liquids	Yes	Yes	Yes
Solids	Yes	Yes	Yes
Aqueous systems	Difficult	Very difficult	Yes
Macroscopic samples	Yes	Yes	Yes
Microscopic samples	No	Yes	Yes
Signal	Strong	Strong	Weak
Sampling	Easy	Difficult	Easy
Through glass	Yes	No	Yes
windows in situ	No	No	Yes

Quantitative	Yes	Difficult	Yes
Noninvasive	Yes	No	Yes
Fibre optic interfacing	Yes	No	Yes
Information content	Low. Limited to O-H, N-H, and C-H vibrations	High	High
Reaction monitoring and modelling	Requires chemometrics	Yes	Yes

III.2.6.1 Advanatgeous of IR

- ***High Scan Speed:*** can get information for the whole range of frequency simultaneously, within short time down to 1 second. Therefor, IR can be used to analyze a substance that is not very stable and finish the scan before it start to decompose.
- ***High Resolution:*** The resolution of general prism spectrometer is only about 3 cm^{-1}, but the resolution of infrared spectrometer is much higher. For example, the resolution of Grating infrared spectrometer could be 0.2 cm^{-1}, the resolution of FT infrared spectrometer could be 0.1-0.005 cm^{-1}.
- ***High Sensitivity:*** With Fourier Transform, the infrared spectrometer doesn't need to use the slit and monochromator. In this way, the reflection specularity will be increased and the loss of energy in the analysis process will be decreased. Therefore the energy that reaches the detector is large enough and even very small amount of analytes could be detected. Nowadays, the infrared spectroscopy could detect the sample as small as 1-10 grams.
- ***Wide Range of Applicatipns:*** IR spectroscopy could be used to analyse almost all organic and some inorganic compounds. It has a wide range of application in both qualitative and quantitative analysis. Also, the sample of Infrared spectroscopy doesn't have phase constraints (gas, liquid or solid).
- ***Large amount of Information:*** IR Spectra could givea lots of structural information, such as the type of compound, the functional group of compound, the

stereoscopic structure of compound, the number and position of substituent group and so on.

- ***Non-Destructive:*** Infrared Spectroscopy is non-destructive to the sample.

III.2.6.2 Disadvanatges of IR

- ***Sample Constraint:*** Infrared spectroscopy is not applicable to the sample that contains water since this solvent strongly absorb IR light.
- ***Spectrum Complication:*** The IR spectrum is very complicated and the interpretation depends on lots of experience. Sometimes, we cannot definitely clarify the structure of the compound just based on one single IR spectrum. Other spectroscopy methods, such as (Mass Spectrometry) MS and (Nuclear Magnetic Resonance) NMR, are still needed to further interpret the specific structure.
- ***Quantification:*** Infrared spectroscopy works well for the qualitative analysis of a large variety of samples, but quantitative analysis may be limited under certain conditions such as very high and low concentrations.

IV

RESULTS AND DISCUSSION

IV.1 Thermal analysis

IV.1.1 Simultaneous thermal analysis (STA), Calorimetry and thermogravimetry

Fe–Cu–X% MWCNTs where X% is 0, 0.5, 1 & 2%.vol respectively with different milling times (20 min, 60 min and 120 min).

IV.1.1.1 Multiwalled carbon nanotubes

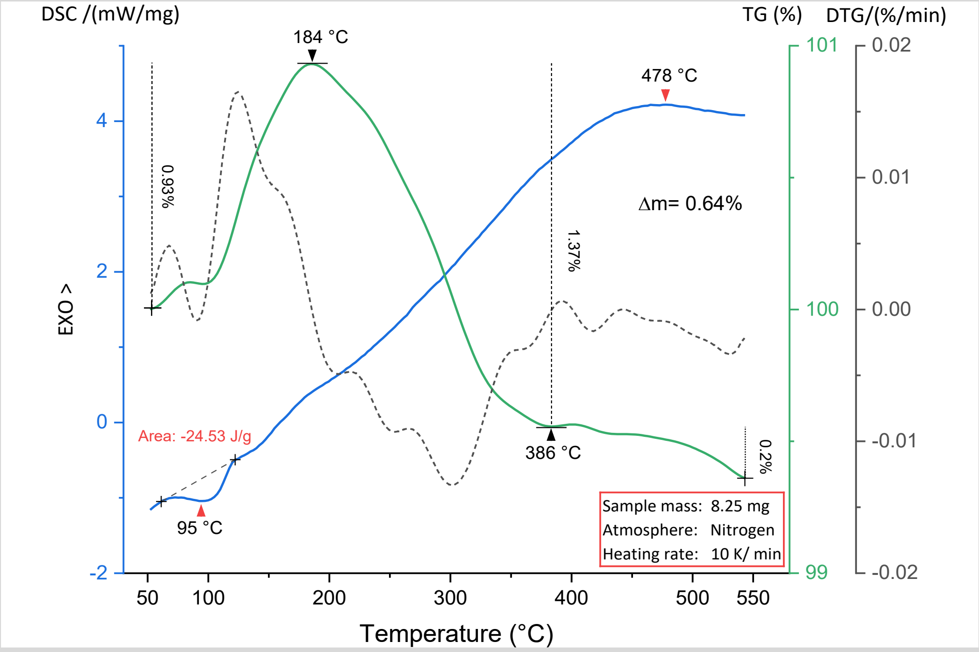

Figure. 4.1: Calorimetric and thermogravimetric charts of multiwall carbon nanotubes.

Both calorimetric and thermogravimetric data of the used MWNCTs in the preparation of the studied iron-copper nanocomposite are shown in the figure. 4.1. For the calorimetric measurements, a presence of a noticeable endothermic event at the temperature range of 50–140 °C.

As for the thermogravimetric data, there are two distinctive regions, from ambient to around 184 °C, oxidation possible due to metal particles residues from the used catalysts, secondly, from 184 °C to around 550 °C, a relatively low weight loss followed by flat around 386 °C, then continuing to decrease to record a weight loss of 0.2%, that might be due to oxidation with low presence of O_2 in the chamber (contamination) releasing CO and CO_2.

IV.1.1.2. 20 minutes milling time

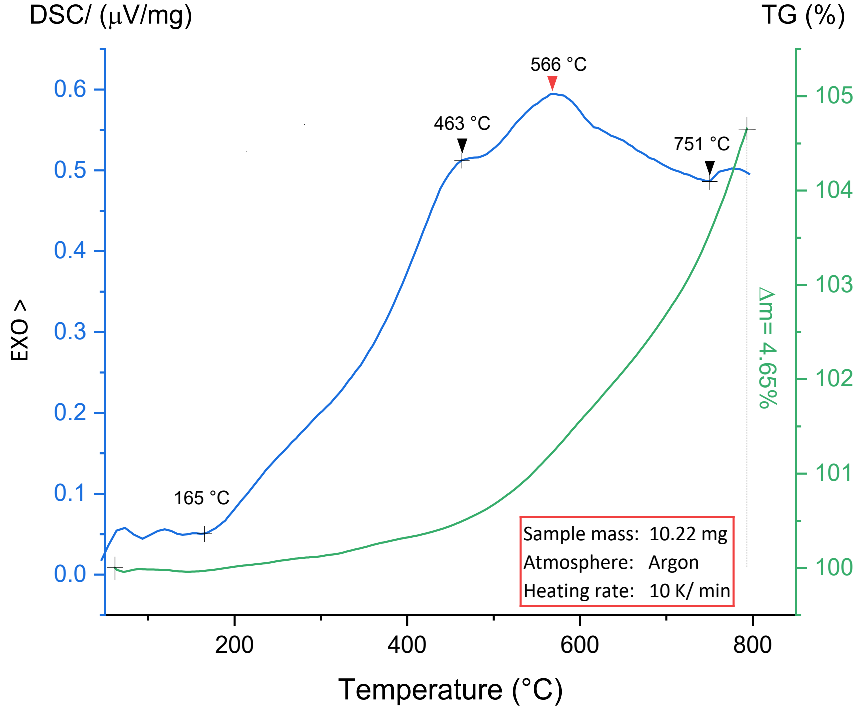

Figure. 4.2: Calorimetric and thermogravimetric charts of Fe–Cu (20 min).

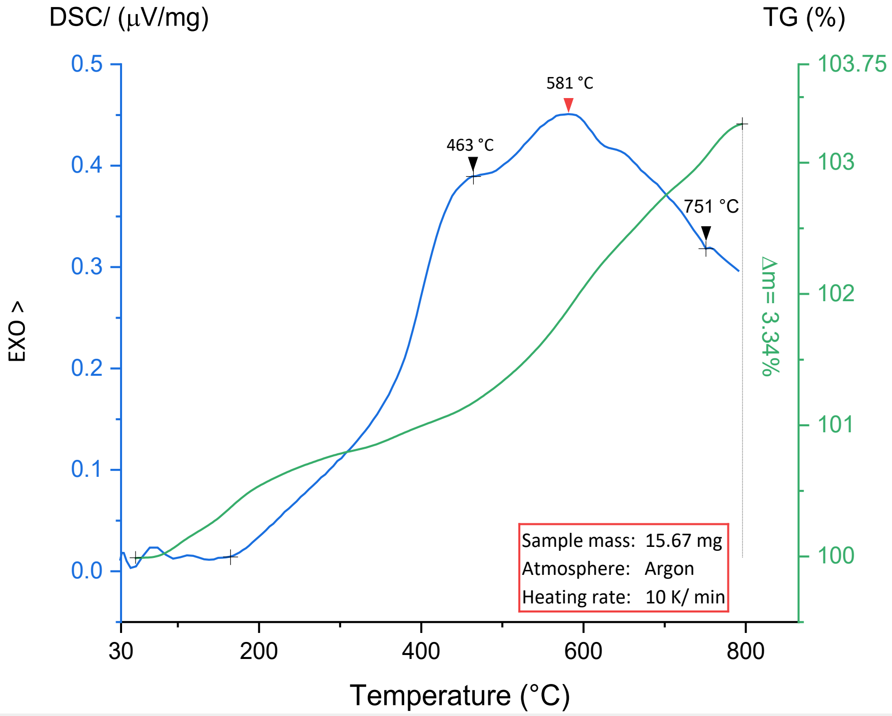

Figure. 4.3: Calorimetric and thermogravimetric charts of Fe–Cu-0.5% MWCNTs (20 min).

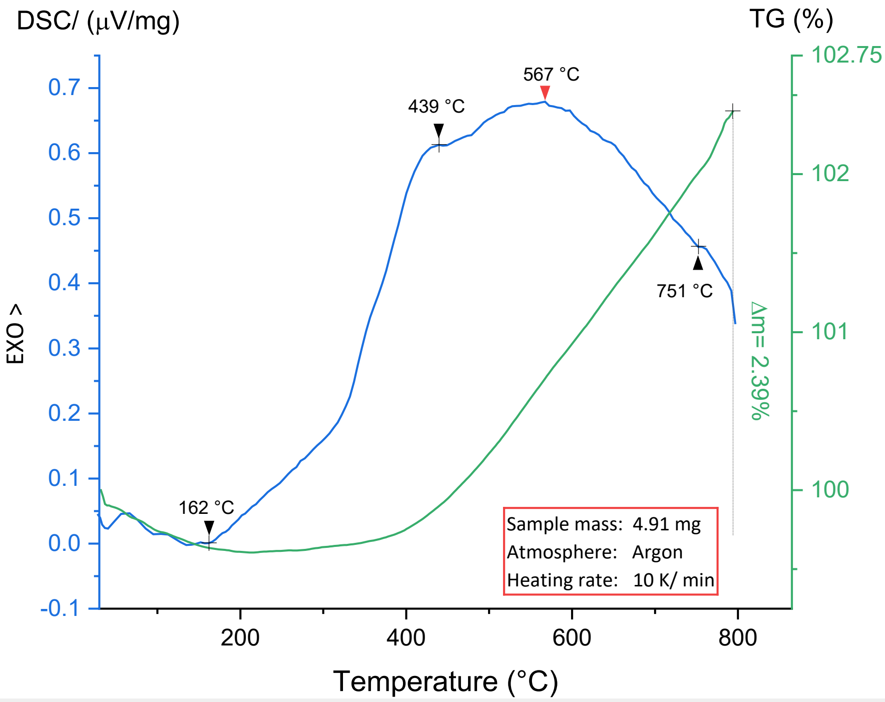

Figure. 4.4: Calorimetric and thermogravimetric charts of Fe–Cu-1% MWCNTs (20 min).

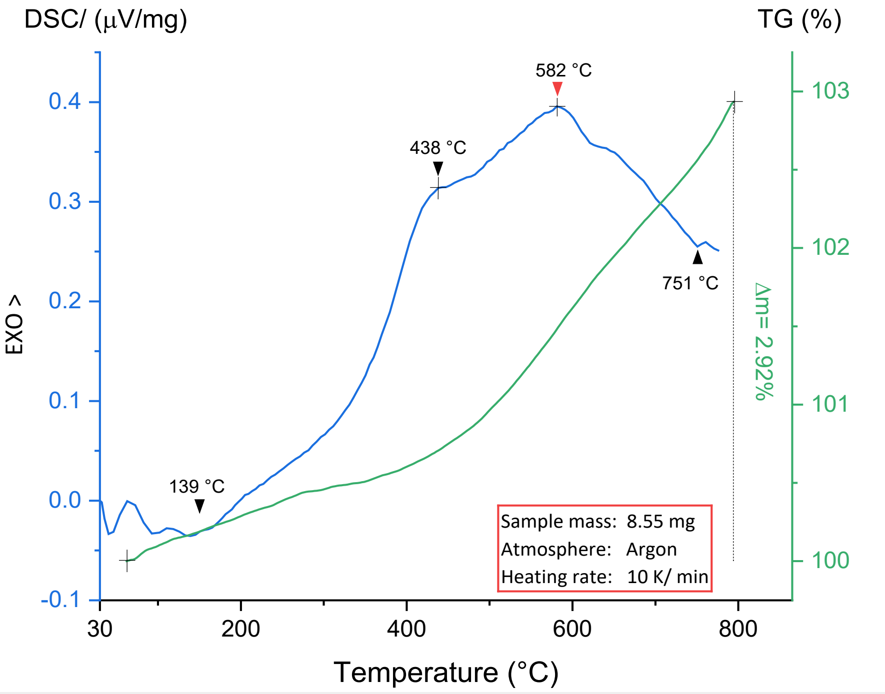

Figure. 4.5: Calorimetric and thermogravimetric charts of Fe–Cu-2% MWCNTs (20 min).

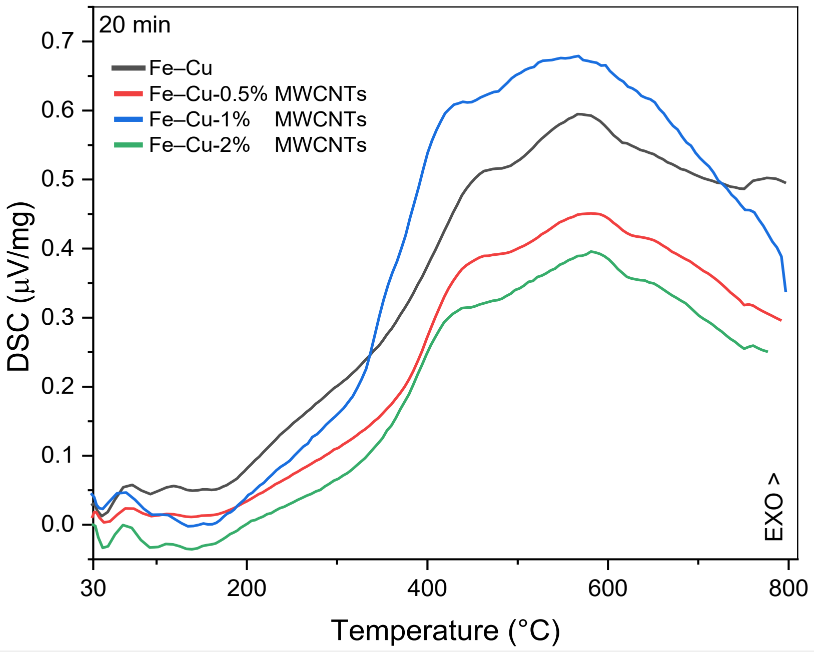

Figure. 4.6: DSC chart of Fe–Cu-X% MWCNTs (20 min).

Figure 4.6 presents the calorimetric measurements of the Fe–Cu-X% MWCNTs nanocomposites with 20 minutes milling time.

The calorimetric charts increase proportionally with rising temperature with the presence of few identifiable anomalies at around 440 °C and 585 °C, respectively. Corresponds to the α-Fe phase transition.

The 1% MWCNTs shows higher calorimetric value peaks at 567 °C, followed by the hosting matrix Fe–Cu, an intersection between these two at around 726 °C and their position reversed, the 1% MWCNTs shows more endothermic behaviour compared to the Fe–Cu at the end of the temperature range.

Both 0.5% and 2% MWCNTs have the same behaviour with low calorimetric values, respectively.

The apex of the charts presenting the heat flow of the Fe–Cu-X% MWCNTs is slightly shifted toward a higher temperature compared to the hosting matrix.

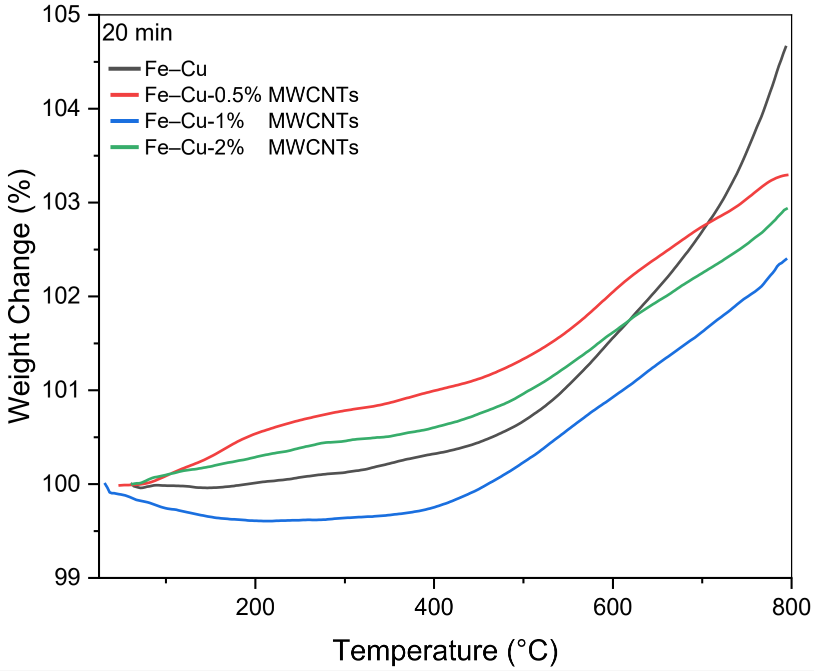

Figure. 4.7: Weight change chart of Fe–Cu- MWCNTs (20 min).

The previous chart presents the thermogravimetric data of the Fe–Cu-MWCNTs nanocomposite milled for 20 minutes.

All samples containing different (or no) concentrations of MWCNTs following near same behaviour (oxidation) with elevated temperature, with different oxidation state (or degree), as for the nanocomposite of 1% MWCNTs, it shows thermal stability (least oxidation) at high temperature followed by 2% MWCNTs, 0.5% MWCNTs and 0% MWCNTs, respectively.

IV.1.1.3. 60 minutes milling time

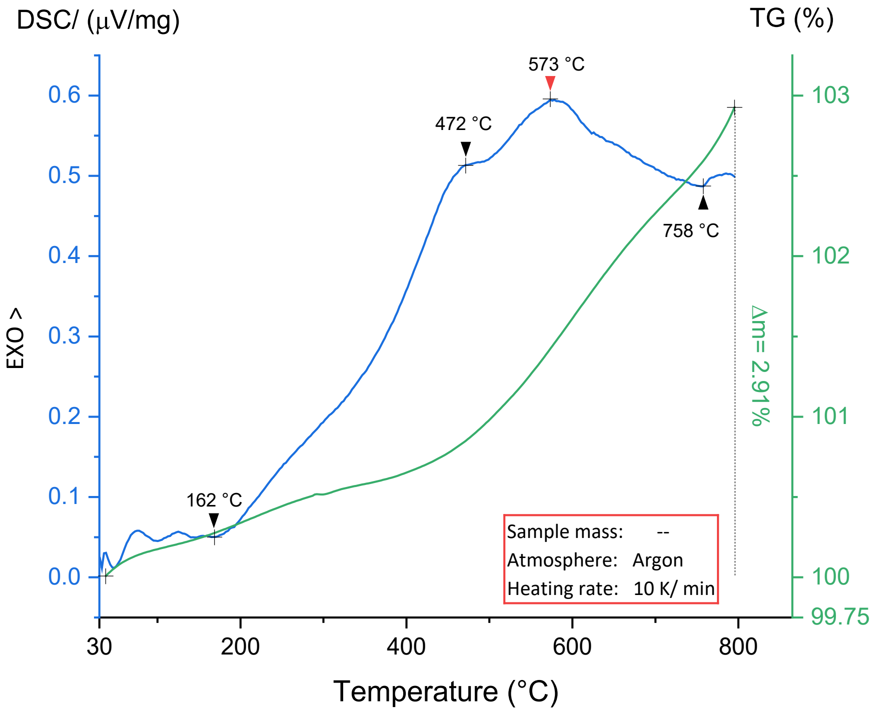

Figure. 4.8: Calorimetric and thermogravimetric charts of Fe–Cu (60 min).

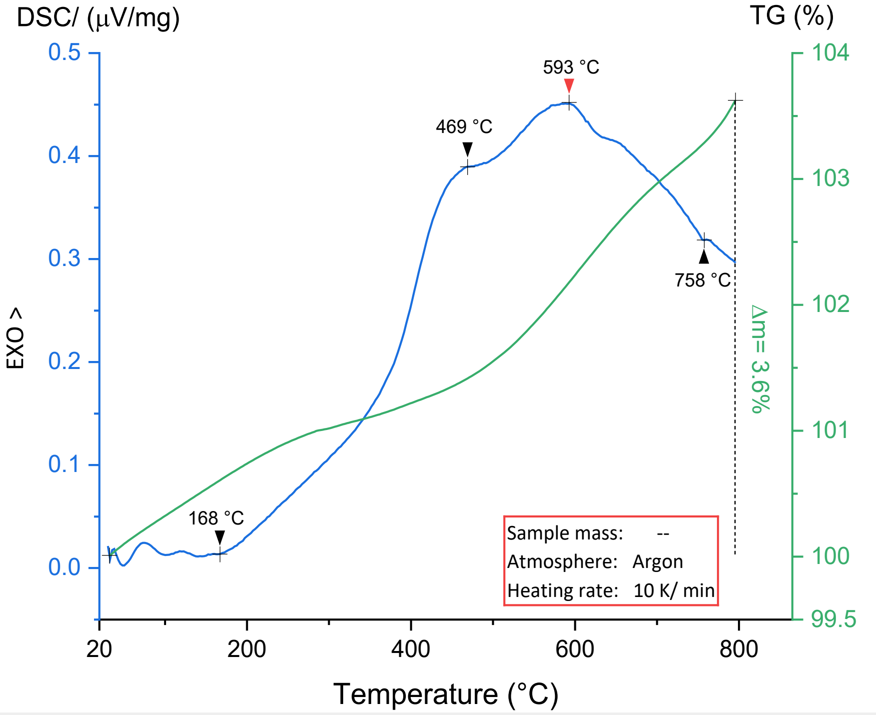

Figure. 4.9: Calorimetric and thermogravimetric charts of Fe–Cu-0.5% MWCNTs (60 min)

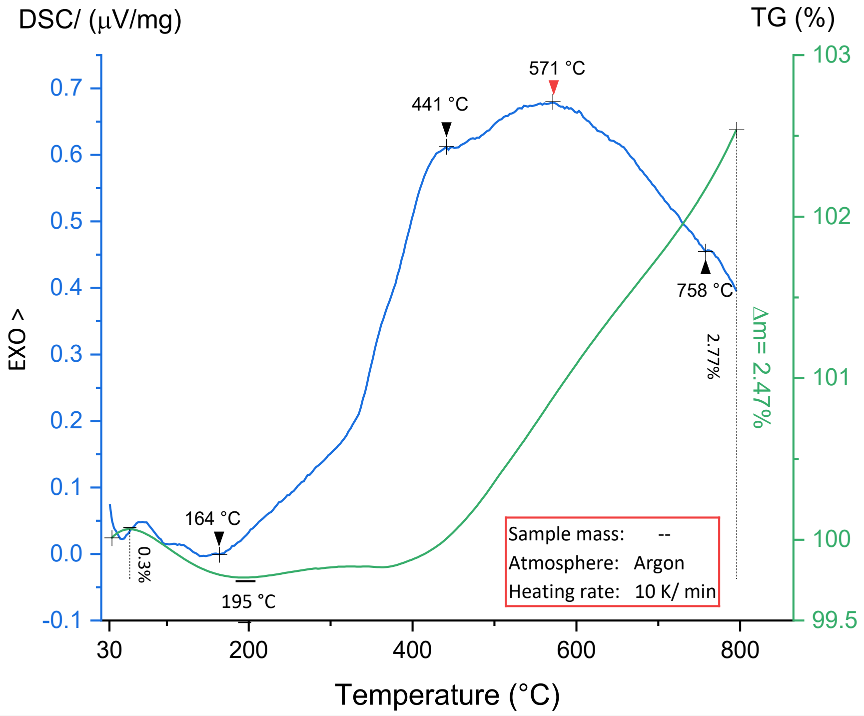

Figure. 4.10: Calorimetric and thermogravimetric charts of Fe–Cu-1% MWCNTs (60 min).

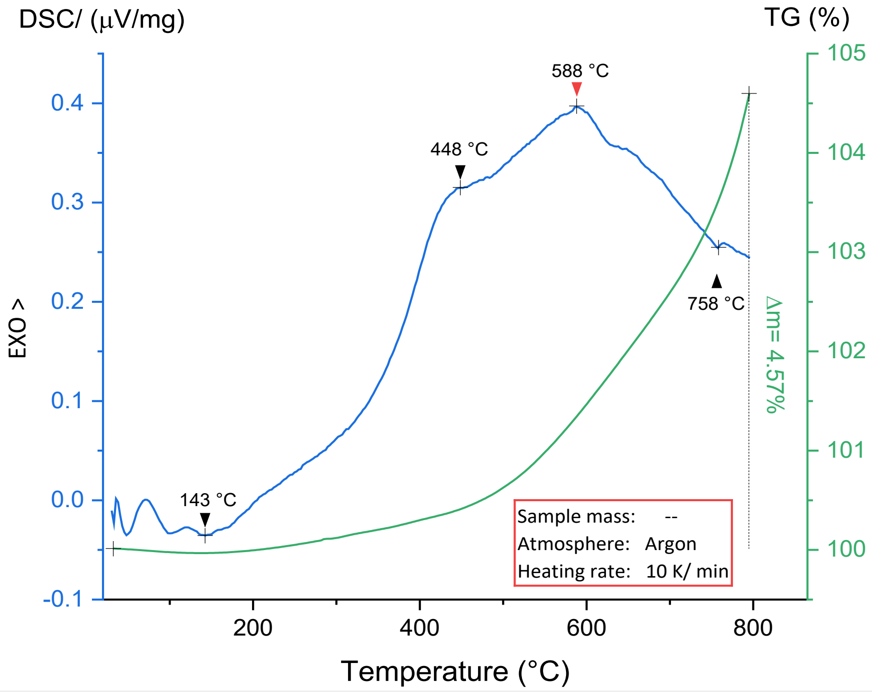

Figure. 4.11: Calorimetric and thermogravimetric charts of Fe–Cu-2% MWCNTs (60 min).

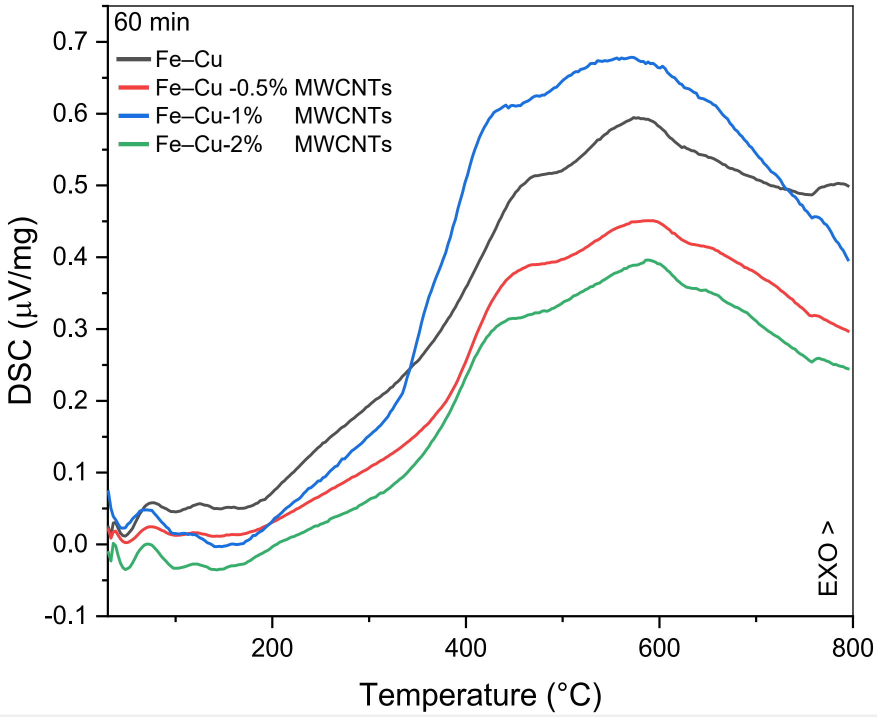

Figure. 4.12: DSC chart of Fe–Cu-X% MWCNTs (60 min).

Figure 4.12 presents the calorimetric thermogram measurements of the Fe–Cu-X% MWCNTs nanocomposites with 60 minutes milling time. The anomaly recorded at the start of the temperature range is fluctuation result by the machine. The heat flow data shows temperature dependence, the calorific capacity rise with the increasing temperature for all samples, also the appearance of an endothermic event around 600 °C. The Fe–Cu-1% MWCNTs shows higher values, followed by the Fe–Cu matrix, then the 0.5% MWCNT and the lowest calorific value is the Fe–Cu-2% MWCNTs.

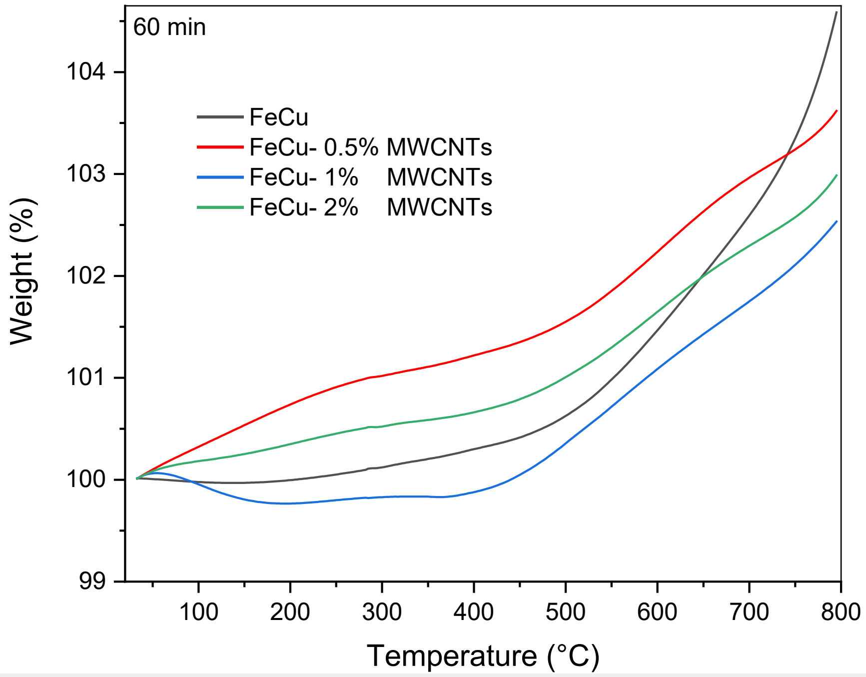

Figure. 4.13: Weight change chart of Fe–Cu-X% MWCNTs (60 min).

Figure 4.13 shows the thermogravimetric data of the Fe–Cu-MWCNTs nanocomposite milled for 60 minutes. Nothing changed in the thermogravimetric compared with the previous samples of the 20 minutes milling time, they have near identical behaviour. The sample containing 1% MWCNTs shows the least oxidation state, followed by 2% MWCNTs which trade place with the Fe–Cu matrix around 640 °C, then the 0.5% MWCNTs around 720 °C.

IV.1.1.4. 120 minutes milling time

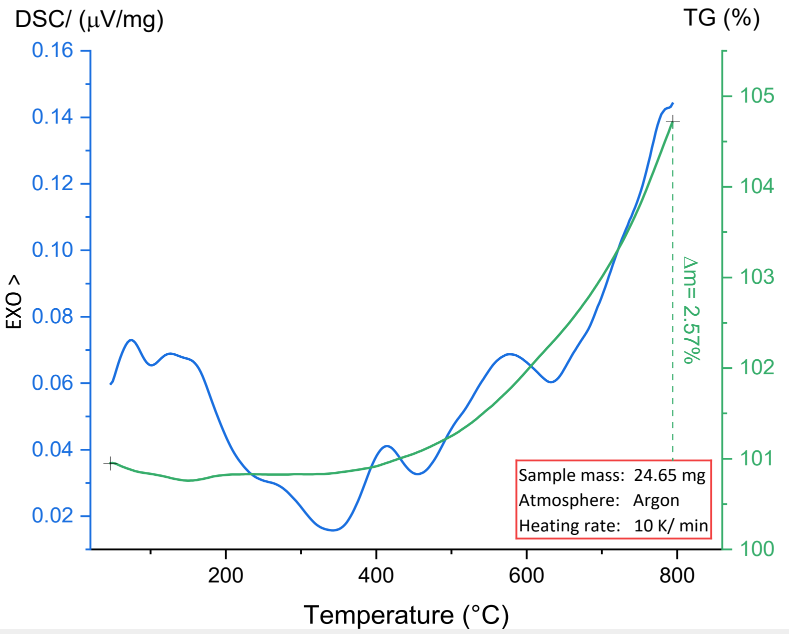

Figure. 4.14: Calorimetric and thermogravimetric charts of Fe–Cu-0% MWCNTs (120 min).

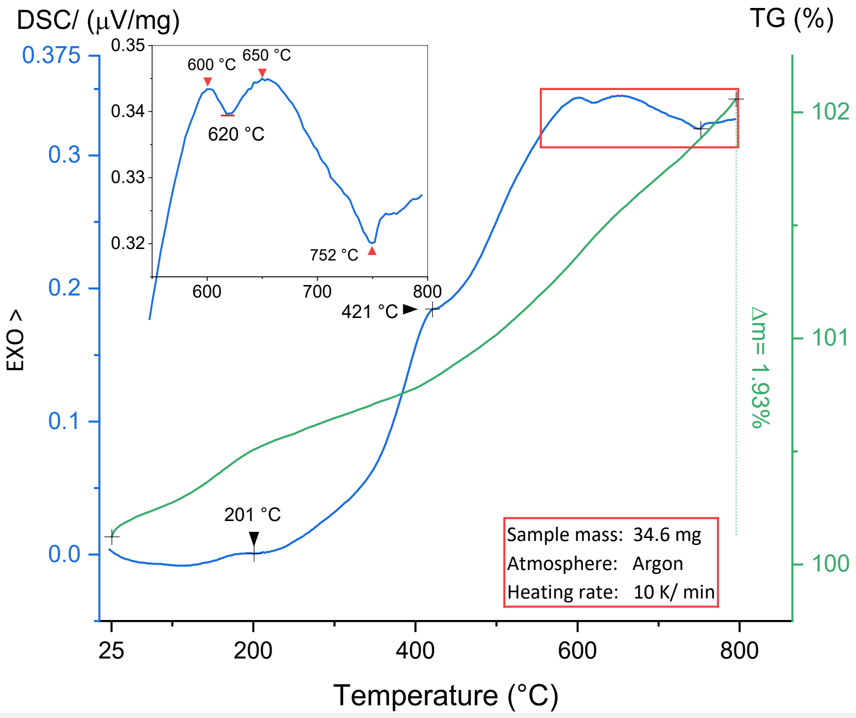

Figure. 4.15: Calorimetric and thermogravimetric charts of Fe–Cu-0.5% MWCNTs (120 min)

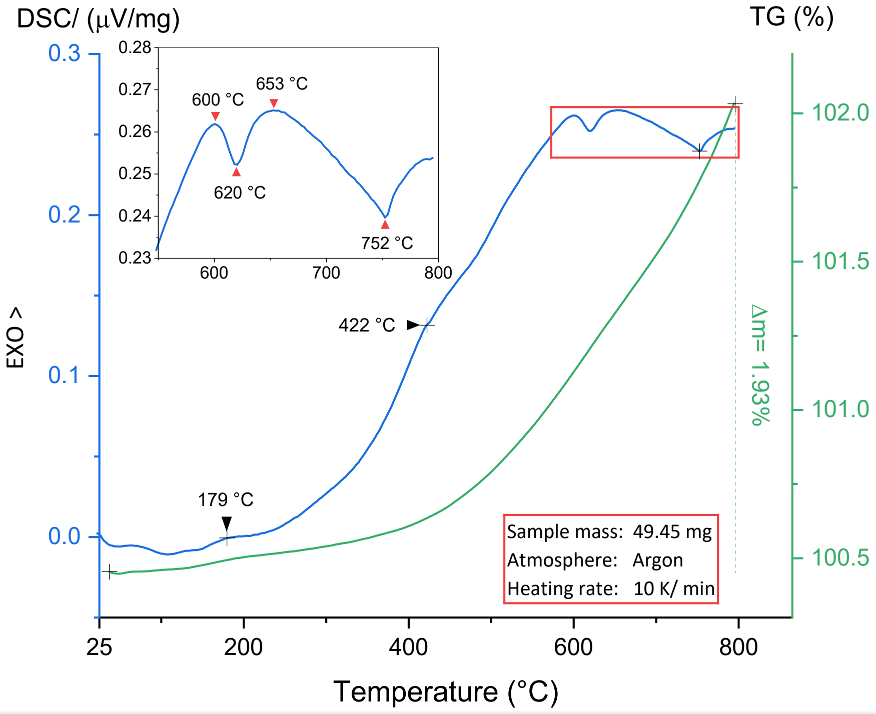

Figure. 4.16: Calorimetric and thermogravimetric charts of Fe–Cu-1% MWCNTs (120 min).

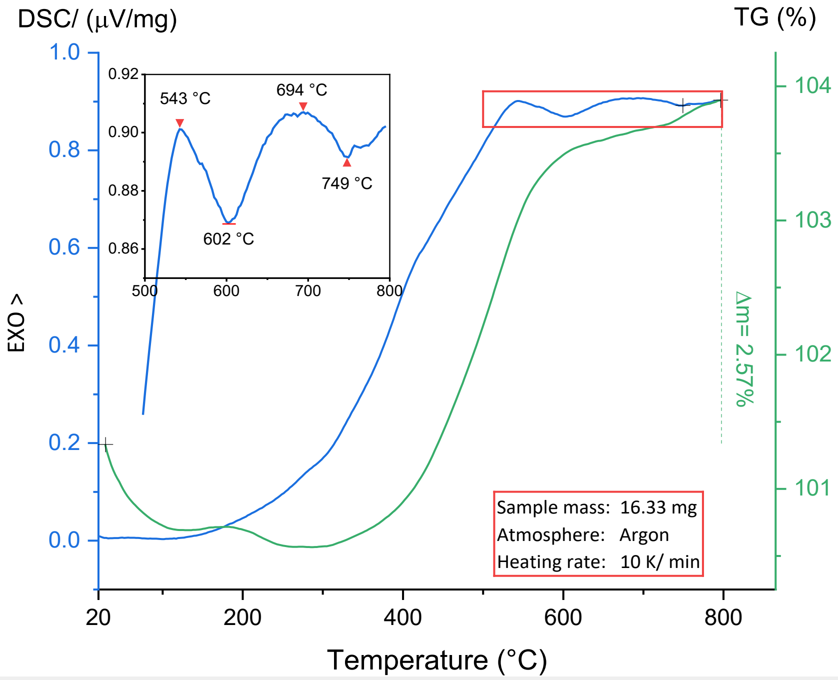

Figure. 4.17: Calorimetric and thermogravimetric charts of Fe–Cu-2% MWCNTs (120 min).

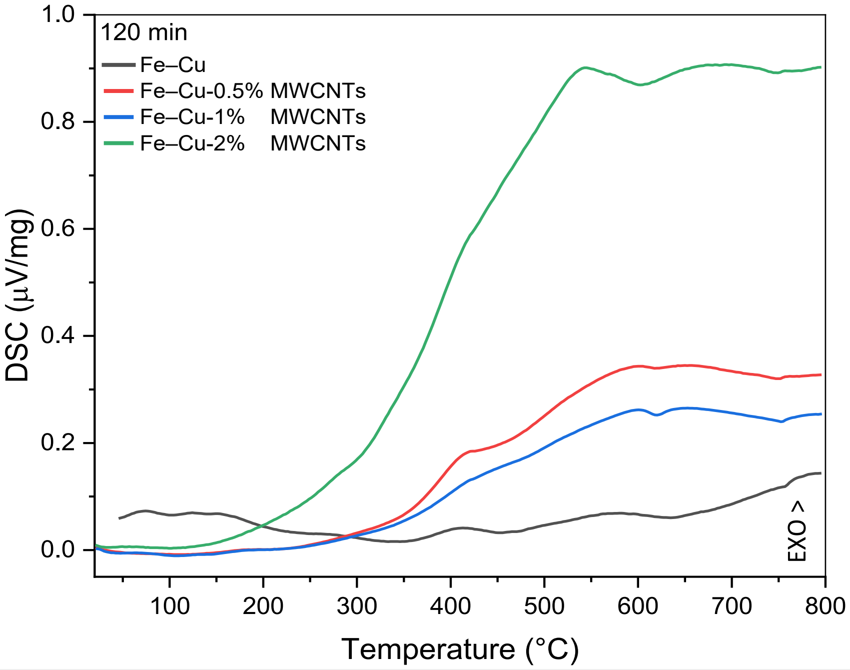

Figure. 4.18: DSC chart of Fe–Cu-X% MWCNTs (120 min).

Figure 4.18 shows the calorimetric measurements corresponding to the Fe–Cu-X% MWCNTs with 120 minutes milling time. The Fe–Cu sample is nearly stable along with the temperature range with minor fluctuations becoming noticeable at a small scale as shown in figure 4.14. As for the 0.5% MWCNTs sample, it shows a climbing value with rising temperature to surpass the 1% MWCNTs around temperature mark of 300 °C, on the other hand, the 2% MWCNTs shows higher calorimetric values of orders of magnitude compared to the last two, with an anomaly, an endothermic event at around 600 °C for all the samples containing CNTs.

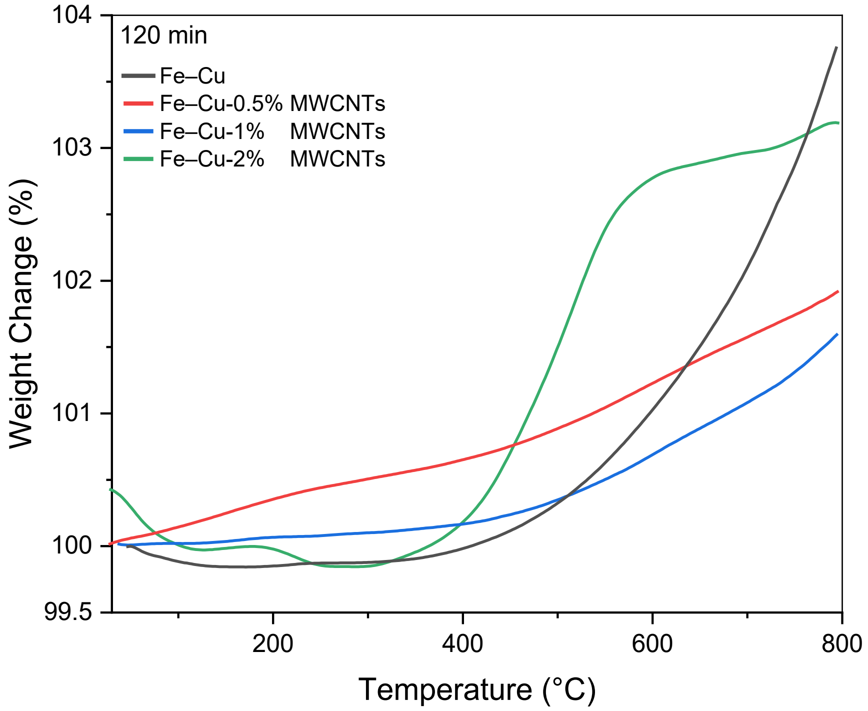

Figure. 4.19: Weight change chart of Fe–Cu-X% MWCNTs (120 min).

Figure 4.19 presents the thermogravimetric results of the Fe–Cu-X% MWCNTs nanocomposites for a 120 minutes milling time. The overall oxidation behaviour is dominant, with different oxidation degrees depending on the concentration of the MWCNTs, optimal thermal stability favouring the Fe–Cu with 1% MWCNTs at high temperature followed by the 0.5% and 2% MWCNTs respectively. The rate of change (oxidation) in the sample with 2% MWCNTs is increasing sharply at around 400 °C, to slow down at 540 °C possibly temperature reaches an activation threshold (thermal agitation) for CNTs.

IV.1.2 The relative linear expansion $\Delta L/L_0$ and the coefficient of thermal expansion (CTE) α(T) (Dilatometry)

The next figures present the relative linear expansion ($\Delta L/L_0$) and the CTE α(T) of the Fe–Cu nanocomposite milled for 20-, 60- and 120-minutes time with the addition of 0%, 0.5%, 1% and 2% vol of MWCNTs.

IV.1.2.1. 20 minutes milling time

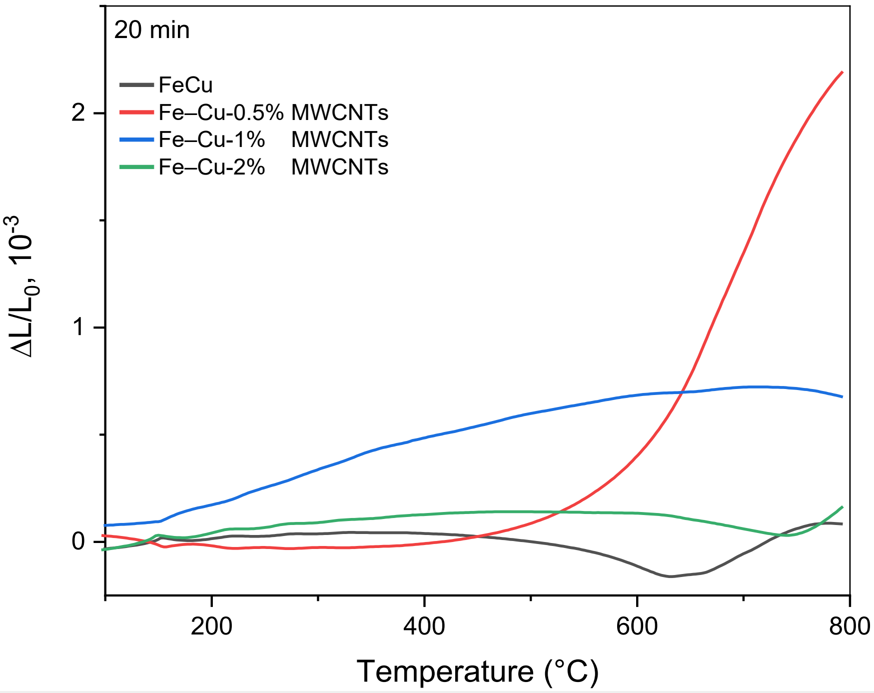

Figure. 4.20: Relative expansion of Fe–Cu-X% MWCNTs (20 min).

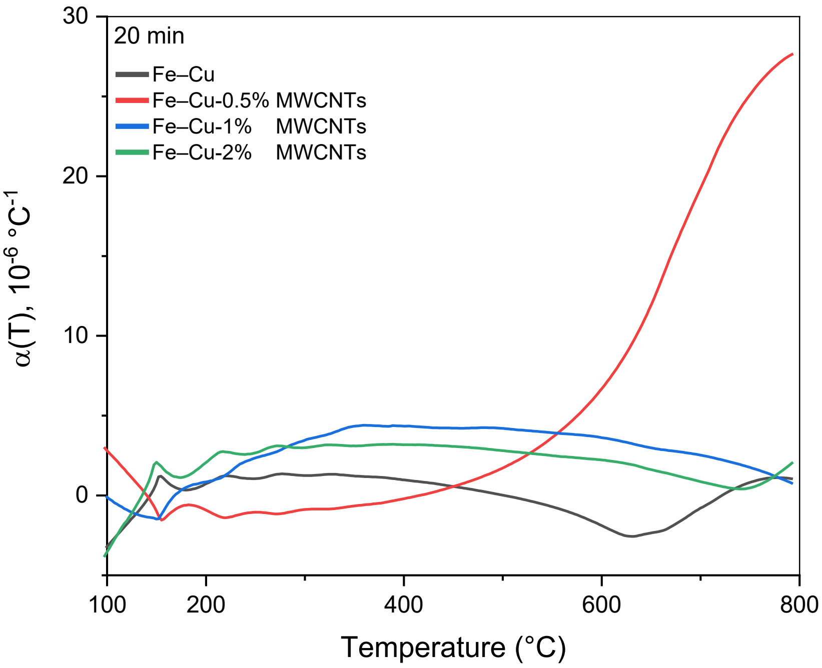

Figure. 4.21: Coefficient of thermal expansion of Fe–Cu-X% MWCNTs (20 min).

Figures 4.20 and 4.21 represent the dimensional variations $\Delta L/L_0$ and coefficient of thermal expansion (CTE) of the iron-copper nanocomposites with various amounts of MWCNTs, respectively.

Both 0.5% and 2% MWCNTs addition, have a small relative variation compared to that of 1% MWCNTs up to 500 °C. The sample with the least addition of MWCNTs sees a gradual increase within 200–600 °C. Probably, the small amount of nanofillers reinforcement acquires intense energy favouring the transformation of the α phase by shifting toward high temperature.

As for the Coefficient of thermal expansion (CTE), its behaviour depends on the temperature, the temperature range can be divided into two intervals. The first one, from ambient to around 500 °C, all charts have the same shape with some overlapping. The possibility of thermal agitation is insufficient to reveal the role of different concentrations of MWCNTs introduced. When the heating became important, the thermal agitation strongly disperse the smaller amount of MWCNTs and thus displaces the anomaly corresponding to the transition in iron. As for the Fe–Cu samples with 1% and 2% MWCNTs addition, they have near identical behaviour with overlapping at high temperatures. This may imply the homogeneous dispersion of MWCNTs knowing that the I_D/I_G ratio (see Raman) shows that the two samples had a slight deterioration of the MWCNTs, which give us an estimation that they contained the same amounts of defects.

IV.1.2.2. 60 minutes milling time

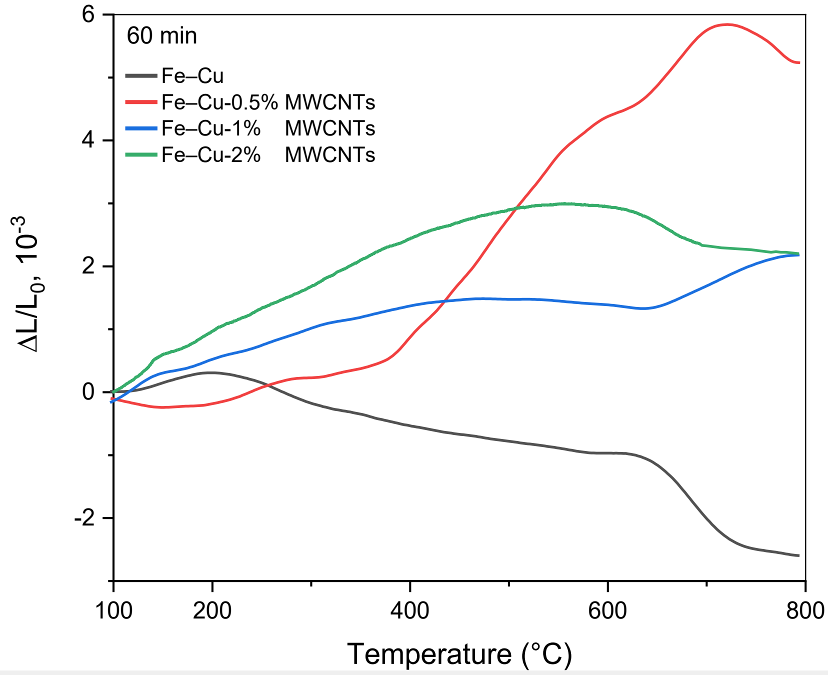

Figure. 4.22: Relative expansion of Fe–Cu-X% MWCNTs (60 min).

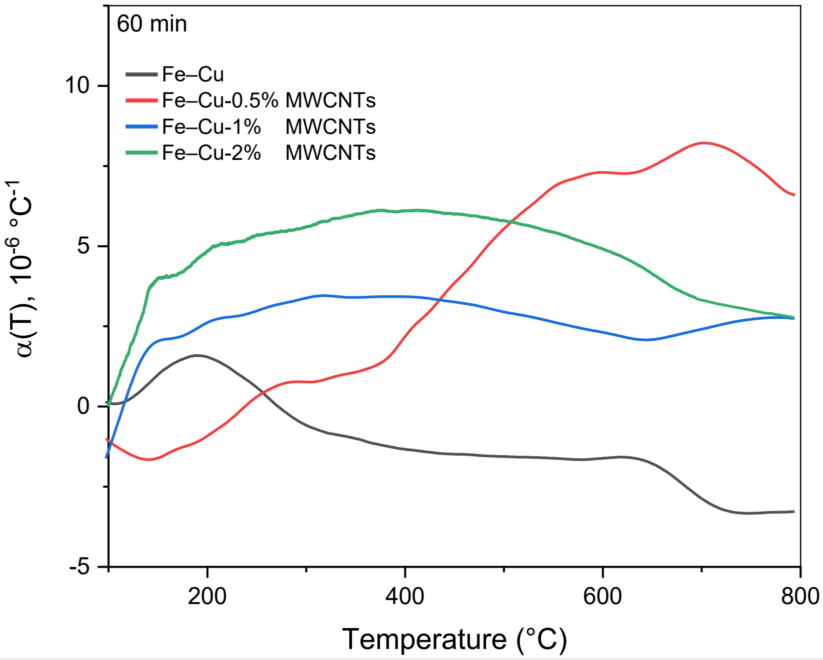

Figure. 4.23: Coefficient of thermal expansion of Fe–Cu-X% MWCNTs (60 min).

As for the 60-minute milling time samples, the dimensional behaviour changes. There are two distinct areas. From ambient to around 440 °C, $\Delta L/L_0$ of Fe–Cu-0.5% MWCNTs is lower than the other two samples with MWCNTs concentrations. Above 440 °C, the roles are reversed. The dimensional variation $\Delta L/L_0$ of the 0.5% MWCNTs is rising with temperature to reach two times the order of magnitude compared to the 1% and 2% MWCNTs. The phase appears to be late compared to the other two. At high temperatures, the thermal agitation is strong implying intense mobility of the MWCNTs which probably implies a delay in the transition of the α phase. An interesting remark concerns the approximation of the ΔL/L and becomes equal to 800 °C. This may mean that the intense mobility of MWCNTs may be related to the uniqueness of the mechanism of interaction.

Meanwhile, the CTE variations for the samples of the 60-minute milling time, shows that both 1% and 2%MWCNTs additions have the same oval shape with a slight increase from ambient temperature till mid rang of around 450 °C, then a slight decrease in the vicinity of 650 °C, both values of CTE intersect at the end of the range near 800 °C. On the other hand, for the CTE corresponding to 0.5% MWCNTs is lower compared to the 1% and 2%MWNCTs concentrations from ambient till 430 °C, above that it becomes higher possibly due to the transition to the α phase.

As for the 1% MWCNTs, it is lower than that of 2% MWCNTs. Perhaps due to the good dispersion of MWNCTs in the 1% MWCNTs sample, leading to an amplification of the interatomic bonding between the host matrix and the incorporated CNTs. In the vicinity of 800 °C, the CTE of both 1% and 2% MWCNTs intersect. This situation is due to the strong thermal agitation causing a homogeneous dispersion of the MWCNTs.

IV.1.2.3. 120 minutes milling time

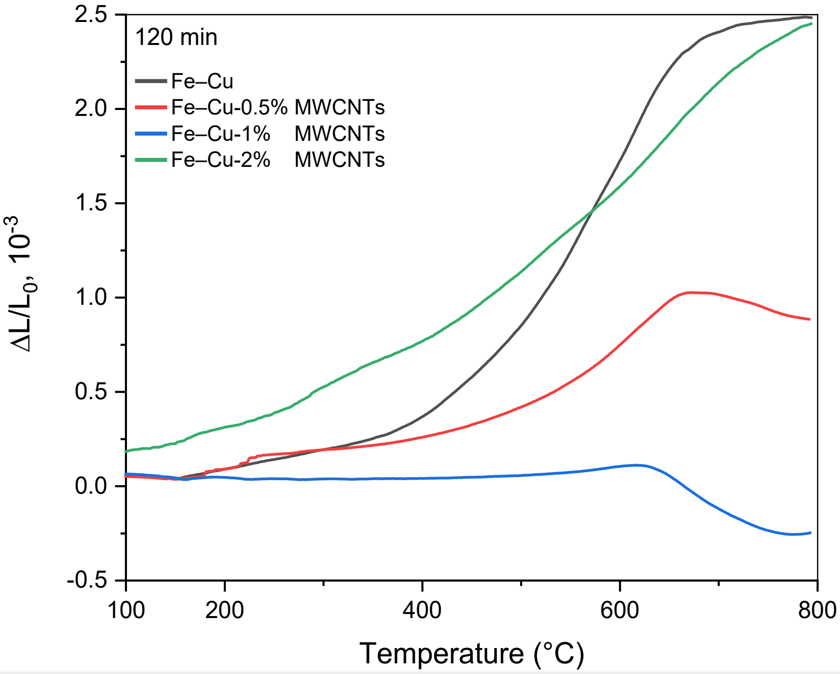

Figure. 4.24: Relative expansion of Fe–Cu-X% MWCNTs (120 min).

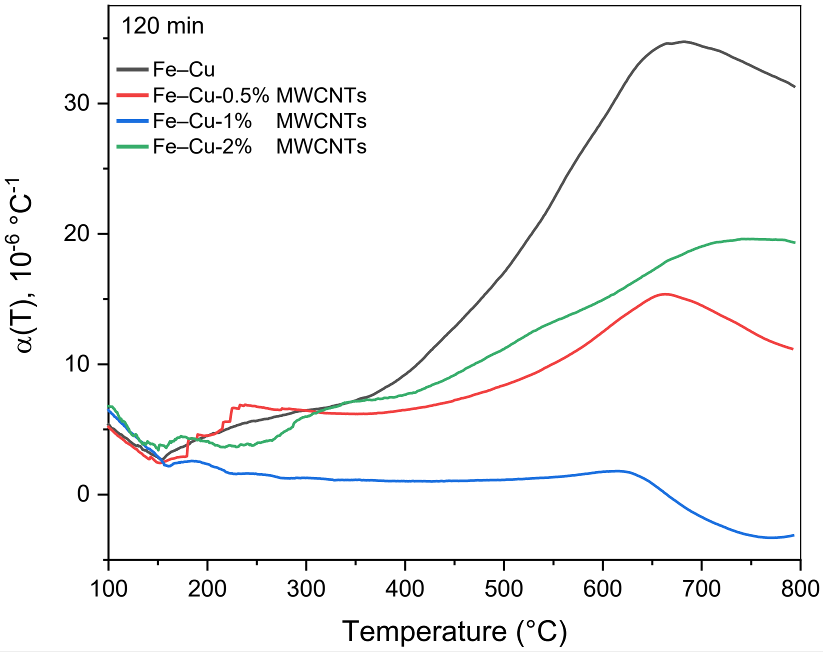

Figure. 4.25: Coefficient of thermal expansion of Fe–Cu-X% MWCNTs (120 min).

Now, as for the Fe–Cu-X% MWCNTs with 120-minute milling time; the relative linear expansion $\Delta L/L_0$ of the three curves (0%, 0.5% and 2%) mainly have similar behaviour over the entire temperature range which increases accordingly with elevating temperature. A presence of an anomaly is located around 620 °C.

The sample containing 2% MWCNTs is over both 0.5% and 1% MWCNTs for the whole interval. At 800 °C, a very noticeable difference in $\Delta L/L_0$ values between 2% and 0.5% MWCNTs compared to the 1% MWCNTs. This large difference can be linked to the difference in concentration of the incorporated carbon nanofillers. The charts presenting the CTE measurements show the same behaviour. Each curve displayed a peak indicating the α phase appearing in the vicinity of 620 °C. On the other hand, its intensity depends on the amount of the reinforcing element introduced. The CTE behaviour of the Fe–Cu-1% MWCNTs nanocomposite is significantly lower than the other two over the entire temperature range. Certainly, this concentration is well-dispersed giving a rise to a significant amount of bonding which translates into a force.

A comparative study on the role of milling time shows that the coefficient of thermal expansion of the 60-minutes milling time is the lowest. This time led to curves with behaviour less intense, practically linear and uniform. Probably the milling time is sufficient to give good dispersion of the MWCNTs. Which will prevent the agglomeration and bundling of the CNTs into clusters, which are responsible for the deterioration of the sample qualities. The characteristic anomalies of the α phase have very low intensities. At high temperatures, the intersection of the curves implies that the interactions are the same and the bond strength is of the same order of magnitude. This is in agreement with the calorimetric behaviour of these samples. They have the same calorific value at high temperatures, which proves that MWCNTs play the same role and are responsible for the stability of nanomaterials.

The interesting result obtained concerns the drop in the coefficient of expansion whatever the concentration or the milling time. The CTE of all nanocomposites is very low. It does not exceed 6.10^{-6} °C^{-1}. It is about the coefficient of expansion of the nanotubes themselves. This drastic decrease in CTE can have different origins. Oxide formation plays a protective role. It envelops the matrix and prevents its contribution to expansion. The interaction becomes M-O-MWCNTs type instead of M-MWCNTs. Without forgetting the formation of carbides which can also block the elongation of the matrix which are important phases in the reinforcement of the matrix-MWCNTs, in addition, they promote the stability of the grain size. We note that the two phases also have very low expansion coefficients.

IV.2 Structural analysis

IV.2.1 X-ray diffraction

X-ray diffraction (XRD) patterns were recorded to analyse the phase and crystal structure of the iron-copper nanocomposites with the addition of multiwalled carbon nanotubes concentrations 0, 0.5, 1 and 2%.vol respectively. The "Philips X Pert pro" was used, operated at a step scan size of 0.026° in the range of [20–80°] and with Cu K_α radiation ($\lambda = 1.5406$ Å, 40 kV voltage, 40 mA current), the X-ray patterns were analysed using X'Pert HighScore with the latest JCPDs database.

IV.2.1.1 Multiwalled carbon nanotubes

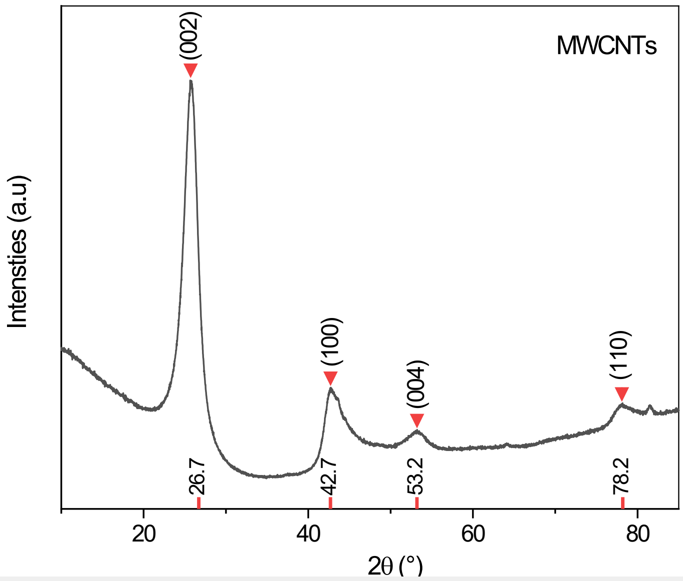

Figure. 4.26: XRD patterns of MWCNTs.

The wide-angle XRD pattern of randomly oriented MWCNTs used as nanofillers in the studied Fe–Cu nanocomposite is shown in Figure 4.26. The pattern displayed an intense large peak at $2\theta = 26.7°$, followed by relatively intense diffraction peaks around 42.7°, 53.2° and 78.2° can be assigned to the corresponding (002), (100), (004) and (110) reflections plane of the highly ordered graphitic structure of carbon. This result indicates that MWCNTs are well graphitized. [262,263] The absence of carbonaceous impurities was observed from the XRD pattern.

IV.2.1.2. 20 minutes milling time

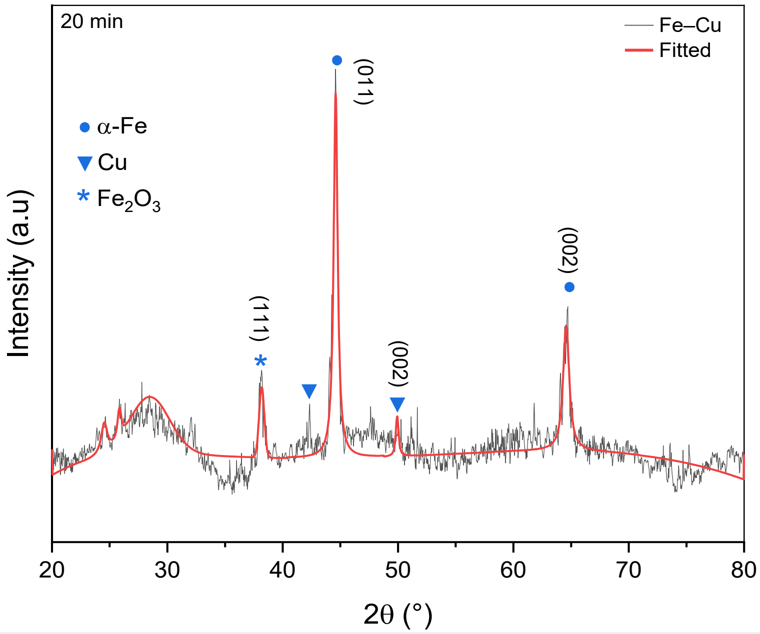

Figure. 4.27: XRD patterns of Fe–Cu without MWCNTs (20 min).

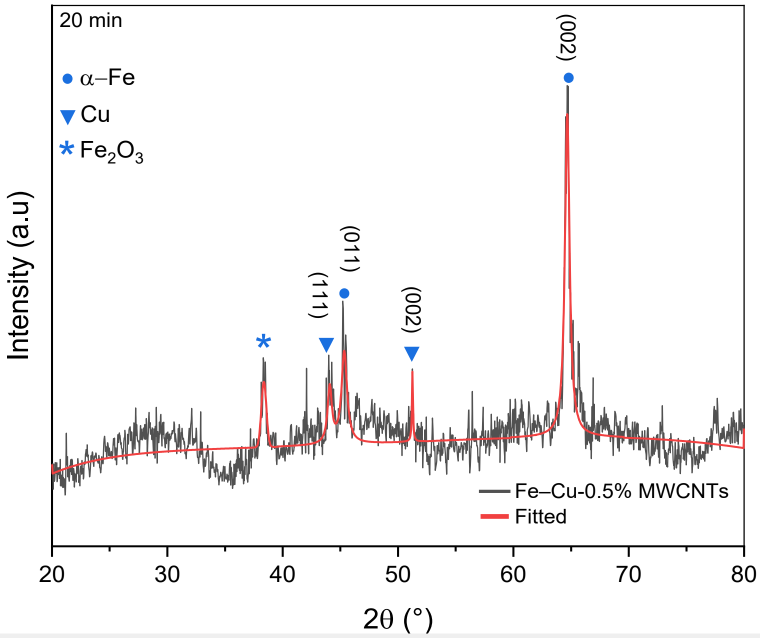

Figure. 4.28: XRD patterns of Fe–Cu-0.5% MWCNTs (20 min).

.

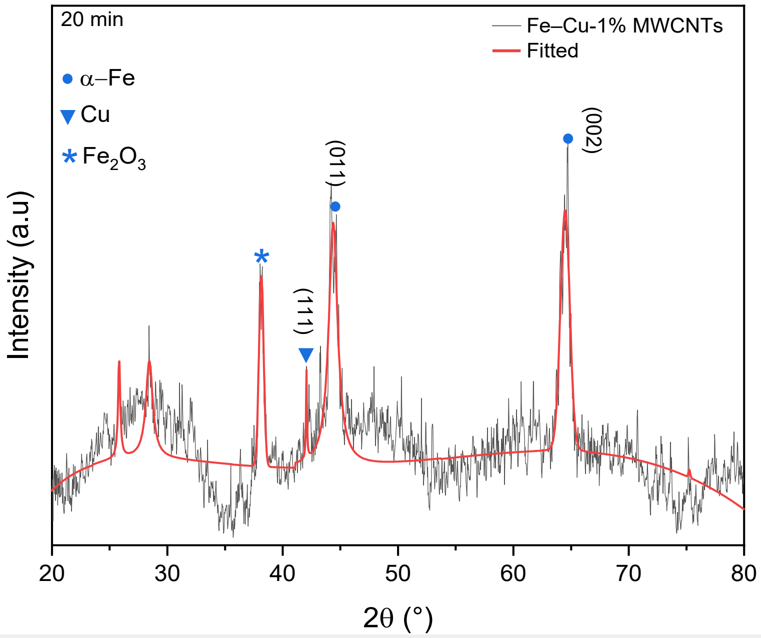

Figure. 4.29: XRD patterns of Fe–Cu-1% MWCNTs (20 min).

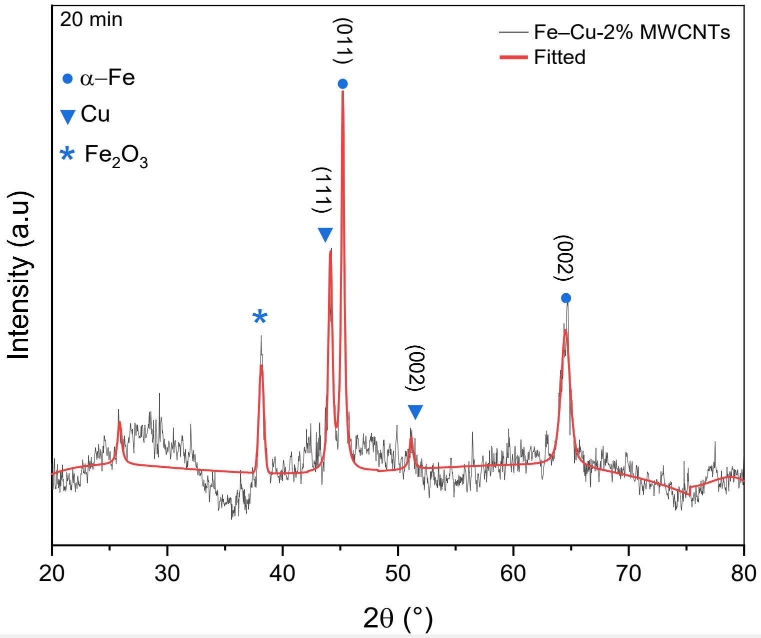

Figure. 4.30: XRD patterns of Fe–Cu-2% MWCNTs (20 min).

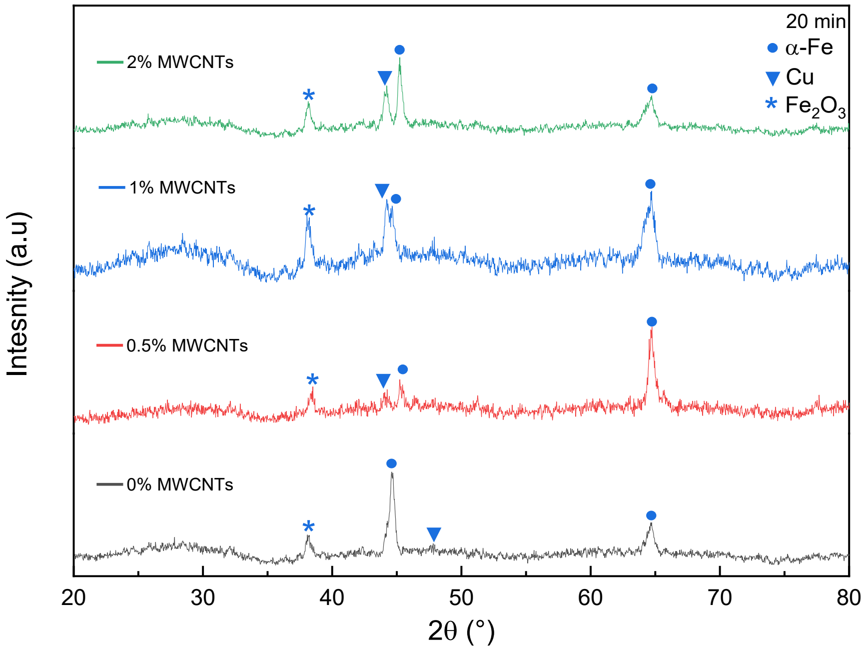

Figure. 4.31: XRD patterns of Fe–Cu with 0.5%, 1% and 2% MWCNTs (20 min).

Figure 4.31 reveal XRD diffractogram patterns of Fe–Cu nanocomposite milled for 20 minutes, the presences of the phases correspond to the body-centred cubic (bcc)-iron crystal and face-centred cubic (fcc)-copper crystal with relative intensities across the board for all samples with their respected reflection planes and 2θ are described in **table 4.1**. Most of the peaks are shifted toward a lower angle. The presence of iron oxide peak at around 2θ=38°.

The average grain size increases accordingly with the increasing amount of MWCNTs.

Table 4.1: The XRD pattern data of the Fe–Cu-X% MWCNTs milled for 20 minutes. (The position of the peaks, relative intensities, FWHM (full width at half maximum), miller indexes, crystallite average size, and JCPDs database reference codes.)

Fe–Cu-X%.vol MWCNTs	2θ (°)	Relative Intensity (%)	(hkl)	FWHM (2θ) (°)	Average grain size (nm)	Reference (JCPDs)
0%	24.22	7.40		2.1	19	-
	25.84	10.05		0.115		-
	28.41	12.97		4.74		-
	32.08	9.69		0.41		-
	38.17	23.10		0.544		-
	44.59	100	(011)	0.462		-
	48.11	11.60		3.34		-
	64.57	34.75		0.676		-
0.5%	38.37	20.20		0.528	20	-
	44.08	17.47	(113)	0.410		-
	45.34	28.47		0.610		-
	51.25	21.69		0.116		-
	64.67	100		0.494		-
1%	26.10	40.01		0.200	26	-
	28.10	39.76		1.200		-
	38.1	77.82		0.100		-
	42.12	36.48	(111)	0.200		-
	44.43	100	(110)	1.300		-
	64.52	98.58		1.300		-
	75.10	3.17		0.100		-
2%	26.56	11.42		0.116	30	-
	38.19	28.52		1.671		-
	44.20	56.74	(111)	0.320		-
	45.45	100	(011)	0.253		-
	51.17	8.53		0.128		-
	65.16	36.29		1.264		-

IV.2.1.3. 60 minutes milling time

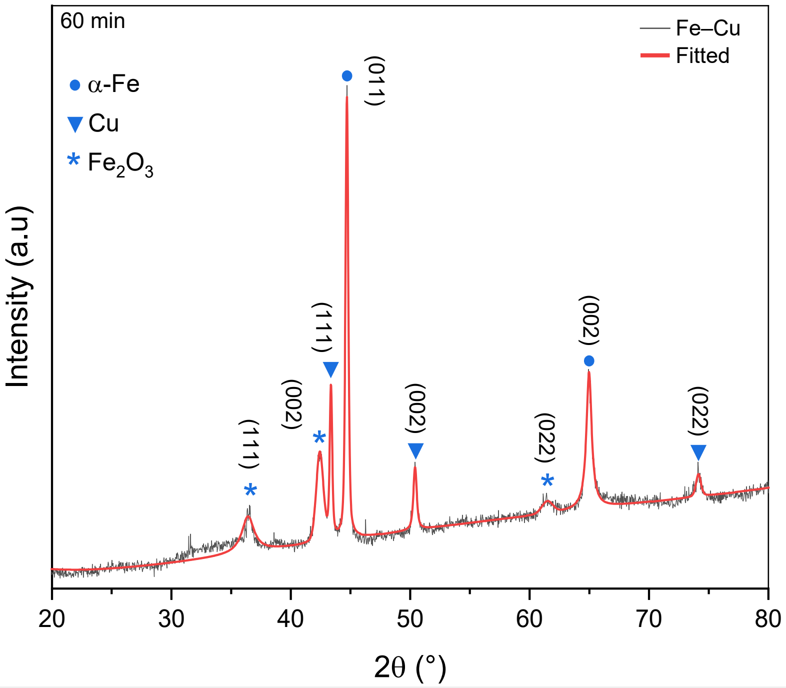

Figure. 4.32: XRD patterns of Fe–Cu without MWCNTs (60 min).

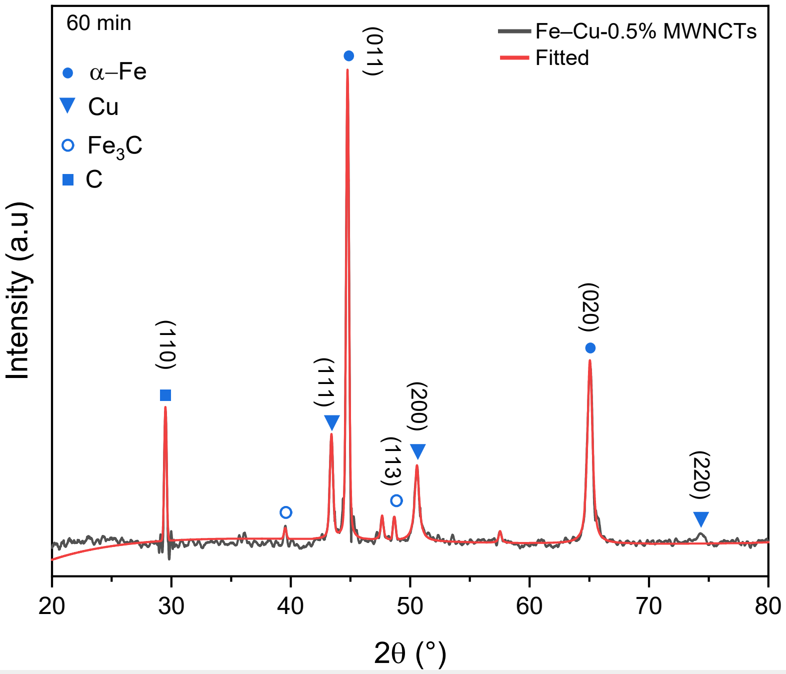

Figure. 4.33: XRD patterns of Fe–Cu-0.5% MWCNTs (60 min).

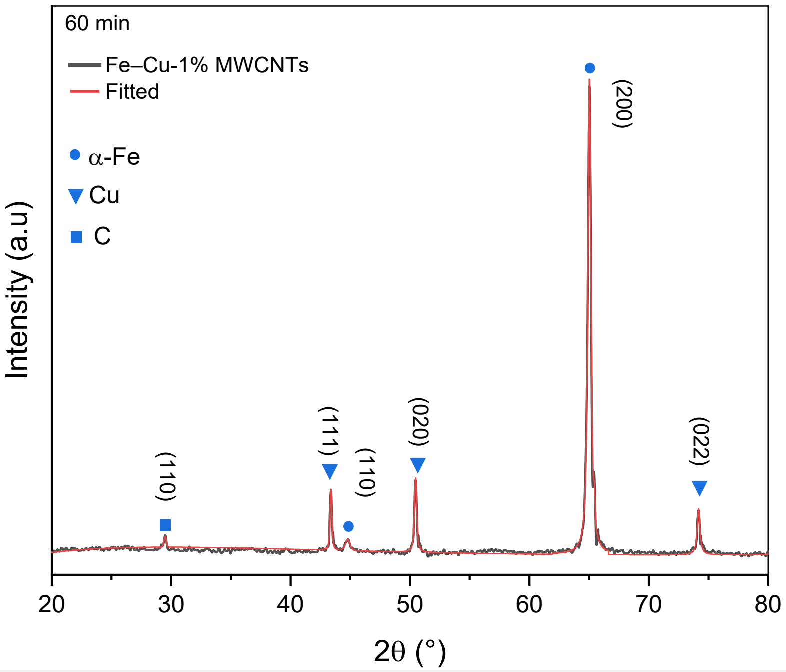

Figure. 4.34: XRD patterns of Fe–Cu-1% MWCNTs (60 min).

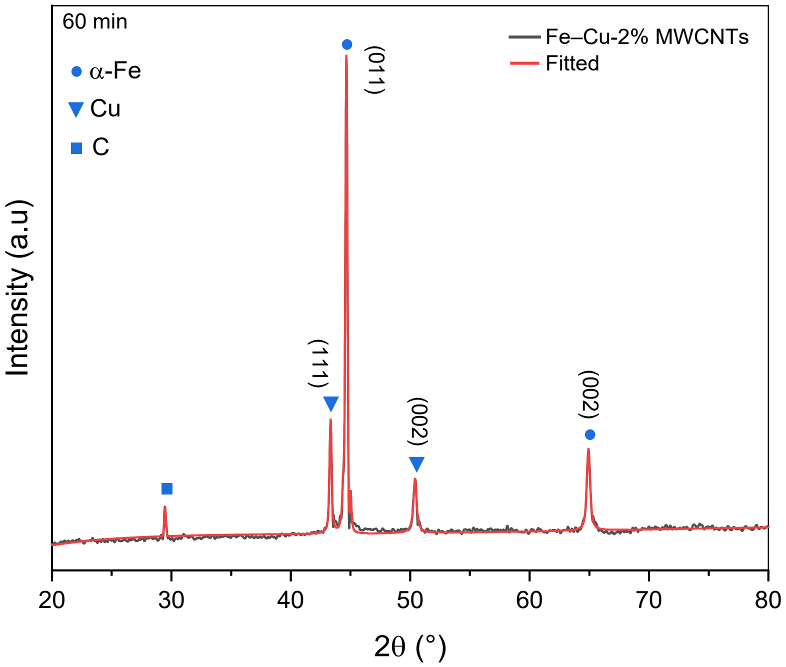

Figure. 4.35: XRD patterns of Fe–Cu-2% MWCNTs (60 min).

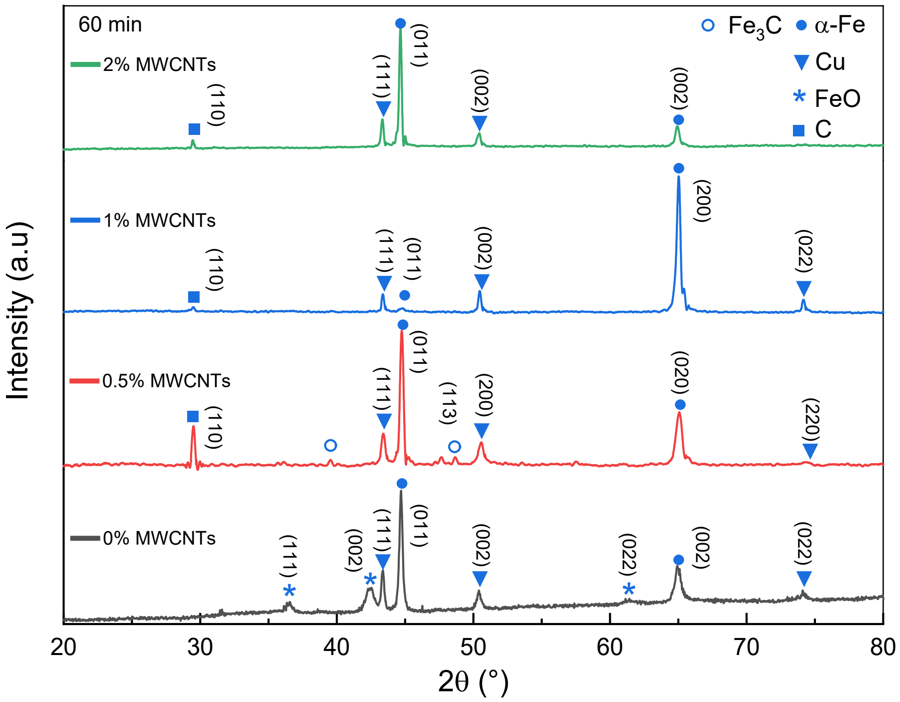

Figure. 4.36: XRD patterns of Fe–Cu with 0.5%, 1% and 2% MWCNTs (60 min).

Figure 4.36 presents XRD diffractogram patterns of Fe–Cu nanocomposite milled for 60 minutes, the presences of the phases correspond to the body-centred cubic (bcc)-iron crystal and face-centred cubic (fcc)-copper crystal with relative intensities across the board for all samples with their respected reflection planes and 2θ are described in **table 4.2** below.

A presence of iron oxide only in the samples Fe–Cu without any MWCNTs, while the samples containing different concentrations of MWCNTs have the same planes corresponding to iron and copper, except for the 1% MWCNTs favouring the plane (200). The presence of carbide in samples containing MWCNTs is immanent, but it recorded only in the samples 0.5% MWCNTs, also a trace of carbon in 1% and 2% MWCNTs and most notable in 0.5% MWCNTs. As for the grain size, the effect of concentrations appeared at a high concentration of 2% MWCNTs.

Table 4.2: The XRD pattern data of the Fe–Cu-X% MWCNTs milled for 60 minutes. (The position of the peaks, relative intensities, FWHM (full width at half maximum), miller indexes, crystallite average size, and JCPDs database reference codes.)

Fe–Cu-X%.vol MWCNTs	2θ (°)	Relative Intensity (%)	(hkl)	FWHM (2θ) (°)	Average grain size (nm)	Reference (JCPDs)
0%	36.40	8.39	(003)	1.437	33	96-231-1021
	42.43	20.60	(10-2)	0.692		96-231-1021
	43.36	33.87	(111)	0.244		96-710-1265
	44.70	100	(011)	0.278		96-411-3937
	50.41	14.36	(020)	0.342		96-710-1265
	64.98	30.83	(020)	0.532		96-411-3937
	74.14	5.17	(022)	0.457		96-710-1265
0.5%	29.50	28.51	(110)	0.231	30	01-072-2091
	43.40	22.16	(111)	0.322		03-065-9743
	44.75	100	(011)	0.281		96-500-0218
	48.67	4.86	(113)	0.267		96-101-0932
	50.56	16.19	(200)	0.445		03-065-9743
	65.05	39.08	(020)	0.512		96-500-0218
	74.59	2.52	(220)	0.09		03-065-9743
1%	29.48	2.19	(110)	0.310	34.56	01-072-2091
	43.38	12.83	(111)	0.202		96-901-3015
	44.77	2.30	(110)	0.410		00-003-1050
	50.46	15.69	(020)	0.232		96-901-3015
	65.02	100	(200)	0.306		00-006-0696
	74.17	9.82	(022)	0.253		96-901-3015
2%	29.47	6.21	(110)	0.172	43.5	01-072-2091
	43.34	24.45	(111)	0.211		01-070-3039
	44.66	100	(011)	0.203		96-901-3473
	50.40	11.69	(002)	0.313		96-901-3015
	64.93	17.60	(020)	0.332		96-901-3473

IV.2.1.4. 120 minutes milling time

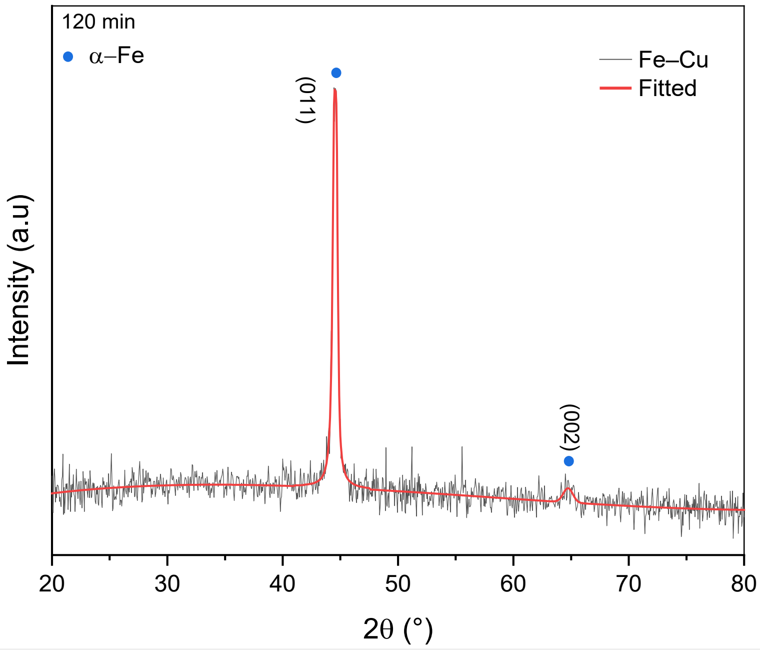

Figure. 4.37: XRD patterns of Fe–Cu without MWCNTs (120 min).

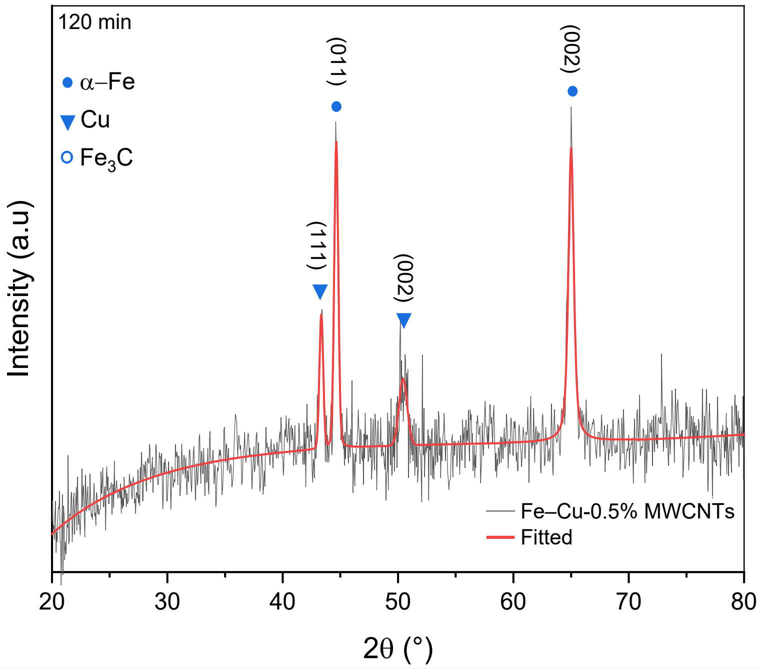

Figure. 4.38: XRD patterns of Fe–Cu-0.5% MWCNTs (120 min).

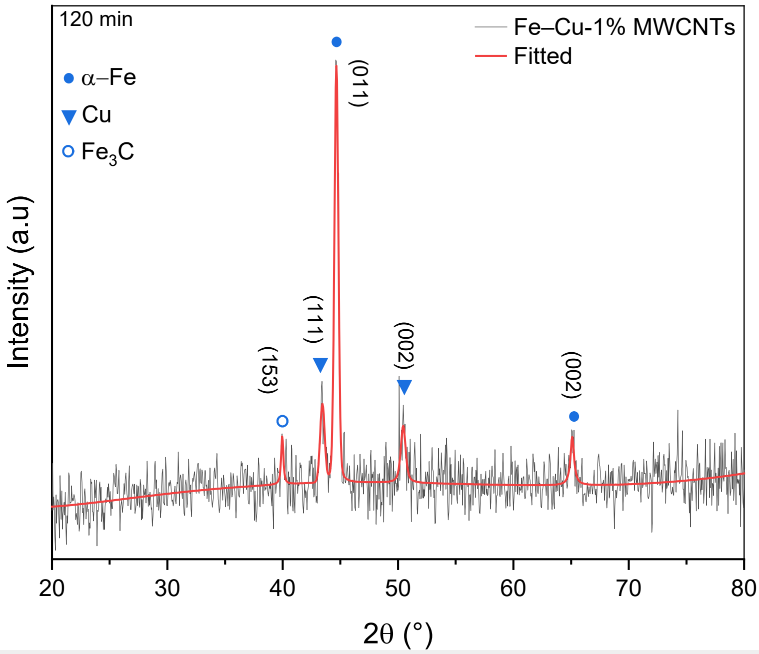

Figure. 4.39: XRD patterns of Fe–Cu-1% MWCNTs (120 min).

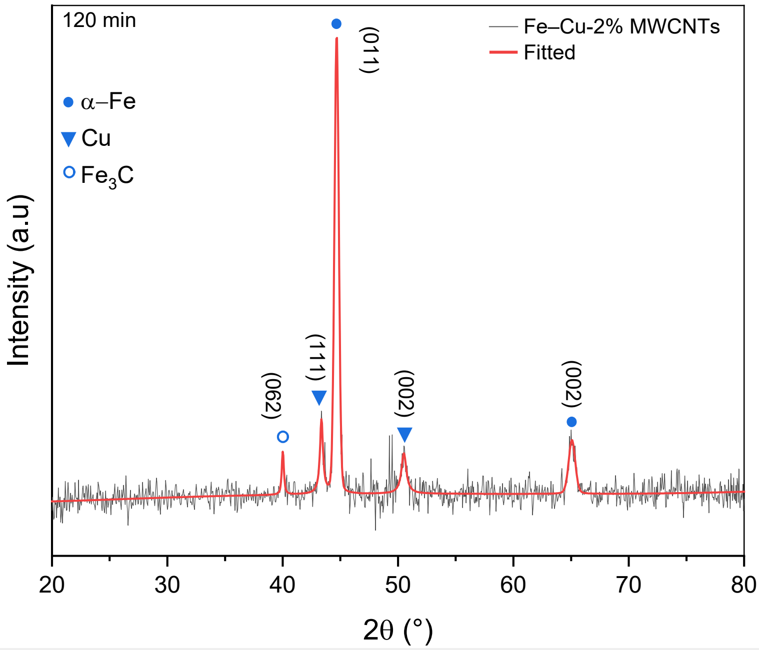

Figure. 4.40: XRD patterns of Fe–Cu-2% MWCNTs (120 min).

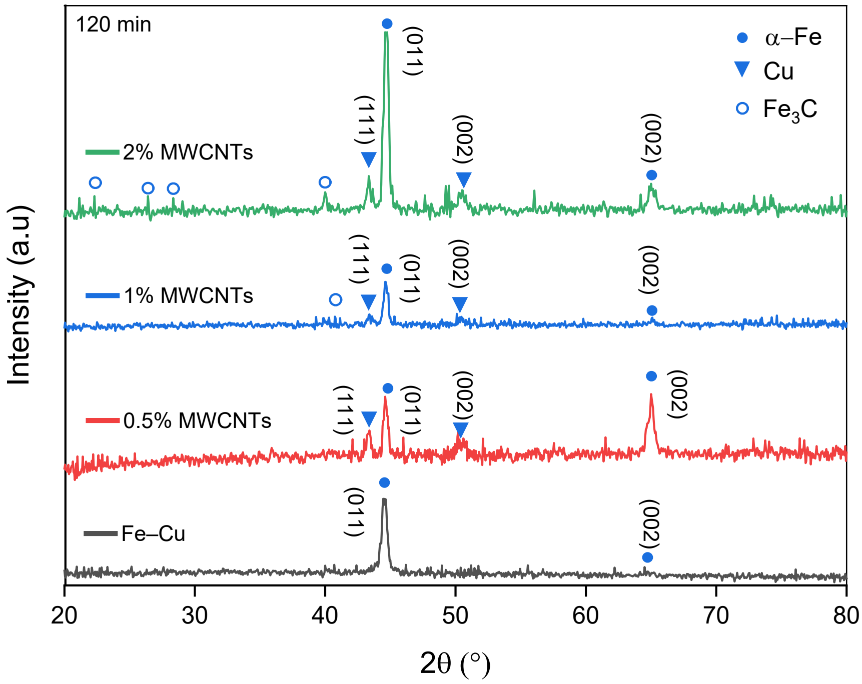

Figure. 4.41: XRD patterns of Fe–Cu with 0.5%, 1% and 2% MWCNTs (120 min).

Figure 4.41 shows XRD diffractogram patterns of Fe–Cu nanocomposite milled for 120 minutes, the presences of the phases correspond to the body-centred cubic (bcc)-iron crystal and face-centred cubic (fcc)-copper crystal with their respected reflection planes and 2q are described in table 4.3. A weak appearance for iron carbide presence between lower angles and 2q = 35° for samples containing 0.5%, 1% and 2% MWCNTs respectively. As for grain size, it averages around 21.5 nm and it doesn't differ from the Fe–Cu without MWCNTs. This grain size is somehow stable, this might be due to, (i) the pining effect, the formation of carbide on the boundaries between the CNTs and the hosting matrix hindering the grain growth. (ii) Grain refinemen.

Table 4.3: The XRD pattern data of the Fe–Cu-X% MWCNTs milled for a 120 min.

Fe–Cu-X%.vol MWCNTs	2θ (°)	Relative Intensity	(hkl)	FWHM (2θ)(°)	Average grain size (nm)	Reference (JCPDs)
0%	40.10	10.73		0.087	19	
	44.54	100	(011)	0.482		96-901-3474
	64.52	7.79		0.130		
0.5%	43.32	34.41	(111)	0.410	21.2	96-901-3015
	44.61	78.28	(011)	0.405		96-901-3473
	50.41	16.95	(020)	0.930		96-901-3015
	65	100	(020)	0.285		96-901-3473

1%	39.95	15.08	(153)	0.073	19	96-230-0662
	43.42	17.14	(111)	0.451		96-901-2955
	44.65	100	(011)	0.389		96-411-3937
	50.43	14.91	(020)	0.525		96-901-2955
	51.96	2.49	(134)	0.131		96-901-4244
	65.10	12.33	(020)	0.357		96-411-3937
	74.29	16.57	(022)	0.180		96-901-2955
2%	40.00	9.65	(062)	0.210	23	96-230-0662
	43.35	15.99	(111)	0.319		96-901-3015
	44.68	100	(011)	0.441		96-900-8537
	50.47	8.11	(020)	0.620		96-901-3015
	65.07	11.87	(020)	0.610		96-900-8537

For all milling times and regardless of concentration, the presence of a more or less background noise suggests the existence of an amorphous phase due to the sampling process, as observed by other authors during high-energy grinding [264-266]. The intensity of grinding at 50 g gives rise, in addition to amorphization, to out-of-equilibrium supersaturated phases. In [267], the authors identified several phases ranging from Fe (95) Cu (5) to Fe (83) Cu (17), such as the α(Fe, Cu) supersaturated Cu phase and ordered phases.

The formation of carbides due to the reaction between CNTs and the host matrix could adversely alter the mechanical properties. If the volume of carbide is high enough (usually >5%), a peak corresponding to the phase in the XRD is highly to occur. [268–270]

Depending on the degree of dispersion, CNTs play an intricate role in altering the grain size of the metal matrix. Due to the high thermal conductivity of dispersed CNTs, the metal matrix near isolated CNTs experiences a higher cooling rate, which results in fine grain size. On the contrary, CNTs clusters have very low thermal conductivity and could lead to grain growth near CNTs clusters [271,272]. CNT clusters also provide a pinning effect and resist grain growth. Hence, all these factors need to be kept in mind while computing matrix grain size from the Scherrer formula. The minimum grain size achievable by milling is determined by the competition between the plastic deformation via dislocation motion and the recovery and recrystallization behaviour of the material [273,274].

IV.2.2 Raman spectroscopy

The influence of the dispersion process on CNTs structure was evaluated by Raman spectroscopy. Through this technique, it is possible to analyse the defect ratio, and thus measure the damage induced by the dispersion technique. The ratio of the intensity of the D band (I_D) to the intensity of the G band (I_G) is used to evaluate the quality of the CNTs [275]. An increase in this ratio indicates a growth in the number of CNTs defects, whereas a decrease indicates a change in the structure of the CNTs.

Each Raman band was analysed by fitting with Breit-Wigner-Fano lines, Lorentzian lines.

The following figures represent the obtained Raman spectra of Fe–Cu containing different concentrations of MWCNTs ground for 20-, 60-, and 120-minutes time. Each curve contains, whatever the nanofiller amount and/or the processing time undergone by the samples.

IV.2.2.1 Multiwalled carbon nanotubes

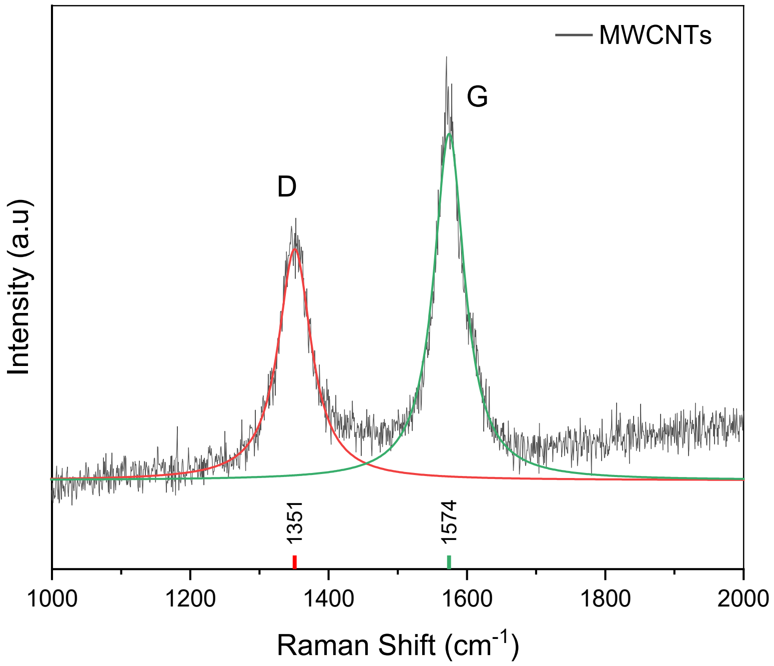

Figure. 4.42: Raman spectra of MWCNTs.

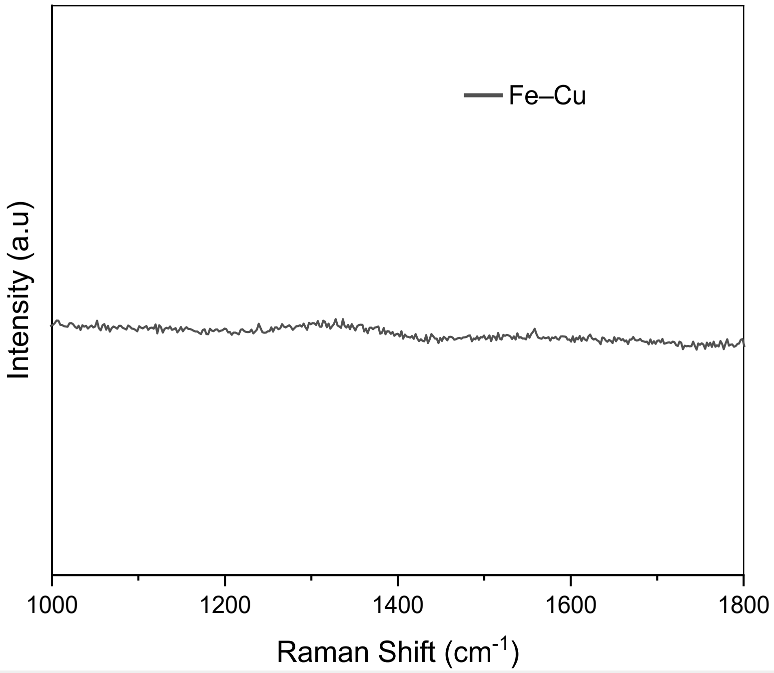

Figure. 4.43: Raman spectra of Fe–Cu without MWCNTs.

IV.2.2.2. 20 minutes milling time

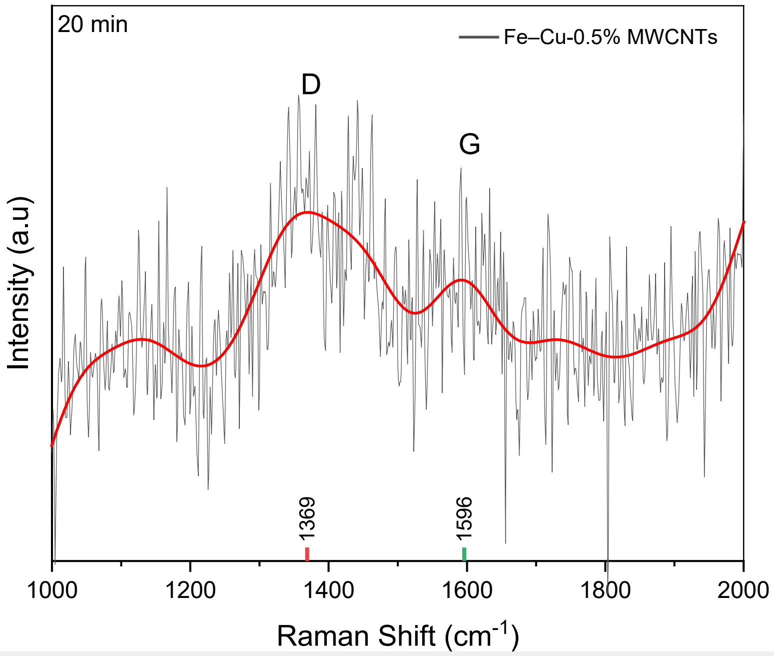

Figure. 4.44: Raman spectra of Fe–Cu-0.5% MWCNTs (20 min).

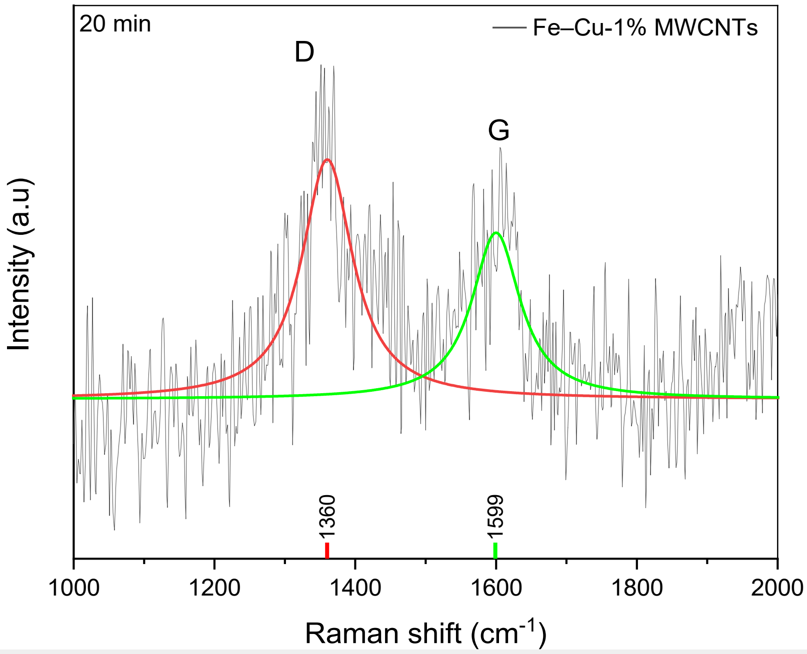

Figure. 4.45: Raman spectra of Fe–Cu-1% MWCNTs (20 min).

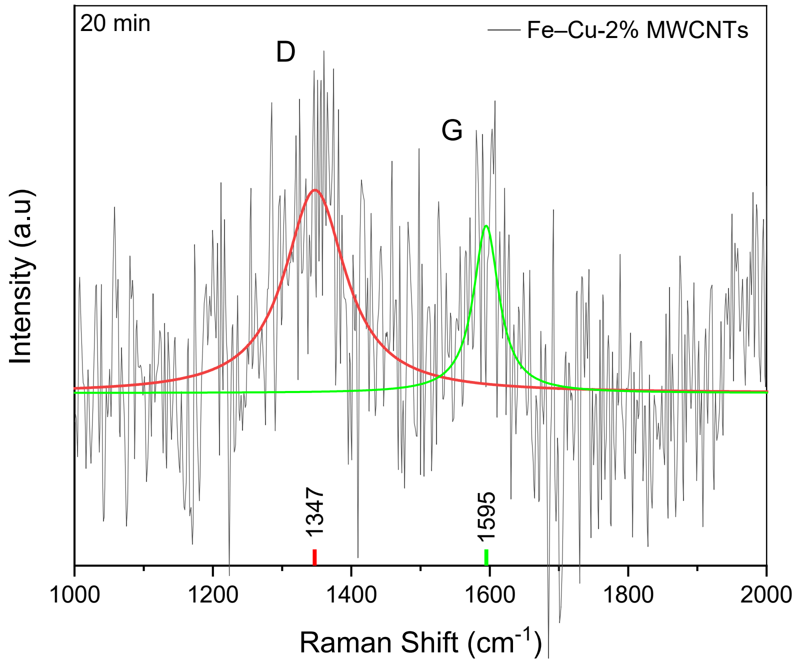

Figure. 4.46: Raman spectra of Fe–Cu-2% MWCNTs (20 min).

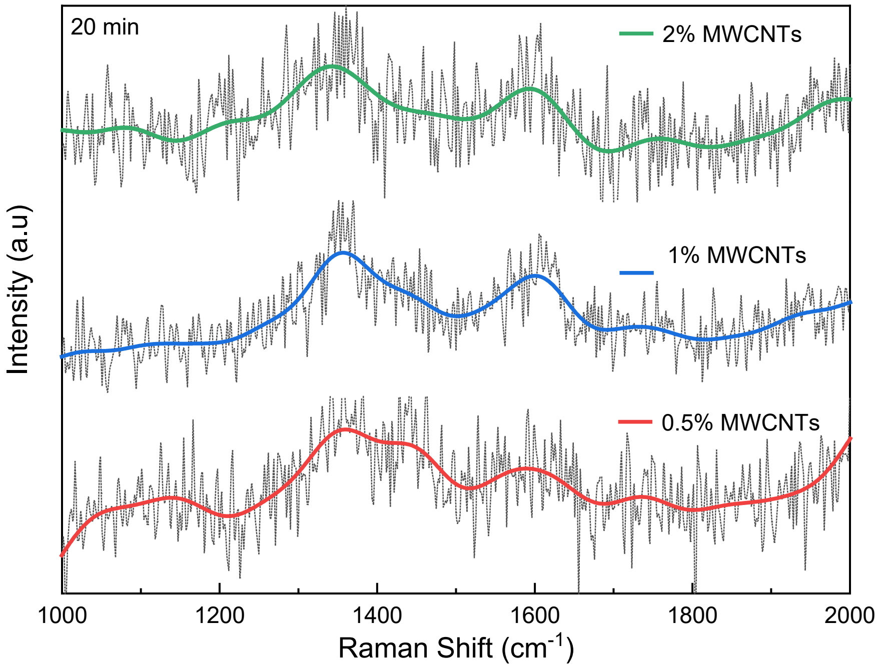

Figure. 4.47: Raman spectra of Fe–Cu-X% MWCNTs (20 min).

As shown in figure 4.47, the three curves contain the two characteristic peaks of carbon. Their shape and relative intensity change with concentration. The Fe–Cu-0.5% MWCNTs sample exhibits the D and G anomalies spread out in front of those of the other two.

Grinding at 20 minutes shows that the G peaks are less intense compared to the D peak regardless of the concentration. This induces a high I_D/I_G ratio, which means that the defect concentrations are high and the nanotubes undergo substantial deterioration. This can also lead to a probable alignment of the MWCNTs.

IV.2.2.3. 60 minutes milling time

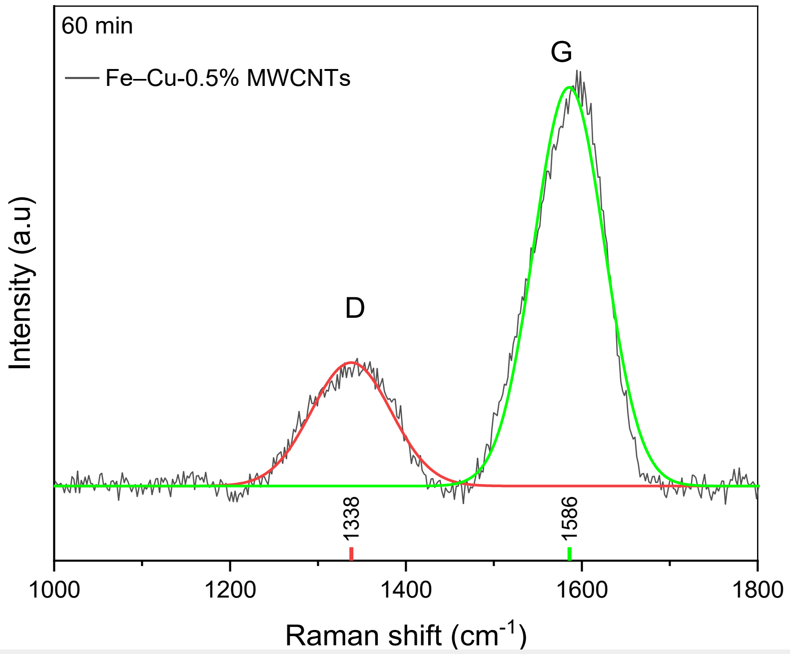

Figure. 4.48: Raman spectra of Fe–Cu-0.5% MWCNTs (60 min).

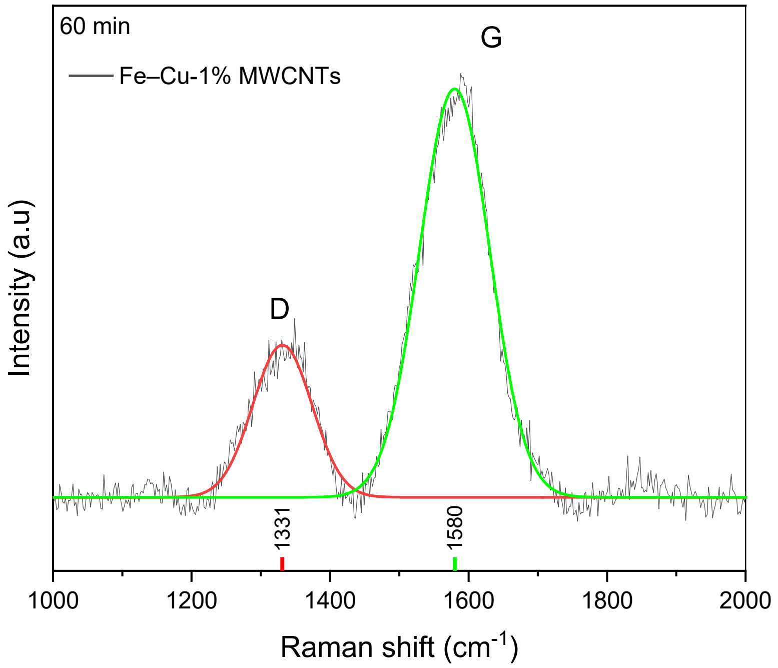

Figure. 4.49: Raman spectra of Fe–Cu-1% MWCNTs (60 min).

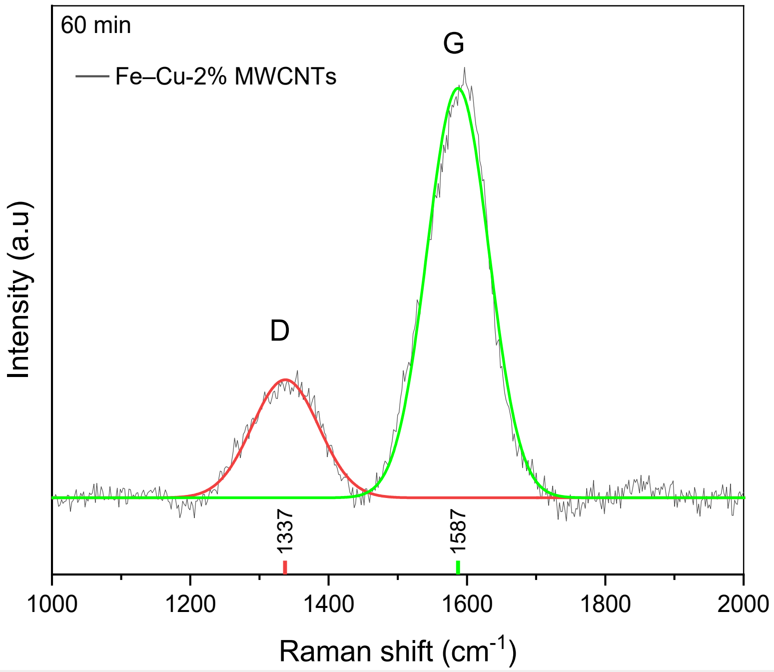

Figure. 4.50: Raman spectra of Fe–Cu-2% MWCNTs (60 min).

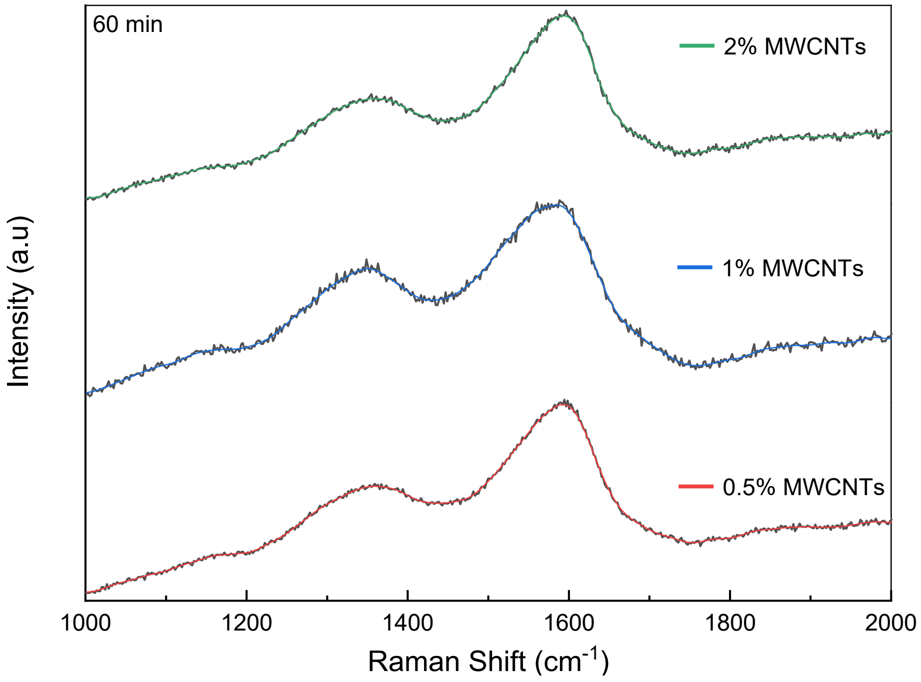

Figure. 4.51: Raman spectra of Fe–Cu-X% MWCNTs (60 min).

When the samples undergo longer mechanical processing, the situation is reversed compared to the 20 minutes milling time. The G peak has higher intensity compared to the D peak. Their relative intensity depends on the concentration of MWCNTs. This implies low I_D/I_G ratios indicating that defect rates have been reduced. This may mean that increasing the grinding time has minimized the number of defects and that MWCNTs have less deterioration (damage). Probably there has been a rearrangement of the MWCNTs or some sort of healing going. They have gone from one disorderly state to ordered one.

IV.2.2.4. 120 minutes milling time

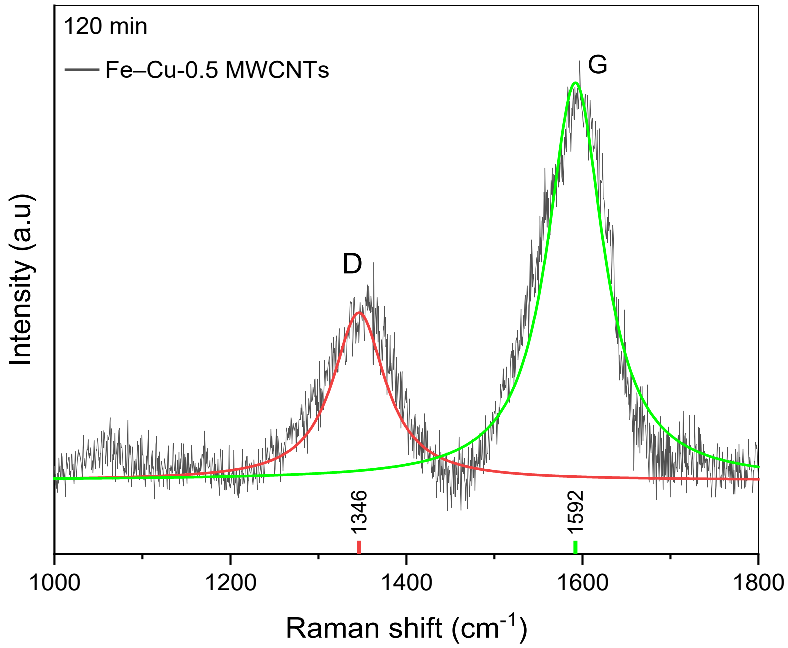

Figure. 4.52: Raman spectra of Fe–Cu-0.5% MWCNTs (120 min).

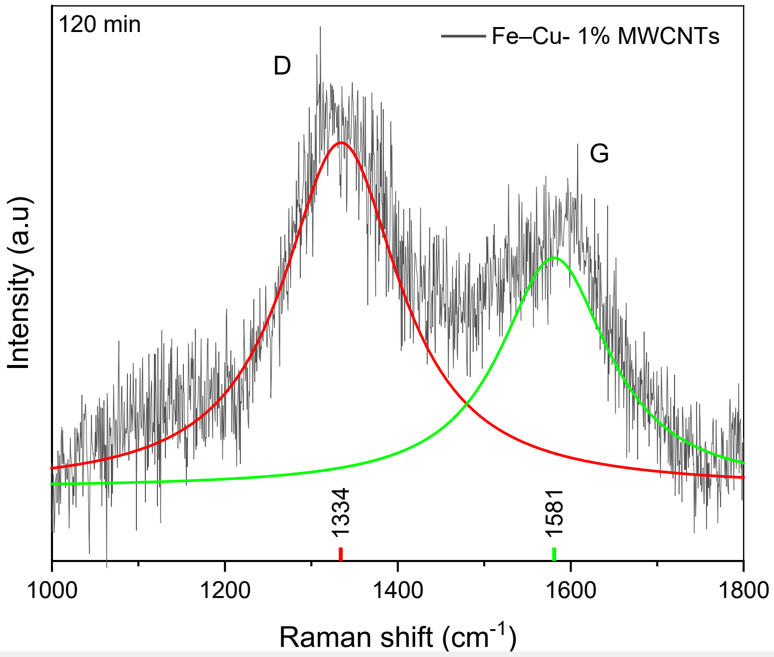

Figure. 4.53: Raman spectra of Fe–Cu-1% MWCNTs (120 min).

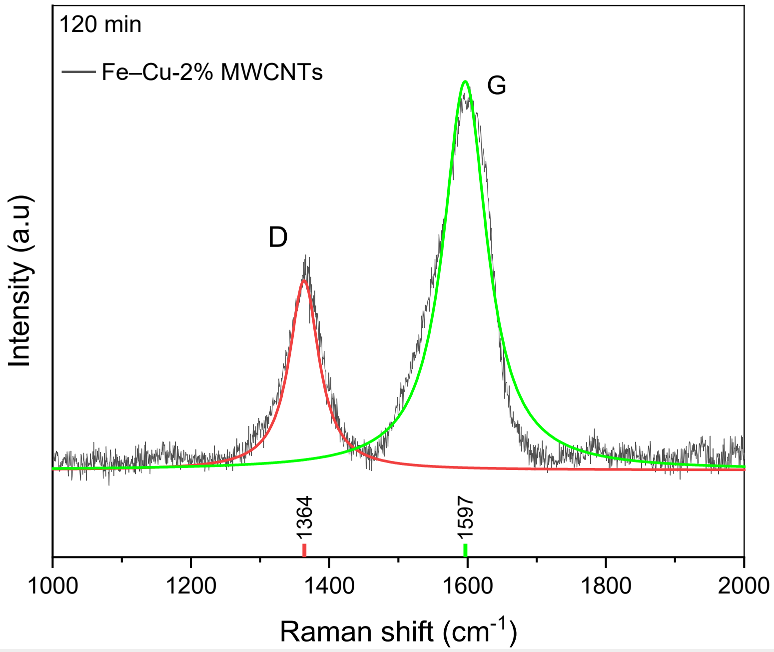

Figure. 4.54: Raman spectra of Fe–Cu-2% MWCNTs (120 min).

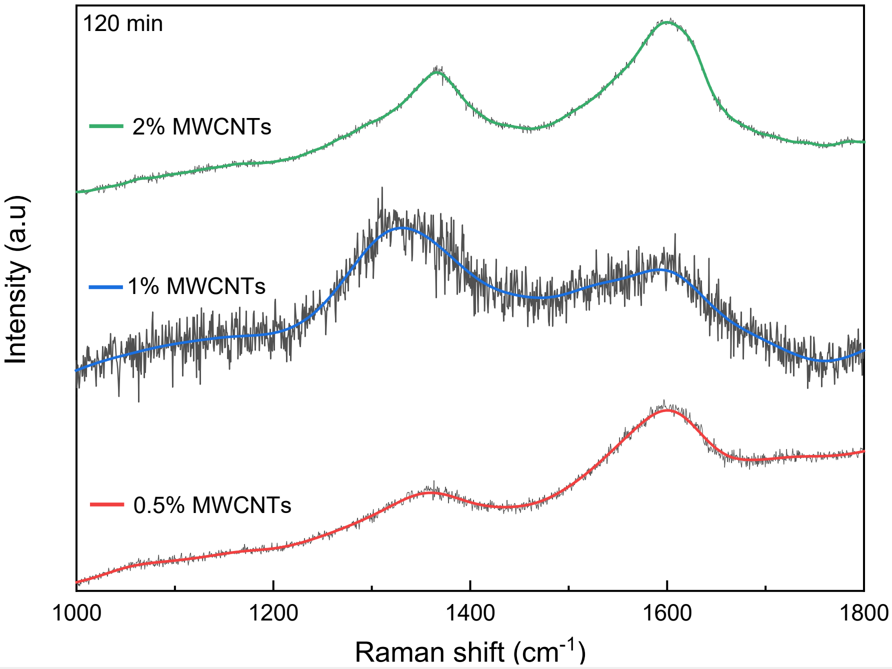

Figure. 4.55: Raman spectra of Fe–Cu-X% MWCNTs (120 min).

The passage to a longer grinding time changes the relative intensity of the Raman spectra of the three samples.

The curves are strongly dependent on the concentration. For the smallest concentration (0.5% MWCNTs), the shape of the Raman curve is different from that of the other two. The D peak is very large and has a tendency to fade out, so its intensity has diminished. On the other hand, the peak G is intense. This implies a reduced I_D/I_G ratio. This is characteristic of a structure with few defects. This behaviour can lead to the transformation of MWCNTs from one disordered state to another order, as well as the healing of structural defects. When the concentration becomes equal to 1% MWCNTs, the roles are reversed. D peak intensifies as G flattens out. This leads to a large ratio leading to a high concentration of defects involving deterioration of the MWCNTs. When the concentration increases to reach 2% MWCNTs, the situation returns to the previous state where the MWCNTs have less deterioration and a small number of defects is present. On the other hand, the grinding at 120 minutes led to a shift in the frequencies of occurrence of D and G compared to previous cases. This situation may be linked to the fact that MWCNTs are constrained. [276]

Table 4.4: Peak frequencies, bandwidths, and relative intensities of *D* and *G* bands in the Raman spectra of Fe–Cu- X% MWCNTs nanocomposite with different milling times. ν_D and ν_G are the peak frequencies of *D*, *G* bands, respectively. W_D, W_G, are the widths [full widths at half maximums (FWHM)] of *D* and *G* bands, respectively. I_D/I_G is the peak intensity ratio of the *D* band to the *G* band. Each band was analysed by fitting with a Lorentzian line.

	MWCNTs (%)	ν_D (cm^{-1})	W_D (cm^{-1})	ν_G (cm^{-1})	W_G (cm^{-1})	I_D/I_G
20 min	0.5	1369	-	1596	-	1.1
	1	1360	87.9	1599	83.7	1.07
	2	1347	107.4	1595	44.8	1.03
60 min	0.5	1338	107	1586	94	0.3
	1	1331	101	1580	119	0.38
	2	1337	113	1587	105	0.29
120 min	0.5	1346	73.1	1592	77.3	0.41
	1	1334	164.9	1581	153.4	1.11
	2	1364	52.4	1597	76.9	0.47

As it is well known in the literature for graphite alike behaviour when undergoes investigation using Raman spectroscopy, we observe the presence of the two characteristic peaks, D and G in the Fe–Cu nanocomposite with different concentrations of multiwall carbon nanotubes, the above **table 4.4** provide information's concerning Raman characterisation; peaks, frequencies, bandwidth, and relative intensities related to both D and *G* bands.

For the characterisation of the structures of the graphitelike carbons, the W_G bandwidth and the I_D/I_G intensity ratio has been widely used. [277–282] It is well known that both W_G and I_D/I_G increases with an increasing disorder in the graphite structure. [277,278] In addition, it has been reported that the I_D/I_G intensity ratio is inversely proportional to the size of the finite crystallites constituting the graphitelike carbons. [245,278] Therefore, the W_G indicates the degree of graphitization, and the I_D/I_G concerns not only the degree of graphitization but also the crystallite size.

The Raman spectra, obtained in the range 1000–2000 cm^{-1}, shows the frequency of the G band values in between 1570–1599 cm^{-1} due to the A_{g1}, E_{1g} and E_{2g} vibrational modes, and the frequency of the D band in between 1334–1361 cm^{-1} arising from the disorder-induced A_{g1} mode.

The G band is wide and its intensity is higher is more than twice that of the D band. The width of the G band is related to the CNTs size distribution whereas the intensity of the D band decreases with the degree of graphitization of the tubes. In this work, Raman spectroscopy was mainly used to verify the multiwalled morphological state and the overall homogeneity of the sample.

From the evaluations of I_D/I_G ratios and D-band intensities, it can be seen that the 1% concentration of MWCNT creates the fewest defects. In the latter, the presence of defects is low compared to that observed for the other concentration of MWCNTs. This means that the MWCNT in the Fe–Cu-1% MWCNTs nanocomposite is the least deteriorated. The intensity of the G band increasing and the I_D/I_G ratio decreasing as a function of the MWCNT concentration, this behaviour leads to a transformation of the MWCNTs from one disordered state to another ordered, as well as to the healing of structural defects. The I_D/I_G ratios remain relatively low compared to those found in the literature, where the I_D/ I_G ratios are between 0.5 and 3. This range of I_D/I_G can mean that the MWCNTs were not damaged [276].

IV.2.3 Infrared spectroscopy

IV.2.3.1. 20 min milling time

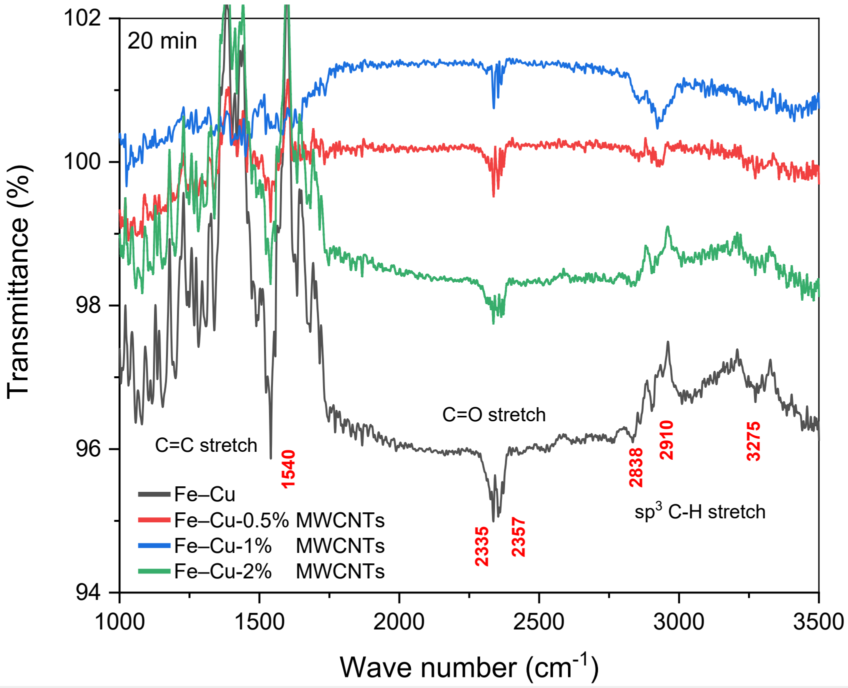

Figure. 4.56: Infrared transmittance spectroscopy of Fe–Cu-X% MWCNTs (20 min).

The figure above presents the charts of infrared transmittance for the Fe–Cu-X% MWCNTs nanocomposite with 20 minutes grinding time. The presence of an intense peak at a frequency of 1540 cm^{-1} correspond to the aromatic ring stretch $C = C$ bond, especially for the sample it should have no carbon derivative in, possibly of contamination during the preparation (highly unlikely) or during the FTIR characterisation. As for the intensity it is higher for the 2%, 0.5% and 1% MWCNTs respectively.

A relatively intense peak at 2235 cm^{-1} and 2357 cm^{-1} corresponded to the carbonyl group $C = O$, the intensity is higher for the Fe–Cu followed by the 0.5%, 1% and 2% MWCNTs respectively.

Presence of peaks at 2838 cm^{-1}, 2910 cm^{-1} and 3275 cm^{-1} of the functional groups $C-H$.

IV.2.3.2. 60 min milling time

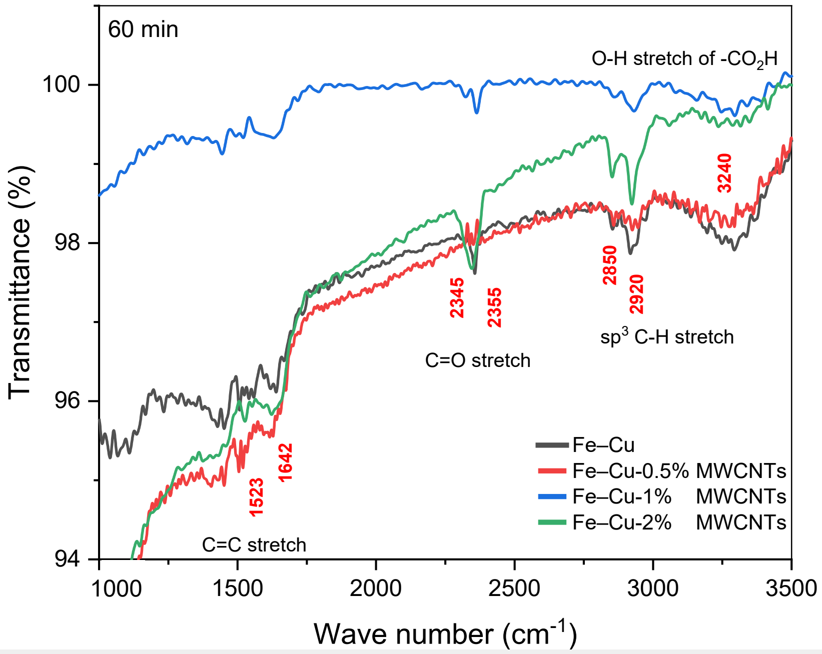

Figure. 4.57: Infrared transmittance spectroscopy of Fe–Cu-X% MWCNTs (60 min).

For the Fe–Cu-X% MWCNTs ground for 60 minutes, the figure above shows the presence of relatively low intense peaks at 1523 cm^{-1} and 1642 cm^{-1} corresponds for the aromatic ring stretch $C = C$.

Two peaks at around 2345 cm^{-1} and 2355 cm^{-1} correspond to the $C = O$ bond with relatively high intensity for the 2% MWCNTs

The peaks at 2850 cm^{-1} and 2920 cm^{-1} are associated with the $C-H$ stretching vibration modes.

IV.2.3.3. 120 min milling time

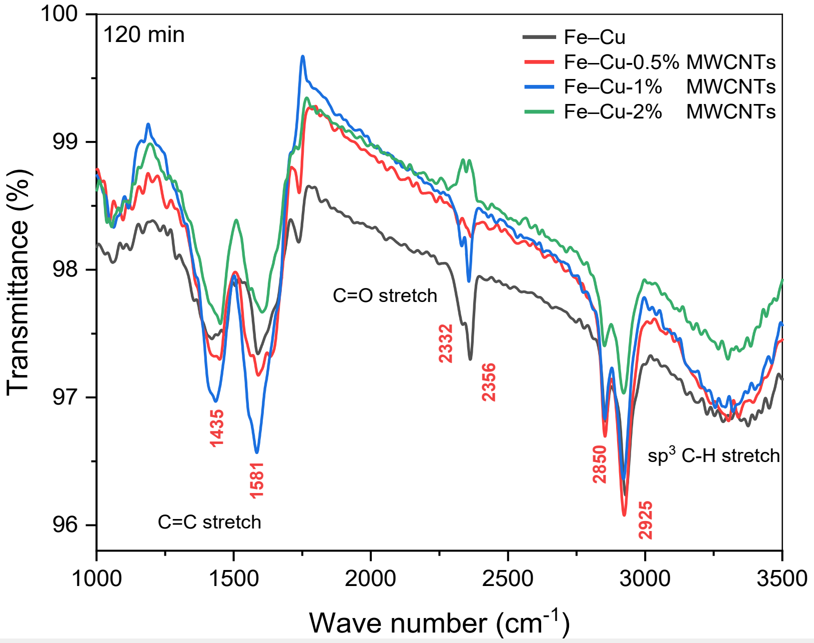

Figure. 4.58: Infrared transmittance spectroscopy of Fe–Cu-X% MWCNTs (120 min).

Infrared spectroscopy was used to show the presence of functional groups in the Fe–Cu-X% MWCNTs nanocomposites. The presence of an intense characteristic peak corresponds to the aromatic ring stretch $C=C$ bond at around 1523 cm^{-1} and 1642 cm^{-1} for the 120 minutes samples that contained MWCNTs and relatively low for the other milling times.

Two peaks have relatively lower intensity compared to the previous ones corresponding to the carbonyl group $C=O$ at around 2345 cm^{-1} and 2355 cm^{-1}, respectively. This may indicate a free bond on the surface of deteriorating CNTs, also indicating higher oxidation for the Fe–Cu without MWCNTs which has an intense peak compared to the samples with 1%, 0.5% and 2% MWCNTs respectively.

Furthermore, a presence of intense dominant peaks corresponds to $C-H$ bond at a frequency around 2850 cm^{-1} and 2920 cm^{-1}

Conclusion

Summary

A classical powder metallurgy route can be used to produce a different aspect ratio of difficult solubility alloys such as iron-copper (4:1) nanocomposites with the volume additions of multiwall carbon nanotubes of 0.5, 1.0, and 2.0% respectively with different grinding times of 20, 60 and 120 minutes.

This study has evaluated the influence of the dispersion of multiwall carbon nanotubes regarding the presented quantities, and the effect of milling time on both the Fe–Cu nanocomposite thermal behaviour as of heat flow (C_p), weight variation and linear coefficient of thermal expansion (CTE or α(T)), the presence phases as well as “grain size”, the morphological state of the carbon nanotubes, which plays a very important role in altering grain size, distributing load and heat throughout the matrix.

The heat flow and thermogravimetry show thermal stability and higher calorific capacity for the samples with longer milling time and containing the highest concentration of CNTs.

As for the coefficient of thermal expansion, an improved CTE of the Fe–Cu-1% MWCNTs milled for 120 minutes.

The provided x-ray diffraction patterns show a grain refinement for the 120 minutes milling time as well as a homogenous distribution of CNTs (the absence of CNTs clusters appearing as carbon graphite).

Raman spectroscopy, on the other hand, assessed the CNTs morphology integrity and damage state of the milling time, it reveals a higher defect density with longer milling time, with an exception for the 60 minutes it shows a lower defect density which indicates the healing and the recovery of CNTs. However, the results of Raman spectroscopy shows that damage to the structure of the CNTs is higher with longer milling time, thus compromising the beneficial effect of better dispersion.

Infrared spectroscopy aid in showing the presence of functional groups in the samples and the establishment of multiple bonding types.

Outlook

Furthermore, there are few (if not fewer) studies regarding Fe–Cu nanocomposites embedding different concentrations of multiwalled carbon nanotubes, more studies that must be carried out, due to the lack of literature concerning this subject.

Mechanical milling contains lots of variables in the process of preparing a nanocomposite, pursuing and dedication of every detail may unveil unexpected results on all different properties.

References

[1] Dresselhaus, M. S., Dresselhaus, G., Sugihara, K., Spain, I. L. & Goldberg, H. A. Synthesis of Graphite Fibers and Filaments. in *Graphite Fibers and Filaments* 12–34 (Springer, 1988). DOI CrossRef Google Scholar

[2] Kelly, B. T. Physics of Graphite (Applied Science, London) (1981). CrossRef Google Scholar

[3] Bundy, F. P. The P, T phase, and reaction diagram for elemental carbon. *J. Geophys. Res.* **85**, 6930–6936 (1980). DOI CrossRef Google Scholar

[4] Bundy, F. P., Bassett, W. A., Weathers, M. S., Hemley, R. J., Mao, H. K., and Goncharov, A. F. The pressure-temperature phase and transformation diagram for carbon. *Carbon.* **34**, 141–153 (1996). DOI CrossRef Google Scholar

[5] Lipson, H., Stokes, A. A New Structure of Carbon. *Nature* **149**, 328 (1942). DOI CrossRef Google Scholar

[6] Moore, A.W., Highly Oriented Pyrolytic Graphite. **11**. Marcel Dekker, New York, (1973). Google Scholar

[7] Heremans, J., Olk, C. H., Eesley, G. L., Steinbeck, J. & Dresselhaus, G. Observation of metallic conductivity in liquid carbon. *Phys. Rev. Lett.* **60**, 452–455 (1988). DOI CrossRef Google Scholar

[8] Lucchese, M. M. *et al.* Quantifying ion-induced defects and Raman relaxation length in graphene. *Carbon N. Y.* **48**, 1592–1597 (2010). DOI CrossRef Google Scholar

[9] Wyckoff, R. W. G. Crystal Structures, Vol. 1, Interscience Publ. *Inc., New York* (1963). Google Scholar

[10] Bundy, F. P. & Kasper, J. S. Hexagonal diamond—a new form of carbon. *J. Chem. Phys.* **46**, 3437–3446 (1967). DOI CrossRef Google Scholar

[11] Council, N. R. METHANE. in *Emergency and Continuous Exposure Limits for Selected Airborne Contaminants: Volume 1* (National Academies Press (US), 1984). Google Scholar

[12] Taliani, C., Zamboni, R. & Ruani, G. *Fullerenes: Status And Perspectives-Proceedings Of The First Italian Workshop*. vol. 2 (World Scientific, 1992). Google Scholar

[13] Leger, A., D'Hendecourt, L., Verstraete, L. & Schmidt, W. Remarkable candidates for the carrier of the diffuse interstellar bands - C60(+) and other polyhedral carbon ions. *Astron. Astrophys.* **203**, 145–148 (1988). CrossRef Google Scholar

[14] Kroto, H. W. Special Issue on Fullerenes. *Carbon N. Y.* **30**, 1139 (1992). Google Scholar

[15] Kroto, H., Heath, J., O'Brien, S. *et al.* C_{60}: Buckminsterfullerene. *Nature* **318**, 162–163 (1985). DOI CrossRef Google Scholar

[16] J. Baggott, *Perfect symmetry*: *the accidental discovery of buckminsterfullerene*, Oxford University Press, 1994. Google Scholar

[17] H. Aldersey-Williams, *The most beautiful molecule*, Aurum Press, London, 1995. DOI CrossRef Google Scholar

[18] Dresselhaus, M. S., Dresselhaus, G. & Eklund, P. C. *Science of Fullerenes and Carbon Nanotubes*. *Science of Fullerenes and Carbon Nanotubes* (Elsevier, 1996). Google Scholar

[19] W. J. Anton, R. W. Stephen, I. S. David, Biological Applications of Fullerenes. New York City, NY: Elsevier Science, 1996. Google Scholar

[20] Terrones, H. & Terrones, M. The transformation of polyhedral particles into graphitic onions. *J. Phys. Chem. Solids* **58**, 1789–1796 (1997). DOI CrossRef Google Scholar

[21] Ruoff, R. S. & Ruoff, A. L. The bulk modulus of C60 molecules and crystals: A molecular mechanic's approach. *Appl. Phys. Lett.* **59**, 1553–1555 (1991). DOI CrossRef Google Scholar

[22] Withers, J. C., Loutfy, R. O. & Löwe, T. P. Fullerene commercial vision. *Fuller. Sci. Technol.* **5**, 1–31 (1997). DOI CrossRef Google Scholar

[23] Imahori, H. & Sakata, Y. Donor-linked fullerenes: Photoinduced electron transfer and its potential application. *Adv. Mater.* **9**, 537–546 (1997). DOI CrossRef Google Scholar

[24] M. Monthioux, V.L. Kuznetsov: Who should be given the credit for the discovery of carbon nanotubes? *Carbon* **44**, 1621–1623 (2006). DOI CrossRef Google Scholar

[25] L.V. Radushkevich, V.M. Lukyanovich: O strukture ugleroda, obrazujucegosja pri termiceskom razlozeniiokisi ugleroda na zeleznomkontakte, *Zurn. Fis. Chim*. **26**, 88–95 (1952). Google Scholar

[26] Oberlin, A., Endo, M. & Koyama, T. High resolution electron microscope observations of graphitized carbon fibres. (1976). CrossRef Google Scholar

[27] Oberlin, A., Endo, M. & Koyama, T. Filamentous growth of carbon through benzene decomposition. *J. Cryst. Growth* **32**, 335–349 (1976). DOI CrossRef Google Scholar

[28] Oberlin, A. Carbonization and graphitization. *Carbon N. Y.* **22**, 521–541 (1984). DOI CrossRef Google Scholar

[29] Kroto, H.W., Heath, J.R., O'Brien, S.C., Curl, R.F., and Smalley, R.E., *Nature* **318**, 162–163, (1985). DOI CrossRef Google Scholar

[30] Iijima, S. Helical microtubules of graphitic carbon. *Nature* **354**, 56–58 (1991). DOI CrossRef Google Scholar

[31] Iijima, S. & Ichihashi, T. Single-shell carbon nanotubes of 1-nm diameter. *Nature* **363**, 603–605 (1993). DOI CrossRef Google Scholar

[32] Bethune, D. S. *et al.* Cobalt-catalysed growth of carbon nanotubes with single-atomic-layer walls. *Nature* **363**, 605–607 (1993). DOI CrossRef Google Scholar

[33] Dresselhaus, M. S., Dresselhaus, G. & Eklund, P. C. *Science of Fullerenes and Carbon Nanotubes*. *Science of Fullerenes and Carbon Nanotubes* (Elsevier, 1996). Google Scholar

[34] Dresselhaus, M.S., Dresselhaus, G., Saito, R., Carbon fibers based on C_{60} and their symmetry. *Phys. Rev. B* **45**, 6234 (1992). DOI CrossRef Google Scholar

[35] Hamada, N., Sawada, S. & Oshiyama, A. New one-dimensional conductors: Graphitic microtubules. *Phys. Rev. Lett.* **68**, 1579 (1992). DOI CrossRef Google Scholar

[36] R. Saito, G. Dresselhaus, M.S. Dresselhaus, Physical Properties of Carbon Nanotubes, Imperial College Press, London, 1998. DOI CrossRef Google Scholar

[37] Birch, M. E., Ruda-Eberenz, T. A., Chai, M., Andrews, R. & Hatfield, R. L. Properties that influence the specific surface areas of carbon nanotubes and nanofibers. *Ann. Occup. Hyg.* **57**, 1148–1166 (2013). DOI CrossRef Google Scholar

[38] Eswaramoorthy, M., Sen, R. & Rao, C. N. R. A study of micropores in single-walled carbon nanotubes by the adsorption of gases and vapors. in *Chemical Physics Letters* vol. 304 207–210 (World Scientific, 1999). DOI CrossRef Google Scholar

[39] Peigney, A., Laurent, C., Flahaut, E., Bacsa, R. R. & Rousset, A. Specific surface area of carbon nanotubes and bundles of carbon nanotubes. *Carbon N. Y.* **39**, 507–514 (2001). DOI CrossRef Google Scholar

[40] Balch, A. L. & Olmstead, M. M. Reactions of transition metal complexes with fullerenes (C60, C70, etc.) and related materials. *Chem. Rev.* **98**, 2123–2166 (1998). Google Scholar

[41] Kim, P., Shi, L., Majumdar, A. & McEuen, P. L. Thermal transport measurements of individual multiwalled nanotubes. *Phys. Rev. Lett.* **87**, 215502-1-215502–4 (2001). DOI CrossRef Google Scholar

[42] Che, J., Çqgin, T., Goddard III, W.A. *Nanotechnology.* **11**, 65 (2000). DOI CrossRef Google Scholar

[43] Treacy, M. M. J., Ebbesen, T. W. & Gibson, J. M. Exceptionally high Young's modulus observed for individual carbon nanotubes. *Nature* **381**, 678–680 (1996). DOI CrossRef Google Scholar

[44] Krishnan, A., Dujardin, E., Ebbesen, T. W., Yianilos, P. N. & Treacy, M. M. J. Young's modulus of single-walled nanotubes. *Phys. Rev. B* **58**, 14013 (1998). DOI CrossRef Google Scholar

[45] Wong, E. W., Sheehan, P. E. & Lieber, C. M. Nanobeam mechanics: elasticity, strength, and toughness of nanorods and nanotubes. *Science (80-.).* **277**, 1971–1975 (1997). DOI CrossRef Google Scholar

[46] Lourie, O. & Wagner, H. D. Evaluation of Young's modulus of carbon nanotubes by micro-Raman spectroscopy. *J. Mater. Res.* **13**, 2418–2422 (1998). Google Scholar

[47] Poncharal, P., Wang, Z. L., Ugarte, D. & De Heer, W. A. Electrostatic deflections and electromechanical resonances of carbon nanotubes. *Science (80-.).* **283**, 1513–1516 (1999). DOI CrossRef Google Scholar

[48] Salvetat, J. P. *et al.* Elastic modulus of ordered and disordered multiwalled carbon nanotubes. *Adv. Mater.* **11**, 161–165 (1999). DOI CrossRef Google Scholar

[49] Salvetat, J. P. *et al.* Elastic and shear moduli of single-walled carbon nanotube ropes. *Phys. Rev. Lett.* **82**, 944–947 (1999). Google Scholar

[50] Yu, M. F. *et al.* Strength and breaking mechanism of multiwalled carbon nanotubes under tensile load. *Science (80-.).* **287**, 637–640 (2000). Google Scholar

[51] Yu, M. F., Files, B. S., Arepalli, S. & Ruoff, R. S. Tensile loading of ropes of single wall carbon nanotubes and their mechanical properties. *Phys. Rev. Lett.* **84**, 5552–5555 (2000). Google Scholar

[52] Krueger, A. & Monthioux, M. Carbon Nanotubes. *Strained Hydrocarbons: Beyond the van-t Hoff and Le Bel Hypothesis* 335–373 (2009). DOI CrossRef Google Scholar

[53] Dai, H., Hafner, J., Rinzler, A. *et al.* Nanotubes as nanoprobes in scanning probe microscopy. *Nature* **384,** 147–150 (1996). DOI CrossRef Google Scholar

[54] Hafner, J. H., Cheung, C. L., Woolley, A. T. & Lieber, C. M. Structural and functional imaging with carbon nanotube AFM probes. *Prog. Biophys. Mol. Biol.* **77**, 73–110 (2001). DOI CrossRef Google Scholar

[55] De Heer, W. A., Châtelain, A. & Ugarte, D. A carbon nanotube field-emission electron source. *Science (80-.).* **270**, 1179–1180 (1995). DOI CrossRef Google Scholar

[56] Trottier, C. M., Glatkowski, P., Wallis, P. & Luo, J. Properties and characterization of carbon-nanotube-based transparent conductive coating. *J. Soc. Inf. Disp.* **13**, 759 (2005). DOI CrossRef Google Scholar

[57] Rueckes, T. *et al.* Carbon nanotube-based nonvolatile random access memory for molecular computing. *Science (80-.).* **289**, 94–97 (2000). DOI CrossRef Google Scholar

[58] De Volder, M. F. L., Tawfick, S. H., Baughman, R. H. & Hart, A. J. Carbon nanotubes: Present and future commercial applications. *Science (80-.).* **339**, 535–539 (2013). DOI CrossRef Google Scholar

[59] Hawkins, T. & Drozdz, S. Cathodic Nanocoating Technology for Corrosion Control of Steel Structures. in *The Waterborne Coatings Symposium 2012* (2012). CrossRef Google Scholar

[60] De Las Casas, C. & Li, W. A review of application of carbon nanotubes for lithium ion battery anode material. *J. Power Sources* **208**, 74–85 (2012). DOI CrossRef Google Scholar

[61] Landi, B. J., Ganter, M. J., Cress, C. D., DiLeo, R. A. & Raffaelle, R. P. Carbon nanotubes for lithium ion batteries. *Energy Environ. Sci.* **2**, 638–654 (2009). DOI CrossRef Google Scholar

[62] Endo, M., Hayashi, T. & Kim, Y. A. Large-scale production of carbon nanotubes and their applications. *Pure Appl. Chem.* **78**, 1703–1713 (2006). DOI CrossRef Google Scholar

[63] Bharech, S. & Kumar, R. A review on the properties and applications of graphene. *J Mater Sci Mech Eng* **2**, 70 (2015). Website Google Scholar

[64] Frank, I. W., Tanenbaum, D. M., van der Zande, A. M. & McEuen, P. L. Mechanical properties of suspended graphene sheets. *J. Vac. Sci. Technol. B Microelectron. Nanom. Struct. Process. Meas. Phenom.* **25**, 2558–2561 (2007). DOI CrossRef Google Scholar

[65] Balandin, A. A. *et al.* Superior thermal conductivity of single-layer graphene. *Nano Lett.* **8**, 902–907 (2008). DOI CrossRef Google Scholar

[66] Nair, R. R., Blake, P., Grigorenko, A. N., Novoselov, K. S., Booth, T. J., Stauber, T., et al. Fine structure constant defines visual transparency of graphene. *Science.* **320**(5881), 1308–1308 (2008). DOI CrossRef Google Scholar

[67] Novoselov, K. S., Geim, A. K., Morozov, S. V., Jiang, D., Zhang, Y., Dubonos, S. V., et al. Electric field effect in atomically thin carbon films. *Science*. **306**(5696), 666–669 (2004). DOI CrossRef Google Scholar

[68] Zhang, Y. B., Tan, Y. W., Stormer, H. L., & Kim, P. Experimental observation of the quantum Hall effect and Berry's phase in graphene. *Nature*. **438**(7065), 201–204 (2005). DOI CrossRef Google Scholar

[69] Schedin, F., Geim, A., Morozov, S. *et al.* Detection of individual gas molecules adsorbed on graphene. *Nature Mater* **6,** 652–655 (2007). DOI CrossRef Google Scholar

[70] Li, X. L., Wang, X. R., Zhang, L., Lee, S. W., & Dai, H. J. Chemically derived ultra-smooth graphene nanoribbon semiconductors. *Science*, **319**(5867), 1229–1232 (2008). DOI CrossRef Google Scholar

[71] Stankovich, S., Dikin, D. A., Dommett, G. H. B., Kohlhaas, K. M., Zimney, E. J., Stach, E. A., et al. Graphene-based composite materials. *Nature*, **442**, 282–286 (2006). DOI CrossRef Google Scholar

[72] Wang, S. *et al.* High field emission reproducibility and stability of carbon nanosheets and nanosheet-based backgated triode emission devices. *Appl. Phys. Lett.* **89**, 183103 (2006). DOI CrossRef Google Scholar

[73] Lu, G. H., Park, S., Yu, K. H., Ruoff, R. S., Ocola, L. E., Chen, J. H., et al. Toward practical gas sensing with highly reduced graphene oxide: A new signal processing method to circumvent run-to-run and device-to-device variations. *ACS Nano*, **5**, 1154–1164 (2011). DOI CrossRef Google Scholar

[74] Lu, G. H., Ocola, L. E., & Chen, J. H. Gas detection using low-temperature reduced graphene oxide sheets. *Appl. Phys. Lett.* **94**, 083111 (2009). DOI CrossRef Google Scholar

[75] Mao, S., Lu, G. H., Yu, K. H., Bo, Z., & Chen, J. H. Specific protein detection using thermally reduced graphene oxide sheet decorated with gold nanoparticle-antibody conjugates. *Adv Materi*, **22**, 3521–3526 (2010). DOI CrossRef Google Scholar

[76] Ohno, Y., Maehashi, K., & Matsumoto, K. Label-free biosensors based on aptamer-modified graphene field-effect transistors. *J. Am. Chem. Soc.* **132**, 18012–18013 (2010). DOI CrossRef Google Scholar

[77] Patchkovskii, S. *et al.* Graphene nanostructures as tunable storage media for molecular hydrogen. *Proc. Natl. Acad. Sci. U. S. A.* **102**, 10439–10444 (2005). DOI CrossRef Google Scholar

[78] Blake, P. *et al.* Graphene-based liquid crystal device. *Nano Lett.* **8**, 1704–1708 (2008). DOI CrossRef Google Scholar

[79] De, S. *et al.* Flexible, transparent, conducting films of randomly stacked graphene from surfactant-stabilized, oxide-free graphene dispersions. *Small* **6**, 458–464 (2010). DOI CrossRef Google Scholar

[80] Ramanathan, T. *et al.* Functionalized graphene sheets for polymer nanocomposites. *Nat. Nanotechnol.* **3**, 327–331 (2008). DOI CrossRef Google Scholar

[81] Robinson, J. T., Perkins, F. K., Snow, E. S., Wei, Z. & Sheehan, P. E. Reduced graphene oxide molecular sensors. *Nano Lett.* **8**, 3137–3140 (2008). DOI CrossRef Google Scholar

[82] Lagow, R. J. *et al.* Synthesis of linear acetylenic carbon: The 'sp' carbon allotrope. *Science (80-.).* **267**, 362–367 (1995). DOI CrossRef Google Scholar

[83] Kasatochkin, V. I., Sladkov, A. M., Kudryavtsev, Y. P., Popov, N. M. & Korshak, V. V. Crystalline forms of a linear modification of carbon. *Dokl. Akad. Nauk SSSR* **177**, 358–360 (1967). Google Scholar

[84] Goresy, A. E. & Donnay, G. A new allotropic form of carbon from Ries Crater. *Science,* **161**, 363–364 (1968). DOI CrossRef Google Scholar

[85] Whittaker, A. G. & Kintner, P. L. Carbon: observations of new allotropic form. Science **165**, 589–591 (1969). DOI CrossRef Google Scholar

[86] Sladkov, A. & Kudryavtsev, Y. Diamond, graphite, carbyne: allotropic forms of carbon. Priroda **5**, 37–44 (1969). CrossRef Google Scholar

[87] F. P. Bundy. In Solid State Physics under Pressure: Recent Advance with Anvil Devices, edited by S. Minomura, page 1, D. Reidel, Dordrecht, 1985. Google Scholar

[88] Kasatochkin, V. I., A. M. Sladkov, Kudryavtsev, Y. P., Popov, N. M, and Korshak, V. V., *Dokl. Chem*. **177**, 1031 (1967). Google Scholar

[89] Kasatochkin, V. I., Korshak, V. V., Kudryavtsev, Y. P., Sladkov, A. M. & Sterenberg, I. E. On crystalline structure of carbyne. *Carbon N. Y.* **11**, 70–72 (1973). DOI CrossRef Google Scholar

[90] Whitaker, A. G. & Kintner, P. L. Carbon: Analysis of spherules and splats formed from the liquid state and of the forms produced by quenching gas and solid. *Carbon N. Y.* **23**, 255–262 (1985). DOI CrossRef Google Scholar

[91] Whittaker, A. G. & Kintner, P. L. Carbon: observations on the new allotropic form. *Science.* **165**, 589–591(1969). DOI CrossRef Google Scholar

[92] Whittaker, A. G. Carbon: A new view of its high-temperature behavior. *Science (80-.).* **200**, 763–764 (1978). DOI CrossRef Google Scholar

[93] Whittaker, A. G., Watts, E. J., Lewis, R. S. & Anders, E. Carbynes: Carriers of primordial noble gases in meteorites. *Science (80-.).* **209**, 1512–1514 (1980). DOI CrossRef Google Scholar

[94] El Goresy, A. & Donnay, G. A new allotropic form of carbon from the Ries crater. *Science (80-.).* **161**, 363–364 (1968). DOI CrossRef Google Scholar

[95] Heimann, R. B., Kleiman, J. & Salansky, N. M. A unified structural approach to linear carbon polytypes. *Nature* **306**, 164–167 (1983). DOI CrossRef Google Scholar

[96] Whittaker, A. G. & Wolten, G. M. Carbon: a suggested new hexagonal crystal form. *Science (80-.).* **178**, 54–56 (1972). DOI CrossRef Google Scholar

[97] Shi, L. *et al.* Confined linear carbon chains as a route to bulk carbyne. *Nat. Mater.* **15**, 634–639 (2016). DOI CrossRef Google Scholar

[98] Liu, M. J., Artyukhov, V. I., Lee, H., Xu, F. B. & Yakobson, B. I. Carbyne from first principles: chain of C atoms, a nanorod or a nanorope. *ACS Nano* **7**, 10075–10082 (2013). DOI CrossRef Google Scholar

[99] Baughman, R. H., Eckhardt, H. & Kertesz, M. Structure-property predictions for new planar forms of carbon: Layered phases containing sp^2 and sp atoms. *J. Chem. Phys.* **87**, 6687–6699 (1987). DOI CrossRef Google Scholar

[100] Li, G. *et al.* Architecture of graphdiyne nanoscale films. *Chem. Commun.* **46**, 3256–3258 (2010). DOI CrossRef Google Scholar

[101] Yue, Q., Chang, S., Kang, J., Qin, S. & Li, J. Mechanical and electronic properties of graphyne and its family under elastic strain: Theoretical predictions. *J. Phys. Chem. C* **117**, 14804–14811 (2013). DOI CrossRef Google Scholar

[102] Narita, N. & Nagai, S. Optimized geometries and electronic structures of graphyne and its family. *Phys. Rev. B - Condens. Matter Mater. Phys.* **58**, 11009–11014 (1998). DOI CrossRef Google Scholar

[103] Malko, D., Neiss, C., Viñes, F. & Görling, A. Competition for graphene: Graphynes with direction-dependent dirac cones. *Phys. Rev. Lett.* **108**, 86804 (2012). DOI CrossRef Google Scholar

[104] Kang, J., Li, J., Wu, F., Li, S. S. & Xia, J. B. Elastic, electronic, and optical properties of two-dimensional graphyne sheet. *J. Phys. Chem. C* **115**, 20466–20470 (2011). DOI CrossRef Google Scholar

[105] Krätschmer, W., Lamb, L. D., Fostiropoulos, K. & Huffman, D. R. Solid C60: a new form of carbon. *Nature* **347**, 354–358 (1990). DOI CrossRef Google Scholar

[106] Fulcheri, L. *et al.* Fullerene production in a 3-phase AC plasma process. *Carbon N. Y.* **38**, 797–803 (2000). DOI CrossRef Google Scholar

[107] Saïdane, K. *et al.* Fullerene synthesis in the graphite electrode arc process: Local plasma characteristics and correlation with yield. *J. Phys. D. Appl. Phys.* **37**, 232–239 (2004). DOI CrossRef Google Scholar

[108] Bacon, R. Growth, structure, and properties of graphite whiskers. *J. Appl. Phys.* **31**, 283–290 (1960). **DOI** **CrossRef** **Google Scholar**

[109] Journet, C., Maser, W.K., Bernier, P. Loiseau, A. ML de la Chapelle, S. Lefrant, P. Deniard, R. Lee & J.E. Ficher. *Nature* **388**, 756–758 (1997). **DOI** **CrossRef** **Google Scholar**

[110] Takikawa, H. *et al.* Fabrication of single-walled carbon nanotubes and nanohorns by means of a torch arc in open air. *Phys. B Condens. Matter* **323**, 277–279 (2002). **DOI** **CrossRef** **Google Scholar**

[111] Antisari, M. V., Marazzi, R. & Krsmanovic, R. Synthesis of multiwall carbon nanotubes by electric arc discharge in liquid environments. *Carbon N. Y.* **41**, 2393–2401 (2003). **DOI** **CrossRef** **Google Scholar**

[112] Ebbesen, T. W. & Ajayan, P. M. Large-scale synthesis of carbon nanotubes. *Nature* **358**, 220–222 (1992). **DOI** **CrossRef** **Google Scholar**

[113] Ebbesen, T. W. *et al.* Patterns in the bulk growth of carbon nanotubes. *Chem. Phys. Lett.* **209**, 83–90 (1993). **DOI** **CrossRef** **Google Scholar**

[114] Taylor, G. H., Gerald, J. D. F., Pang, L. & Wilson, M. A. Cathode deposits in fullerene formation - microstructural evidence for independent pathways of pyrolytic carbon and nanobody formation. *J. Cryst. Growth* **135**, 157–164 (1994). **DOI** **CrossRef** **Google Scholar**

[115] Endo, M. *et al.* The production and structure of pyrolytic carbon nanotubes (PCNTs). *J. Phys. Chem. Solids* **54**, 1841–1848 (1993). **DOI** **CrossRef** **Google Scholar**

[116] Height, M. J., Howard, J. B., Tester, J. W. & Sande, J. B. V. Flame synthesis of single-walled carbon nanotubes. *Carbon N. Y.* **42**, 2295–2307 (2004). **DOI** **CrossRef** **Google Scholar**

[117] Rohmund, F., Falk, L. K. L. & Campbell, E. E. B. A simple method for the production of large arrays of aligned carbon nanotubes. *Chem. Phys. Lett.* **328**, 369–373 (2000). **DOI** **CrossRef** **Google Scholar**

[118] Sinnott, S. B. *et al.* Model of carbon nanotube growth through chemical vapor deposition. *Chem. Phys. Lett.* **315**, 25–30 (1999). **DOI** **CrossRef** **Google Scholar**

[119] Andrews, R. *et al.* Continuous production of aligned carbon nanotubes: A step closer to commercial realization. *Chem. Phys. Lett.* **303**, 467–474 (1999). **DOI** **CrossRef** **Google Scholar**

[120] Pan, Z., Xie, S., Chang, B. *et al.* Very long carbon nanotubes. *Nature* **394**, 631–632 (1998). **DOI** **CrossRef** **Google Scholar**

[121] Fan, S. *et al.* Self-oriented regular arrays of carbon nanotubes and their field emission properties. *Science (80-.).* **283**, 512–514 (1999). **DOI** **CrossRef** **Google Scholar**

[122] Gao, R., Wang, Z.L., and Fan, S. *J. Phys. Chem. B* **104**, 1227–1234 (2000). **DOI** **CrossRef** **Google Scholar**

[123] Grobert, N. *et al.* A novel route to aligned nanotubes and nanofibres using laser-patterned catalytic substrates. *Appl. Phys. A* **70**, 175–183 (2000). **DOI** **CrossRef** **Google Scholar**

[124] Kamalakaran, R. *et al.* Synthesis of thick and crystalline nanotube arrays by spray pyrolysis. *Appl. Phys. Lett.* **77**, 3385–3387 (2000). **DOI** **CrossRef** **Google Scholar**

[125] Mayne, M. *et al.* Pyrolytic production of aligned carbon nanotubes from homogeneously dispersed benzene-based aerosols. *Chem. Phys. Lett.* **338**, 101–107 (2001). **DOI** **CrossRef** **Google Scholar**

[126] Cassell, A. M., Verma, S., Delzeit, L., Meyyappan, M. & Han, J. Combinatorial optimization of heterogeneous catalysts used in the growth of carbon nanotubes. *Langmuir* **17**, 260–264 (2001). **DOI CrossRef Google Scholar**

[127] Cui, S., Lu, C. Z., Qiao, Y. L. & Cui, L. Large-scale preparation of carbon nanotubes by nickel catalyzed decomposition of methane at 600 °C. *Carbon (New York, NY)* **37**, 2070–2073 (1999). **DOI CrossRef Google Scholar**

[128] Willems, I. *et al.* Control of the outer diameter of thin carbon nanotubes synthesized by catalytic decomposition of hydrocarbons. *Chem. Phys. Lett.* **317**, 71–76 (2000). **DOI CrossRef Google Scholar**

[129] Lee, C. J. *et al.* Low-temperature growth of carbon nanotubes by thermal chemical vapor deposition using Pd, Cr, and Pt as co-catalyst. *Chem. Phys. Lett.* **327**, 277–283 (2000). **DOI CrossRef Google Scholar**

[130] Sen, R., Govindaraj, A. & Rao, C. N. R. Carbon nanotubes by the metallocene route. *Chem. Phys. Lett.* **267**, 276–280 (1997). **DOI CrossRef Google Scholar**

[131] Thess, A. *et al.* Crystalline ropes of metallic carbon nanotubes. *Science (80-.).* **273**, 483–487 (1996). **DOI CrossRef Google Scholar**

[132] Eklund, P. C. *et al.* Large-Scale Production of Single-Walled Carbon Nanotubes Using Ultrafast Pulses from a Free Electron Laser. *Nano Lett.* **2**, 561–566 (2002). **DOI CrossRef Google Scholar**

[133] Bolshakov, A. P. *et al.* A novel CW laser-powder method of carbon single-wall nanotubes production. *Diam. Relat. Mater.* **11**, 927–930 (2002). **DOI CrossRef Google Scholar**

[134] Hou, P. X., Liu, C. & Cheng, H. M. Purification of carbon nanotubes. *Carbon N. Y.* **46**, 2003–2025 (2008). **DOI CrossRef Google Scholar**

[135] Guo, T. *et al.* Self-assembly of tubular fullerenes. *J. Phys. Chem.* **99**, 10694–10697 (1995). **DOI CrossRef Google Scholar**

[136] Nikolaev, P. *et al.* Gas-phase catalytic growth of single-walled carbon nanotubes from carbon monoxide. *Chem. Phys. Lett.* **313**, 91–97 (1999). **DOI CrossRef Google Scholar**

[137] Bronikowski, M. J., Willis, P. A., Colbert, D. T., Smith, K. A. & Smalley, R. E. Gas-phase production of carbon single-walled nanotubes from carbon monoxide via the HiPco process: A parametric study. *J. Vac. Sci. Technol. A Vacuum, Surfaces, Film.* **19**, 1800–1805 (2001). **DOI CrossRef Google Scholar**

[138] Resasco, D. E. *et al.* A scalable process for production of single-walled carbon nanotubes (SWNTs) by catalytic disproportionation of CO on a solid catalyst. *J. Nanoparticle Res.* **4**, 131–136 (2002). **DOI CrossRef Google Scholar**

[139] Bachilo, S. M. *et al.* Narrow (n, m)-distribution of single-walled carbon nanotubes grown using a solid supported catalyst. *J. Am. Chem. Soc.* **125**, 11186–11187 (2003). **DOI CrossRef Google Scholar**

[140] Cassell, A. M., Raymakers, J. A., Kong, J. & Dai, H. Large Scale CVD Synthesis of Single-Walled Carbon Nanotubes. *J. Phys. Chem. B* **103**, 6484–6492 (1999). **DOI CrossRef Google Scholar**

[141] Lyu, S. C. *et al.* Large-scale synthesis of high-quality single-walled carbon nanotubes by catalytic decomposition of ethylene. *J. Phys. Chem. B* **108**, 1613–1616 (2004). **DOI CrossRef Google Scholar**

[142] Kitiyanan, B., Alvarez, W. E., Harwell, J. H. & Resasco, D. E. Controlled production of single-wall carbon nanotubes by catalytic decomposition of CO on bimetallic Co-Mo catalysts. *Chem. Phys. Lett.* **317**, 497–503 (2000). DOI CrossRef Google Scholar

[143] Herrera, J. E. & Resasco, D. E. Loss of single-walled carbon nanotubes selectivity by disruption of the Co-Mo interaction in the catalyst. *J. Catal.* **221**, 354–364 (2004). DOI CrossRef Google Scholar

[144] Alvarez, W. E., Pompeo, F., Herrera, J. E., Balzano, L. & Resasco, D. E. Characterization of single-walled carbon nanotubes (SWNTs) produced by CO disproportionation on Co-Mo catalysts. *Chem. Mater.* **14**, 1853–1858 (2002). DOI CrossRef Google Scholar

[145] Mizuno, K. *et al.* Selective matching of catalyst element and carbon source in single-walled carbon nanotube synthesis on silicon substrates. *J. Phys. Chem. B* **109**, 2632–2637 (2005). DOI CrossRef Google Scholar

[146] Dai, H. *et al.* Single-wall nanotubes produced by metal-catalyzed disproportionation of carbon monoxide. *Chem. Phys. Lett.* **260**, 471–475 (1996). DOI CrossRef Google Scholar

[147] Kong, J., Soh, H. T., Cassell, A. M., Quate, C. F. & Dai, H. Synthesis of individual single-walled carbon nanotubes on patterned silicon wafers. *Nature* **395**, 878–881 (1998). DOI CrossRef Google Scholar

[148] Vander Wal, R. L., Ticich, T. M. & Curtis, V. E. Flame synthesis of metal-catalyzed single-wall carbon nanotubes. *J. Phys. Chem. A* **104**, 7209–7217 (2000). DOI CrossRef Google Scholar

[149] Kim, W. *et al.* Synthesis of Ultralong and High Percentage of Semiconducting Single-walled Carbon Nanotubes. *Nano Lett.* **2**, 703–708 (2002). DOI CrossRef Google Scholar

[150] Satishkumar, B. C., Govindaraj, A., Sen, R. & Rao, C. N. R. Single-walled nanotubes by the pyrolysis of acetylene-organometallic mixtures. *Chem. Phys. Lett.* **293**, 47–52 (1998). DOI CrossRef Google Scholar

[151] Maruyama, S., Kojima, R., Miyauchi, Y., Chiashi, S. & Kohno, M. Low-temperature synthesis of high-purity single-walled carbon nanotubes from alcohol. *Chem. Phys. Lett.* **360**, 229–234 (2002). DOI CrossRef Google Scholar

[152] Bai, S., Li, F., Yang, Q. H., Cheng, H. M. & Bai, J. B. Influence of ferrocene/benzene mole ratio on the synthesis of carbon nanostructures. *Chem. Phys. Lett.* **376**, 83–89 (2003). DOI CrossRef Google Scholar

[153] Liao, H. & Hafner, J. H. Low-temperature single-wall carbon nanotube synthesis by thermal chemical vapor deposition. *J. Phys. Chem. B* **108**, 6941–6943 (2004). DOI CrossRef Google Scholar

[154] Harutyunyan, A. R., Pradhan, B. K., Kim, U. J., Chen, G. & Eklund, P. C. CVD Synthesis of Single Wall Carbon Nanotubes under 'Soft' Conditions. *Nano Lett.* **2**, 525–530 (2002). DOI CrossRef Google Scholar

[155] Zheng, L. X. *et al.* Ultralong single-wall carbon nanotubes. *Nat. Mater.* **3**, 673–676 (2004). DOI CrossRef Google Scholar

[156] Hata, K. *et al.* Water-assisted highly efficient synthesis of impurity-free single-walled carbon nanotubes. *Science (80-.).* **306**, 1362–1364 (2004). DOI CrossRef Google Scholar

[157] Yumura, M. Synthesis and Purification of Multi-Walled and Single-Walled Carbon Nanotubes. in *The Science and Technology of Carbon Nanotubes* 2–13 (Elsevier, 1999). DOI CrossRef Google Scholar

[158] Tohji, K. *et al.* Purifying single-walled nanotubes. *Nature* **383**, 679 (1996). DOI CrossRef Google Scholar

[159] Bandow, S., Asaka, S., Zhao, X. & Ando, Y. Purification and magnetic properties of carbon nanotubes. *Appl. Phys. A Mater. Sci. Process.* **67**, 23–27 (1998). Google Scholar

[160] Duesberg, G. S., Muster, J., Krstic, V., Burghard, M. & Roth, S. Chromatographic size separation of single-wall carbon nanotubes. *Appl. Phys. A Mater. Sci. Process.* **67**, 117–119 (1998). CrossRef Google Scholar

[161] Ren, W., Li, F., Chen, J., Bai, S. & Cheng, H. M. Morphology, diameter distribution and Raman scattering measurements of double-walled carbon nanotubes synthesized by catalytic decomposition of methane. *Chem. Phys. Lett.* **359**, 196–202 (2002). DOI CrossRef Google Scholar

[162] Fang, H. T. *et al.* Purification of single-wall carbon nanotubes by electrochemical oxidation. *Chem. Mater.* **16**, 5744–5750 (2004). DOI CrossRef Google Scholar

[163] Chang, H. & Bard, A. J. Scanning Tunneling Microscopy Studies of Carbon-Oxygen Reactions on Highly Oriented Pyrolytic Graphite. *J. Am. Chem. Soc.* **113**, 5588–5596 (1991). DOI CrossRef Google Scholar

[164] Colbert, D. T. *et al.* Growth and sintering of fullerene nanotubes. *Science (80-.).* **266**, 1218–1222 (1994). DOI CrossRef Google Scholar

[165] Banerjee, S., Hemraj-Benny, T. & Wong, S. S. Covalent surface chemistry of single-walled carbon nanotubes. *Adv. Mater.* **17**, 17–29 (2005). DOI CrossRef Google Scholar

[166] Niyogi, S. *et al.* Chemistry of single-walled carbon nanotubes. *Acc. Chem. Res.* **35**, 1105–1113 (2002). DOI CrossRef Google Scholar

[167] Ajayan, P. M. *et al.* Opening carbon nanotubes with oxygen and implications for filling. *Nature* **362**, 522–525 (1993). DOI CrossRef Google Scholar

[168] Ebbesen, T. W., Ajayan, P. M., Hiura, H. & Tanigaki, K. Purification of nanotubes [6]. *Nature* **367**, 519 (1994). DOI CrossRef Google Scholar

[169] Zimmerman, J. L., Bradley, R. K., Huffman, C. B., Hauge, R. H. & Margrave, J. L. Gas-phase purification of single-wall carbon nanotubes. *Chem. Mater.* **12**, 1361–1366 (2000). DOI CrossRef Google Scholar

[170] Chiang, I. W., Brinson, B. E., Smalley, R. E., Margrave, J. L. & Hauge, R. H. Purification and characterization of single-wall carbon nanotubes. *J. Phys. Chem. B* **105**, 1157–1161 (2001). DOI CrossRef Google Scholar

[171] Xu, Y. Q., Peng, H., Hauge, R. H. & Smalley, R. E. Controlled multistep purification of single-walled carbon nanotubes. *Nano Lett.* **5**, 163–168 (2005). DOI CrossRef Google Scholar

[172] Jeong, T., Kim, W. Y. & Hahn, Y. B. A new purification method of single-wall carbon nanotubes using H_2S and O_2 mixture gas. *Chem. Phys. Lett.* **344**, 18–22 (2001). DOI CrossRef Google Scholar

[173] Tobias, G., Shao, L., Salzmann, C. G., Huh, Y. & Green, M. L. H. Purification and opening of carbon nanotubes using steam. *J. Phys. Chem. B* **110**, 22318–22322 (2006). DOI CrossRef Google Scholar

[174] Hu, H., Zhao, B., Itkis, M. E. & Haddon, R. C. Nitric Acid Purification of Single-Walled Carbon Nanotubes. *J. Phys. Chem. B* **107**, 13838–13842 (2003). DOI CrossRef Google Scholar

[175] Zhao, X. *et al.* Large-scale purification of single-wall carbon nanotubes prepared by electric arc discharge. *Diam. Relat. Mater.* **15**, 1098–1102 (2006). DOI CrossRef Google Scholar

[176] Suzuki, T. *et al.* Purification of single-wall carbon nanotubes produced by arc plasma jet method. *Diam. Relat. Mater.* **16**, 1116–1120 (2007). DOI CrossRef Google Scholar

[177] Wang, Y., Shan, H., Hauge, R. H., Pasquali, M. & Smalley, R. E. A highly selective, one-pot purification method for single-walled carbon nanotubes. *J. Phys. Chem. B* **111**, 1249–1252 (2007). DOI CrossRef Google Scholar

[178] Liu, J. *et al.* Fullerene pipes. *Science (80-.).* **280**, 1253–1256 (1998). DOI CrossRef Google Scholar

[179] Wiltshire, J. G. *et al.* Comparative studies on acid and thermal based selective purification of HiPCO produced single-walled carbon nanotubes. *Chem. Phys. Lett.* **386**, 239–243 (2004). DOI CrossRef Google Scholar

[180] Li, Y. *et al.* Purification of CVD synthesized single-wall carbon nanotubes by different acid oxidation treatments. *Nanotechnology* **15**, 1645–1649 (2004). DOI CrossRef Google Scholar

[181] Zhang, J. *et al.* Effect of chemical oxidation on the structure of single-walled carbon nanotubes. *J. Phys. Chem. B* **107**, 3712–3718 (2003). DOI CrossRef Google Scholar

[182] Hernadi, K., Siska, A., Thiên-Nga, L., Forró, L. & Kiricsi, I. Reactivity of different kinds of carbon during oxidative purification of catalytically prepared carbon nanotubes. *Solid State Ionics* **141–142**, 203–209 (2001). DOI CrossRef Google Scholar

[183] Tasis, D., Tagmatarchis, N., Georgakilas, V. & Prato, M. Soluble carbon nanotubes. *Chem. - A Eur. J.* **9**, 4000–4008 (2003). DOI CrossRef Google Scholar

[184] Rao, C. N. R., Satishkumar, B. C., Govindaraj, A. & Nath, M. Nanotubes. *ChemPhysChem* **2**, 78–105 (2001). DOI CrossRef Google Scholar

[185] Gao, B. *et al.* Fabrication and electron field emission properties of carbon nanotube films by electrophoretic deposition. *Adv. Mater.* **13**, 1770–1773 (2001). DOI CrossRef Google Scholar

[186] Hafner, J. H., Cheung, C. L., Oosterkamp, T. H. & Lieber, C. M. High-yield assembly of individual single-walled carbon nanotube tips for scanning probe microscopies. *J. Phys. Chem. B* **105**, 745–746 (2001). DOI CrossRef Google Scholar

[187] Hou, P. X., Liu, C. & Cheng, H. M. Purification of carbon nanotubes. *Carbon N. Y.* **46**, 2003–2025 (2008). DOI CrossRef Google Scholar

[188] Hu, H. *et al.* Influence of the zeta potential on the dispersability and purification of single-walled carbon nanotubes. *J. Phys. Chem. B* **109**, 11520–11524 (2005). DOI CrossRef Google Scholar

[189] Yu, A. *et al.* Application of centrifugation to the large-scale purification of electric arc-produced single-walled carbon nanotubes. *J. Am. Chem. Soc.* **128**, 9902–9908 (2006). DOI CrossRef Google Scholar

[190] Klumpp, C., Kostarelos, K., Prato, M. & Bianco, A. Functionalized carbon nanotubes as emerging nanovectors for the delivery of therapeutics. *Biochim. Biophys. Acta - Biomembr.* **1758**, 404–412 (2006). DOI CrossRef Google Scholar

[191] Lambert, J. M. *et al.* Improving conditions towards isolating single-shell carbon nanotubes. *Chem. Phys. Lett.* **226**, 364–371 (1994). DOI CrossRef Google Scholar

[192] Andrews, R., Jacques, D., Qian, D. & Dickey, E. C. Purification and structural annealing of multiwalled carbon nanotubes at graphitization temperatures. *Carbon N. Y.* **39**, 1681–1687 (2001). DOI CrossRef Google Scholar

[193] Huang, W., Wang, Y., Luo, G. & Wei, F. 99.9% Purity Multi-Walled Carbon Nanotubes By Vacuum High-Temperature Annealing. *Carbon N. Y.* **41**, 2585–2590 (2003). DOI CrossRef Google Scholar

[194] Wang, Y., Wu, J. & Wei, F. A treatment method to give separated multi-walled carbon nanotubes with high purity, high crystallization and a large aspect ratio. *Carbon N. Y.* **41**, 2939–2948 (2003). DOI CrossRef Google Scholar

[195] Kim, Y. A., Hayashi, T., Osawa, K., Dresselhaus, M. S. & Endo, M. Annealing effect on disordered multi-wall carbon nanotubes. *Chem. Phys. Lett.* **380**, 319–324 (2003). DOI CrossRef Google Scholar

[196] Hou, P. X., Liu, C. & Cheng, H. M. Purification of carbon nanotubes. *Carbon N. Y.* **46**, 2003–2025 (2008). DOI CrossRef Google Scholar

[197] Koch, C. C. The synthesis and structure of nanocrystalline materials produced by mechanical attrition: A review. *Nanostructured Mater.* **2**, 109–129 (1993). DOI CrossRef Google Scholar

[198] Tjong, S. C. Nanocrystalline Materials: Their Synthesis-Structure-Property Relationships and Applications. *Nanocrystalline Mater.* **40**, 41–64 (2006). CrossRef

[199] Gleiter, H. Nanocrystalline materials. *Prog. Mater. Sci.* 33, 223–315 (1989). DOI CrossRef

[200] Suryanarayana, C. Non-equilibrium processing of materials. (Elsevier, 1999). CrossRef Google Scholar

[201] Fecht, H. J., Hellstern, E., Fu, Z. & Johnson, W. L. Nanocrystalline metals prepared by high-energy ball milling. *Metall. Trans. A* **21**, 2333–2337 (1990). DOI CrossRef Google Scholar

[202] Eckert, J., Holzer, J. C., Krill, C. E. & Johnson, W. L. Structural and thermodynamic properties of nanocrystalline fcc metals prepared by mechanical attrition. *J. Mater. Res.* **7**, 1751–1761 (1992). DOI CrossRef Google Scholar

[203] Eckert, J. & Borner, I. Nanostructure formation and properties of ball-milled NiAl intermetallic compound. *Mater. Sci. Eng. A* **239–240**, 619–624 (1997). DOI CrossRef Google Scholar

[204] Kim, I. Y. *et al.* Friction and wear characteristics of the carbon nanotube-aluminum composites with different manufacturing conditions. *Wear* **267**, 593–598 (2009). DOI CrossRef Google Scholar

[205] Wu, J., Zhang, H., Zhang, Y. & Wang, X. Mechanical and thermal properties of carbon nanotube/aluminum composites consolidated by spark plasma sintering. *Mater. Des.* **41**, 344–348 (2012). DOI CrossRef Google Scholar

[206] Morsi, K., Esawi, A. M. K., Borah, P., Lanka, S. & Sayed, A. Characterization and spark plasma sintering of mechanically milled aluminum-carbon nanotube (CNT) composite powders. J. Compos. Mater. 44, 1991–2003 (2010). DOI CrossRef Google Scholar

[207] Nie, J. H. *et al.* Aluminum matrix composites reinforced by molybdenum-coated carbon nanotubes. *Int. J. Miner. Metall. Mater.* **18**, 695–702 (2011). DOI CrossRef Google Scholar

[208] Kurita, H., Kwon, H., Estili, M. & Kawasaki, A. Multi-walled carbon nanotube-aluminum matrix composites prepared by combination of hetero-agglomeration method, spark

plasma sintering and hot extrusion. *Mater. Trans.* **52**, 1960–1965 (2011). DOI CrossRef Google Scholar

[209] Kondoh, K., Threrujirapapong, T., Umeda, J. & Fugetsu, B. High-temperature properties of extruded titanium composites fabricated from carbon nanotubes coated titanium powder by spark plasma sintering and hot extrusion. *Compos. Sci. Technol.* **72**, 1291–1297 (2012). DOI CrossRef Google Scholar

[210] Paramsothy, M., Tan, X. H., Chan, J., Kwok, R. & Gupta, M. Carbon nanotube addition to concentrated magnesium alloy AZ81: Enhanced ductility with occasional significant increase in strength. *Mater. Des.* **45**, 15–23 (2013). DOI CrossRef Google Scholar

[211] Imai, H. *et al.* Microstructural and electrical properties of copper titanium alloy dispersed with carbon nanotubes via powder metallurgy process+1. *Mater. Trans.* **55**, 522–527 (2014). DOI CrossRef Google Scholar

[212] Suryanarayana, C. Powder metal technologies and applications. *ASM Handb.* **7**, 80–90 (1998). Google Scholar

[213] Thümmler, F. & Oberacker, R. *An Introduction to Powder Metallurgy*. vol. 490 (Institute of Materials London, 1993). CrossRef Google Scholar

[214] Froes, F. H., Suryanarayana, C., Mukhopadhyay, D., Li, C. G. & Brand, K. Synthesis of intermetallics by mechanical alloying. *Acta Metall. Sin. Ser. A, Phys. Metall. Mater. Sci.* **8**, 441–446 (1995). DOI CrossRef Google Scholar

[215] Börner, I. & Eckert, J. Structural properties and compositional dependence of grain size in heavily mechanically deformed nanophase NiAl. in *Materials Science Forum* **225–227**, 377–382 (Trans Tech Publ, 1996). DOI CrossRef Google Scholar

[216] Suryanarayana, C. Mechanical alloying and milling. *Prog. Mater. Sci.* **46**, 1–184 (2001). DOI CrossRef Google Scholar

[217] E.O. Kovalska, Yu.I Sementsov, H.P. Prykhodko, M.T. Kartel', Process for the preparation of catalysts for chemical deposition of carbon nanotubes from gas phase (in Ukrainian), (2012) Patent # 70847 Ukraine, C01B11/00 D01F9/00. CrossRef Google Scholar

[218] A.V. Melezhyk, V.V. Yanchenko, Yu.I. Sementsov, Nanocarbon materials, NATO Security through Science Series A: Chemistry and Biology, 529–537 (2007). Google Scholar

[219] Sementsov, Y. U. I. *et al.* Properties of PTFE–MWNT composite materials. in *Hydrogen materials science and chemistry of carbon nanomaterials* 757–763 (Springer, 2007). DOI CrossRef Google Scholar

[220] Haynie, D. T. *Biological thermodynamics*. (Cambridge University Press, 2001). Google Scholar

[221] Gill, P., Moghadam, T. T. & Ranjbar, B. Differential scanning calorimetry techniques: Applications in biology and nanoscience. *J. Biomol. Tech.* **21**, 167–193 (2010). CrossRef Google Scholar

[222] Abraham, J., Mohammed, A. P., Kumar, M. P. A., George, S. C. & Thomas, S. Thermoanalytical techniques of nanomaterials. in *Characterization of Nanomaterials: Advances and Key Technologies* (eds. Mohan Bhagyaraj, S., Oluwafemi, O. S., Kalarikkal, N. & Thomas, S. B. T.-C. of N.) 213–236 (Woodhead Publishing, 2018). DOI CrossRef Google Scholar

[223] Zucca, N., Erriu, G., Onnis, S. & Longoni, A. An analytical expression of the output of a power-compensated DSC in a wide temperature range. *Thermochim. Acta* **413**, 117–125 (2004). DOI CrossRef Google Scholar

[224] Lehmann, H. P., Fuentes-Arderiu, X. & Bertello, L. F. Glossary of terms in quantities and units in clinical chemistry (IUPAC-IFCC recommendations 1996). *Pure Appl. Chem.* **68**, 957–1000 (1996). DOI CrossRef Google Scholar

[225] Laidler, K. J. A glossary of terms used in chemical kinetics, including reaction dynamics (IUPAC recommendations 1996). *Pure Appl. Chem.* **68**, 149–192 (1996). DOI CrossRef Google Scholar

[226] Uddandarao, P. & Balakrishnan, R. M. Thermal and optical characterization of biologically synthesized ZnS nanoparticles synthesized from an endophytic fungus Aspergillus flavus: A colorimetric probe in metal detection. *Spectrochim. Acta - Part A Mol. Biomol. Spectrosc.* **175**, 200–207 (2017). DOI CrossRef Google Scholar

[227] Kayal, S. & Ramanujan, R. V. Doxorubicin loaded PVA coated iron oxide nanoparticles for targeted drug delivery. *Mater. Sci. Eng. C* **30**, 484–490 (2010). DOI CrossRef Google Scholar

[228] Mansfield, E., Tyner, K. M., Poling, C. M. & Blacklock, J. L. Determination of nanoparticle surface coatings and nanoparticle purity using microscale thermogravimetric analysis. *Anal. Chem.* **86**, 1478–1484 (2014). DOI CrossRef Google Scholar

[229] Hunkel, M., Surm, H. & Steinbacher, M. Dilatometry. in *Handbook of Thermal Analysis and Calorimetry* (eds. Vyazovkin, S., Koga, N. & Schick, C. B. T.-H. of T. A. and C.) vol. 6 103–129 (Elsevier Science B.V., 2018). DOI CrossRef Google Scholar

[230] Barrera, G. D., Bruno, J. A. O., Barron, T. H. K. & Allan, N. L. Negative thermal expansion. *J. Phys. Condens. Matter* **17**, R217–R252 (2005). DOI CrossRef Google Scholar

[231] Evans, J. S. O. Negative thermal expansion materials. *J. Chem. Soc. - Dalt. Trans.* 3317–3326 (1999). DOI CrossRef Google Scholar

[232] White, G. K. Solids: Thermal expansion and contraction. Contemp. Phys. 34, 193–204 (1993). DOI CrossRef Google Scholar

[233] Bragg, L. Recent Advances in the Study of the Crystalline State. *Science (80-.).* **108**, 455–463 (1948). CrossRef Google Scholar

[234] Bian, Z., Pan, M. X., Zhang, Y. & Wang, W. H. Carbon-nanotube-reinforced $Zr_{52.5}Cu_{17.9}Ni_{14.6}$ $Al_{10}Ti_5$ bulk metallic glass composites. *Appl. Phys. Lett.* **81**, 4739–4741 (2002). DOI CrossRef Google Scholar

[235] Cao, A., Xu, C., Liang, J., Wu, D. & Wei, B. X-ray diffraction characterization on the alignment degree of carbon nanotubes. *Chem. Phys. Lett.* **344**, 13–17 (2001). DOI CrossRef Google Scholar

[236] Norton, M. G. & Suryanarayana, C. *X-Ray diffraction: a practical approach*. (Plenum Press, 1998). Google Scholar

[237] Kneringer, G., Roedhammer, P. & Wildner, H. Powder metallurgical high performance materials. Proceedings. Volume 2: P/M hard materials. (2001). CrossRef Google Scholar

[238] Lönnberg, B. Characterization of milled Si_3N_4 powder using X-ray peak broadening and surface area analysis. *J. Mater. Sci.* **29**, 3224–3230 (1994). DOI CrossRef Google Scholar

[239] Aymard, L., Delahaye-Vidal, A., Portemer, F. & Disma, F. Study of the formation reactions of silver-palladium alloys by grinding and post-milling isothermal annealing. *J. Alloys Compd.* **238**, 116–127 (1996). DOI CrossRef Google Scholar

[240] Jorio, A. *et al.* Characterizing carbon nanotube samples with resonance Raman scattering. *New J. Phys.* **5**, 139 (2003). CrossRef Google Scholar

[241] Dresselhaus, M. S. & Eklund, P. C. Phonons in carbon nanotubes. *Adv. Phys.* **49**, 705–814 (2000). DOI CrossRef Google Scholar

[242] Lehman, J. H., Terrones, M., Mansfield, E., Hurst, K. E. & Meunier, V. Evaluating the characteristics of multiwall carbon nanotubes. *Carbon N. Y.* **49**, 2581–2602 (2011). DOI CrossRef Google Scholar

[243] Mizuno, K. *et al.* A black body absorber from vertically aligned single-walled carbon nanotubes. *Proc. Natl. Acad. Sci.* **106**, 6044–6047 (2009). DOI CrossRef Google Scholar

[244] Ferraro, J. R. *Introductory raman spectroscopy*. (Elsevier, 2003). Google Scholar

[245] Tuinstra, F. & Koenig, J. Lo. Raman spectrum of graphite. *J. Chem. Phys.* **53**, 1126–1130 (1970). DOI CrossRef Google Scholar

[246] Eklund, P. C., Holden, J. M. & Jishi, R. A. Vibrational modes of carbon nanotubes; spectroscopy and theory. *Carbon N. Y.* **33**, 959–972 (1995). DOI CrossRef Google Scholar

[247] Rao, A. M. *et al.* Diameter-selective Raman scattering from vibrational modes in carbon nanotubes. *Science (80-.).* **275**, 187–191 (1997). DOI CrossRef Google Scholar

[248] Belin, T. & Epron, F. Characterization methods of carbon nanotubes: a review. *Mater. Sci. Eng. B* **119**, 105–118 (2005). DOI CrossRef Google Scholar

[249] Delzeit, L. *et al.* Growth of multiwall carbon nanotubes in an inductively coupled plasma reactor. *J. Appl. Phys.* **91**, 6027–6033 (2002). DOI CrossRef Google Scholar

[250] Cooper, C. A., Young, R. J. & Halsall, M. Investigation into the deformation of carbon nanotubes and their composites through the use of Raman spectroscopy. *Compos. Part A Appl. Sci. Manuf.* **32**, 401–411 (2001). DOI CrossRef Google Scholar

[251] Lourie, O. & Wagner, H. D. Evaluation of Young's modulus of carbon nanotubes by micro-Raman spectroscopy. *J. Mater. Res.* **13**, 2418–2422 (1998). DOI CrossRef Google Scholar

[252] Choi, H., Shin, J., Min, B., Park, J. & Bae, D. Reinforcing effects of carbon nanotubes in structural aluminum matrix nanocomposites. *J. Mater. Res.* **24**, 2610–2616 (2009). DOI CrossRef Google Scholar

[253] Saito, R. *et al.* Probing Phonon Dispersion Relations of Graphite by Double Resonance Raman Scattering. *Phys. Rev. Lett.* **88**, 4 (2002). DOI CrossRef Google Scholar

[254] Osswald, S., Flahaut, E., Ye, H. & Gogotsi, Y. Elimination of D-band in Raman spectra of double-wall carbon nanotubes by oxidation. *Chem. Phys. Lett.* **402**, 422–427 (2005). DOI CrossRef Google Scholar

[255] Bose, S. M., Gayen, S. & Behera, S. N. Theory of the tangential G-band feature in the Raman spectra of metallic carbon nanotubes. *Phys. Rev. B - Condens. Matter Mater. Phys.* **72**, 153402 (2005). DOI CrossRef Google Scholar

[256] Chakrapani, N. *et al.* Spectral fingerprinting of structural defects in plasma-treated carbon nanotubes. *J. Mater. Res.* **18**, 2515–2521 (2003). DOI CrossRef Google Scholar

[257] Endo, M. *et al.* Nanotube Coalescence-Inducing Mode: A Novel Vibrational Mode in Carbon Systems. *Small* **2**, 1031–1036 (2006). DOI CrossRef Google Scholar

[258] Fantini, C. *et al.* Resonance Raman study of linear carbon chains formed by the heat treatment of double-wall carbon nanotubes. *Phys. Rev. B* **73**, 193408 (2006). DOI CrossRef Google Scholar

[259] Jinno, M. *et al.* Raman scattering study for heat-treated carbon nanotubes: The origin of ≈1855 cm^{-1} Raman band. *Chem. Phys. Lett.* **418**, 109–114 (2006). DOI CrossRef Google Scholar

[260] Kim, K. K. *et al.* Dependence of Raman spectra G′ band intensity on metallicity of single-wall carbon nanotubes. *Phys. Rev. B - Condens. Matter Mater. Phys.* **76**, 205426 (2007). DOI CrossRef Google Scholar

[261] Stuart, B.H. *Infrared Spectroscopy: Fundamentals and Applications (Analytical Techniques in the Sciences (AnTs) *)*; John Wiley & Sons Ltd.: Chichester, UK, 2004. Google Scholar

[262] Juan, J. C. *et al.* Supported zirconium sulfate on carbon nanotubes as water-tolerant solid acid catalyst. *Mater. Res. Bull.* **42**, 1278–1285 (2007). DOI CrossRef Google Scholar

[263] Zhang, X., Fu, J., Zhang, Y. & Lei, L. A nitrogen functionalized carbon nanotube cathode for highly efficient electrocatalytic generation of H2O2 in Electro-Fenton system. *Sep. Purif. Technol.* **64**, 116–123 (2008). DOI CrossRef Google Scholar

[264] Boshko, O. *et al.* Structure and Strength of Iron-Copper-Carbon Nanotube Nanocomposites. *Nanoscale Res. Lett.* **11**, 1–8 (2016). DOI CrossRef Google Scholar

[265] Guérault, H. Propriétés structurales et magnétiques de poudres de fluorures nanostructurées MF3 (M= Fe, Ga) obtenues par broyage mécanique. (2000). CrossRef Google Scholar

[266] Kumar, A., Banerjee, U., Chowrasia, M. K., Shekhar, H. & Banerjee, M. K. Effect of MWCNT Content on the Structure and Properties of Spark Plasma-Sintered Iron-MWCNT Composites Synthesized by High-Energy Ball Milling. *J. Mater. Eng. Perform.* **28**, 2983–3000 (2019). DOI CrossRef Google Scholar

[267] Boshko, O. *et al.* Effect of the carbon nanotubes on structure and magnetic properties of the Fe–Cu (4:1) composites. *Adv. Powder Technol.* **27**, 1101–1108 (2016). DOI CrossRef Google Scholar

[268] Bian, Z., Pan, M. X., Zhang, Y., and W. H. Wang. Carbon-nanotube-reinforced $Zr_{52.5}Cu_{17.9}Ni_{14.6}Al_{10}Ti_5$ bulk metallic glass composites. *Appl. Phys. Lett*. **81,** 4739–4741 (2002). DOI CrossRef Google Scholar

[269] Pérez-Bustamante, R. *et al.* Microstructural and mechanical characterization of Al–MWCNT composites produced by mechanical milling. *Mater. Sci. Eng. A* **502**(1-2), 159–163 (2009). DOI CrossRef Google Scholar

[270] Bakshi, S. R., Singh V., Seal, S., and A. Agarwal. Aluminum composite reinforced with multiwalled carbon nanotubes from plasma spraying of spray-dried powders. *Surf. Coat. Tech*. **203,** 1544–1554 (2009). DOI CrossRef Google Scholar

[271] Chu, K., Wu, Q., Jia, C., Liang, X., Nie, J., Tian, W., Gai, G., and H. Guo. Fabrication and effective thermal conductivity of multiwalled carbon nanotubes reinforced Cu matrix composites for heat sink applications. *Comp. Sci. Tech.* **70,** 298–304 (2010). DOI CrossRef Google Scholar

[272] Shi, X. L., Yang, H., Shao, G. Q., Duan, Z. L., Yan, L., Xiong, Z., and P. Sun. Fabrication and properties of W–Cu alloy reinforced by multiwalled carbon nanotubes. *Mater. Sci. Eng. A* **457,** 18–23 (2007). DOI CrossRef Google Scholar

[273] Eckert, J., Holzer, J. C., Krill, C. E. & Johnson, W. L. Structural and thermodynamic properties of nanocrystalline fcc metals prepared by mechanical attrition. *J. Mater. Res.* **7**, 1751–1761 (1992). DOI CrossRef Google Scholar

[274] Börner, I. & Eckert, J. Structural properties and compositional dependence of grain size in heavily mechanically deformed nanophase NiAl. in *Materials Science Forum* vols 225–227 377–382 (Trans Tech Publ, 1996). DOI CrossRef Google Scholar

[275] Keszler, A. M., Nemes, L., Ahmad, S. R. & Fang, X. Characterisation of carbon nanotube materials by Raman spectroscopy and microscopy - A case study of multiwalled and singlewalled samples. *J. Optoelectron. Adv. Mater.* **6**, 1269–1274 (2004). Google Scholar

[276] Bokobza, L. Mechanical, electrical and spectroscopic investigations of carbon nanotube-reinforced elastomers. *Vib. Spectrosc.* **51**, 52–59 (2009). DOI CrossRef Google Scholar

[277] Knight, D. S. & White, W. B. Characterization of diamond films by Raman spectroscopy. *J. Mater. Res.* **4**, 385–393 (1989). DOI CrossRef Google Scholar

[278] Chieu, T. C., Dresselhaus, M. S. & Endo, M. Raman studies of benzene-derived graphite fibers. *Phys. Rev. B* **26**, 5867–5877 (1982). DOI CrossRef Google Scholar

[279] Katagiri, G. Raman Spectroscopy of Graphite and Carbon Materials and Its Recent Application. *Tanso* **1996**, 304–313 (1996). DOI CrossRef Google Scholar

[280] Lespade, P., Marchand, A., Couzi, M. & Cruege, F. Caracterisation de matériaux carbones par microspectrométrie Raman. *Carbon N. Y.* **22**, 375–385 (1984).DOI CrossRef Google Scholar

[281] Katagiri, G., Ishida, H. & Ishitani, A. Raman spectra of graphite edge planes. *Carbon N. Y.* **26**, 565–571 (1988). DOI CrossRef Google Scholar

[282] Asari, E. *et al.* Lattice disordering in graphite under rare-gas ion irradiation studied by Raman spectroscopy. *Phys. Rev. B* **49**, 1011–1015 (1994). DOI CrossRef Google Scholar